A Benchmark Study on Operational Modal Analysis System Identification Algorithms for Operating Offshore Wind Turbines

Georgios Gasparis

Technische Universiteit Delft

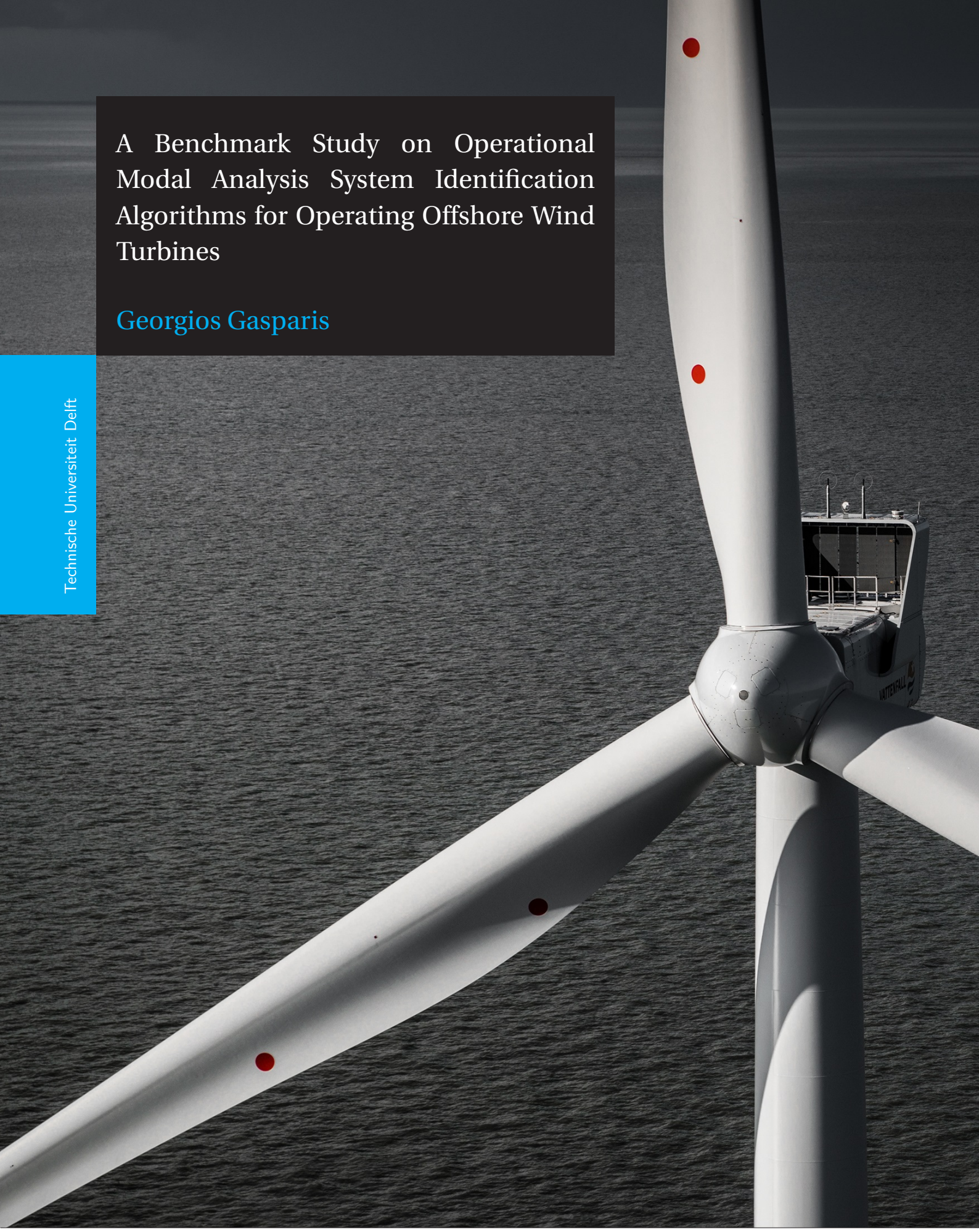

TU Delft Delft University of Technology

Challenge the future

TITLE

A BENCHMARK STUDY ON OPERATIONAL MODAL ANALYSIS SYSTEM IDENTIFICATION ALGORITHMS FOR OPERATING OFFSHORE WIND TURBINES

by

Georgios Gasparis

in partial fulfilment of the requirements for the degree of

Master of Science

in Offshore & Dredging Engineering

at the Delft University of Technology

Thesis committee::	Prof. dr. A. Metrikine,	TU Delft - Chairman
	Ir. D.J.M. Fallais,	TU Delft - Supervisor
	Ir. W.E. de Vries,	Eneco Wind

TU Delft Delft University of Technology

ABSTRACT

Recently, Offshore Wind Turbines (OWT) have attracted great attention in an effort to make a shift from fossil-based energy sources towards an enhanced sustainable and renewable energy production. In order to achieve the renewables targets and reduce the cost of wind energy, OWTs are consistently increasing in size. Therefore, research has targeted the optimization of OWT design. For many years, System Identification has played a central role in obtaining the actual modal properties of existing structures. Operational Modal Analysis (OMA) is a subset of these technique that applies on measurement data obtained from a structure loaded by ambient excitation. In the case of an OWT, such methods would be highly important in validating and/or updating the design and monitoring the structural health of the structure, which includes damage identification and fatigue damage estimation and would potentially lead into lifetime extension.

In practice, however, using OMA techniques on operating OWT is not a straightforward procedure. In fact, most of these techniques assume that the excitation is a white-noise process, which is not the case when waves and operational loads (e.g. rotational sampling) are present. Apart from that, the system itself is considered to be Linear Time-Invariant. Unfortunately, the modal properties of the system are highly affected by the varying rotational speed of the rotor and in general do violate the LTI assumptions. Given these challenges, the use-ability of existing methods need to be further investigated through application on OWTs under different operational conditions. Also, it is vital to asses and if possible eliminate the impact of the limitations related to loading on the identification.

Thus, a benchmark study of OMA algorithms has been performed on simulated data obtained from two models. The first model is a simplified OWT numerical model in Matlab, which can be used to validate the algorithms, and the second is the NREL 5-MW baseline offshore wind turbine in FAST that was used to simulate multiple different operational conditions. Using the simulated responses, at first, the Eigensystem Realization Algorithm (ERA) and the Natural Excitation Technique (NExT) were applied. Secondly, the widely used Stochastic Subspace Identification (SSI), has been included in this study. In Addition to these time domain techniques, the frequency-domain algorithms, Frequency Domain Decomposition (FDD) and the Least-Squares Complex Frequency-domain (LSCF) estimator were examined. In the end, Transmissibility-based Operational Modal Analysis (TOMA) was developed aiming in removing the influence of the external loading.

Through this study several parameters used in each algorithm as well as the robustness against harmonic excitation and measurement noise were investigated, providing the user with guidelines for each method. Then in the application on simulated data obtained from FAST, the results showed that all the algorithms were able to derive several stable modes, even when theoretically fundamental assumptions are violated. In general, the algorithms performed better for low wind speeds, while at high wind speeds the algorithms leaded in poorer identification (unstable and smaller number of modes). The greatest deviation compared to analytically obtained modal properties was observed in the damping ratios of the flapwise blade bending modes, where none of the algorithms was able to obtain such large damping ratios (>30%). However, most of them were still able to obtain two fore-aft tower modes and an accurate damping estimation. TOMA did remove the influence of external loading from the identification, but faced difficulties in obtaining blade modes. Finally, this benchmark study revealed the strengths and weaknesses of each technique when the core assumptions are violated.

ACKNOWLEDGEMENT

Throughout the last year I dedicated most of my attention in the preparation and completion of my master thesis project. During this period I faced multiple difficulties and I needed to ask Dominik Fallais for help and guidance, who kindly supervised me all this time and deserves my deepest respect and gratitude. I would also like to express my very great appreciation to Dominik for being undoubtedly supportive both in practical and psychological sense, and always willing to provide me with clear and essential answers. Apart from his very frequent support, I would like to thank Dominik for his willingness to provide me with alternative paths and motivate me to think wider.

In addition, I would like to express my great gratitude to Professor Metrikine for his inspiration as he is amongst the brightest professors I have met throughout my studies in TU Delft. I am particularly grateful for his contribution in giving me the opportunity to attend a series of courses related to structural dynamics. This provided me with an important background on this highly interesting field of engineering.

I would also like to expand my gratitude towards all those who have directly and indirectly encouraged me in writing and completing this thesis. Particularly, I would like to acknowledge the support provided by my family during all this difficult period of my studies, given the distance. Finally, I would like to offer my special thanks to all those who were patient and close to me, since that helped me a lot in being concentrated on my target.

Georgios Gasparis
Delft, March 2019

CONTENTS

LIST OF FIGURES

LIST OF TABLES

List of Abbreviation

BEM	Blade Element/Momentum
BET	Blade Element Theory
$BTLS$	Bootstrapped Total Least Squares
$Cov-SSI$	Covariance-Driven Stochastic Subspace Identification
CVA	Canonical Variant Analysis
$DD-SSI$	Data-Driven Stochastic Subspace Identification
DoF	Degrees of Freedom
$EFDD$	Enhanced Frequency Domain Decomposition
EMA	Experimental Modal Analysis
EoM	Equation of Motion
ERA	Eigenvalue Realization Algorithm
ERA/DC	Eigensystem Realization Algorithm with Data Correlation
$FAST$	Fatigue Aerodynamics Structures and Turbulence
FDD	Frequency Domain Decomposition
FE	Finite Element
FRF	Frequency Response Functions
$GTLS$	Generalized Total Least-Squares
HSS	High-Speed Shaft
$IDFT$	Inverse Discrete Fourier Transform
IEC	International Electrotechnical Commission
IMU	Inertia Measurement Unit
IRF	Impulse Response Functions
ITD	Ibrahim Time Domain
$JONSWAP$	JOint North Sea WAve Project
LS	Least Squares
$LSCE$	Least Square Complex Exponential
$LSCF$	Least Squares Complex Frequency
LSS	Low-Speed Shaft
LTI	Linear Time Invariant
LTP	Linear Time Periodic

MAC	Modal Amplitude Coherence - Used in `ERA`
MAC	Modal Assurance Criterion - Used in `FDD`
$MDoF$	Multiple Degree of Freedom
$MIMO$	Multiple-Input Multiple-Output
MLE	Maximum Likelihood Estimation
MSL	Mean Sea Level
$NExT$	Natural Excitation Technique
$NREL$	National Renewable Energy Laboratory
OMA	Operational Modal Analysis
OWT	Offshore Wind Turbine
PC	Principal Component
$pLSCF$	poly-reference Least Squares Complex Frequency
PP	Peak Picking
PSD	Power Spectral Density
$PSDT-OMA$	Power Spectrum Density Transmissibility based OMA
$pTOMA$	Poly-reference Transmissibility-based Operational Modal Analysis
RNA	Rotor-Nacelle Assembly
$SDoF$	Single Degree of Freedom
SHM	Structural Health Monitoring
$SIMO$	Single-Input Multiple-Output
SNR	Signal-to-Noise Ratio
SSI	Stochastic Subspace Identification
$SSTD$	Single-Station Time Domain
SVD	Singular Value Decomposition
TLS	Total Least Squares
$TOMA$	Transmissibility based
$Tv-TOMA$	Time-Varying Transmissibility based OMA
UPC	Unweighted Principal Component

1

INTRODUCTION

In recent years, there has been an inclination towards renewable energy resources, and wind power in particular. For the coming decades, wind industry aims at increasing the wind power production by developing more and more offshore wind farms. In order to achieve this target, there is a great demand for new technologies and techniques with respect to OWT structures. Operational Modal Analysis is the field that aims at deriving the dynamic properties of an existing structure and has great potential in offshore wind turbines applications. However, applying such techniques is not straightforward for offshore wind turbines, especially under operational conditions. In fact, fundamental theoretical assumptions which are made during the derivation of most state of the art OMA algorithms are violated. This chapter, briefly mentions several identification methods, and also describes the strategy that will be followed in order to investigate if existing system identification algorithms can be adapted and used on OWTs, or the violated assumptions will result in loss of use-ability. After this introduction, the desired applications as well as the main challenges are presented. The chapter is closed with the problem statement and an chapter-wise overview of this thesis.

1.1. WIND POWER

In the coming decades, global energy needs are predicted to rise. This fact is mainly related to the growth of the world population, but also to the increasing standards of living for people of the developing countries. In order to meet this rising energy demand, more and more different energy resources need to be exploited.

To date, fossil fuels (*e.g.* oil, coal and gas) remain the dominant source and drive the global energy consumption. However, investments in renewable energy resources are rising, since it is a very promising alternative source of energy. Replacing fossil fuels with renewable energy sources will reduce global warming by mitigating the greenhouse gas emissions. Another reason to lean towards renewables is that they are clean energy sources with a positive impact on public health. Finally, renewables are inexhaustible sources of energy and can contribute in creating a sustainable world that does not depend on the limited amount of resources.

Amongst all possible renewable energy resource, wind energy is the most abundant one. Technologies to extract wind power have being investigated for decades, but it is a fact that attention is largely attracted in recent years. It is not an exaggeration to say that wind power nowadays has become the fastest growing energy source in the world. This has led to rapid growth of wind farm construction both onshore and offshore. It is obvious that developing onshore wind farms is faster, cheaper and easier than offshore. However, wind power industry aims at increasing the wind power production, and using bigger turbines, under higher and steadier wind velocities is the answer. This is the reason why more and more wind farms have being developed deeper, further offshore. As it is shown in Figure 1.1, offshore wind aims at exceeding a capacity of 500GW by 2050[1].

This target is a great challenge itself, since the development of offshore wind farms is not a straightforward procedure. This relatively new field is often connected to problems that have never been encountered before. Also, wind industry aims at driving down the cost of wind power in order to make it a fully competitive energy source. Therefore, there is a great demand of technical knowledge, new technologies and techniques.

1.2. AN OVERVIEW OF IDENTIFICATION TECHNIQUES

For many years researchers have being investigating ways to process information that is present in measurement data collected from civil (*e.g.* public buildings, bridges) and mechanical structures (*e.g.* wind turbines)

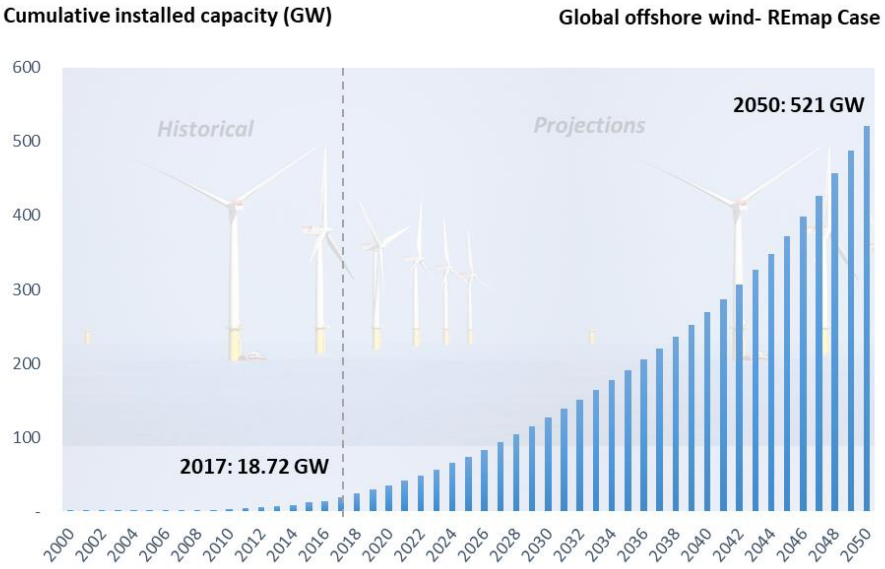

Figure 1.1: Historical and projected total installed capacity of offshore wind, 2000–2050

in order to get a better understanding of the real physics and the actual structural behaviour.

One way to determine the actual dynamic properties of an existing structure is by applying Experimental Modal Analysis (EMA) techniques. More in detail, EMA is carried out by artificially exciting the structure with known, measured forces (input), while measuring the structural response (output). These experiments can be performed by using shakers, drop weights or impact hammers in laboratory, in order to derive measurements of good quality. Then, the structure's modal parameters (modal frequencies and damping ratios, mode shapes and participation factors) can be determined by applying system identification techniques on the input-output data. The identification most of the times is based on the Impulse Response Functions (IRF), or on the Frequency Response Functions (FRF) for time-domain and frequency-domain techniques, respectively. Some of the traditional time-domain system identification algorithms that were developed to extract the modal parameters from the IRF are the Eigenvalue Realization Algorithm (ERA)[2][3], the Ibrahim Time Domain (ITD)[4] and the Least-Square Complex Exponential method (LSCE)[5]. Due to the fact that both input and output are measured, EMA methods many times are referred to as deterministic system identification techniques. The identification of a system using EMA techniques can be shown in Figure 1.2.

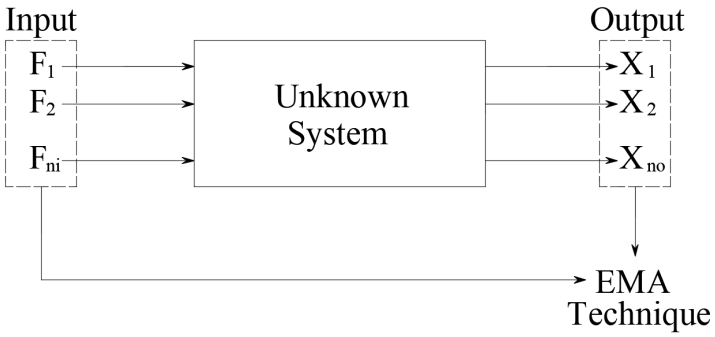

Figure 1.2: Deterministic Input-Output identification

Unfortunately, EMA approaches are inappropriate for large and complex structures like OWT. Laboratory conditions can largely differ from the complicated real-operating conditions. Also, measuring the excitation forces for the case of an OWT is not a trivial task. On the other hand, a different type of modal analysis, which considers that the structure is under real operational conditions has been developed with great success and a large number of applications. Such system identification techniques identify the modal parameters (modal frequencies, damping ratios and mode shapes) of the structure using output-only response data, without

measuring the excitation forces. Therefore, no equipment to excite a structure is needed. In that sense, Operational Modal Analysis (OMA) techniques are faster and cheaper than EMA techniques. Another advantage is that the structure of interest is tested under the complicated real-operating conditions, leading into more realistic identified modal models.

When performing an OMA technique the applied forces are not known but they are assumed to behave approximately as band-limited white noise. Ambient excitation due to wind, traffic and earthquakes are some examples. Particularly for the case of an OWT, the turbine is loaded by wind and waves. Most of the OMA methods implicitly assume that the dynamic content in the measured data is directly linked to the structural properties and not the loading. This is directly linked to the assumption of white noise excitation.

The Natural Excitation Technique (NExT)[6][7] was the pioneering method that set the foundations for OMA. By combining NExT with an IRF-based system identification algorithm, the modal parameters can be identified using only output response time-histories. One of the most popular time-domain OMA techniques is the Stochastic Subspace Identification technique (SSI)[8][9], which uses output-only measurements for a system under random excitation. OMA techniques in frequency-domain have also been developed, apart from time-domain. Peak Picking (PP) is the simplest frequency-domain technique, since the natural frequencies are just manually selected from the peaks of the Power Spectral Density (PSD). Moreover, one of the most popular frequency-domain OMA techniques is the so-called Frequency Domain Decomposition (FDD)[10], which has been used with great success in many applications. Finally, more advanced techniques have also been developed, that aim in determining the modal parameters of the system by applying curve fitting techniques on the measured response spectrum. Some of the most popular are the Least-Squares Complex Frequency-domain (LSCF) estimator[11] and the poly-reference version of it (pLSCF)[12][13].

It needs to be mentioned that most of the OMA techniques work by also assuming that the structure behaves as a Linear Time-Invariant (LTI) system in the analysed time interval. However, structures with rotating parts are most of the times described as Linear Time-Periodic (LTP) systems instead. Some OMA algorithms have also been extended or developed from ground up for LTP systems[14][15] and for non-linear systems[16]. The fundamental difference is related to the way the discrete-time state-space equation of motion is formulated. In LTP the so-called Floquet exponents of the system are identified instead of the the typical modal parameters.

In most of the algorithms, which were briefly described before, the unmeasured input is assumed to be a stochastic process. Therefore, the measured response will be a random signal. Such OMA identification procedures are sometimes called stochastic (as illustrated in Figure 1.3).

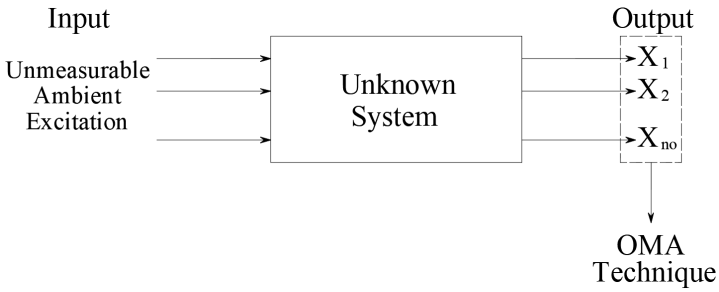

Figure 1.3: Stochastic Output-only identification

For the reasons explained before, and also due to the fact that the determination of the actual loading on an OWT is already a very difficult task, it can be concluded that OMA techniques are extremely attractive for the identification of the dynamic properties of OWT structures.

Online monitoring of system parameters is also another field of identification techniques with a large number of applications and increasingly high interest[17][18]. Some cases of OMA system identification techniques have also been used in an automated way, directly on real-life measured responses, in order to monitor the effect of unknown system parameters of interest on the dynamic characteristics of the structure. Applying online monitoring techniques on wind turbines is indeed a challenging topic, which attracts researchers' attention.

Finally, system identification techniques can also be separated into parametric and non-parametric methods. In the first case, the target is to determine several parameters of the system of interest (*e.g.* natural frequency, damping, stiffness, etc). On the other hand, non-parametric methods aim in modelling a system directly with its responses (*e.g.* impulse response, step response, etc) [19].

1.3. IMPORTANCE AND APPLICATIONS OF IDENTIFIED DYNAMIC PROPERTIES

Identifying a modal model of an OWT has great scientific, but also practical interest. Determining the modal properties is motivated by the fact that it is an important, and often the only, input for many possible applications.

At first, it needs to be stressed out that the real dynamic behaviour of an OWT is usually different than in the predicted response, which is simulated during the design process using (aero-elastic coupled) finite element (FE) models. Errors can be introduced by assumptions made during modelling the structure. After all, every model is more or less a simplification of reality. For instance, the support conditions can be modelled using the simplest linear spring-dashpot model in order to represent the soil stiffness. However the response and interaction of the soil with the turbine foundation in reality will probably be different than in the FE model. Therefore, the identified modal parameters can be used to get a better understanding of the real dynamic behaviour of the structure and to validate the design, or update the FE model, if needed.

Another potential field of application is Structural Health Monitoring (SHM) of OWTs, which includes damage identification and fatigue damage estimation. The first aims at detecting and quantifying any damages related to changes of the structural system, while the second is used to predict the accumulated fatigue damage in order to assess the potential of lifetime extension of the turbine. Therefore, SHM is a promising strategy that aims at assessing and predicting the structural health state of the turbine with the objective to reduce maintenance cost and potentially extend the lifetime of a single, or a group of, offshore wind turbines. An accurate identification of the modal parameter is fundamental for the applicability of many SHM methods, which motivates to investigate the question of the applicability of OMA algorithms outside their theoretical framework.

Finally, the actual dynamic properties of a structure may also reveal and clarify some unexplored aspects of related, not completely understood physics behind the complex nature of an OWT system in a highly dynamic environment. This may help to create improved and new models and guide the design. Hence, there is strong motivation to investigate the applicability of a variety of OMA system identification techniques, for the case of OWT structures.

1.4. KEY CHALLENGES

Identification of modal parameters on a full-scale OWT is a very difficult and complex task. Researchers still put a lot of effort into the development of suitable methods that will result in an accurate and reliable identification over the full range of operational conditions. OMA system identification algorithms are widely applied when collecting input time-series is not possible. Therefore, from now on attention will be focused on such techniques.

The best agreement between the theoretical assumptions made during deriving an OMA algorithm and the dynamic behaviour of an OWT can be found when the turbine is not rotating (parked conditions). For this particular case the environmental conditions do approach the assumption of white noise excitation to a reasonable degree. Furthermore, the system properties remain unchanged with respect to the environmental and operational conditions. However, current OMA techniques have serious limitations when applied to an OWT under operating conditions and the identification is not a straightforward task anymore.

1.4.1. WHITE NOISE EXCITATION ASSUMPTION

The unmeasurable input loading is one of the limitations, since in practice it cannot be approximated by Gaussian white noise process. In case where harmonic components are also present in the input, it is expected that classic OMA techniques will provide incorrect results in these frequency regions. Their influence on the identification procedure should be eliminated before extracting the structural modes, since directly applying current techniques without first dealing with the harmonic components may encounter several difficulties. At first, most OMA techniques will probably falsely associate the dynamics of the harmonic components of the loading with system properties. This means that harmonic modes may be mistaken for being structural modes. In OMA system identification it is a challenge to distinguish the real structural dynamic behaviour from noise and excitation contributions. A second problem is caused in case where the non-white noise force contributions have larger energy than the ambient excitation, particularly at frequencies close to any natural frequency of the system. This leads classical identification algorithms to fail in separating harmonic modes from structural modes. Thus, false modes may be identified instead of the weakly excited structural modes and the identification accuracy may be badly affected.

In reality, it is expected that an OWT will be loaded by wind and wave. In general, wind loads approximate

such a flat, broadband frequency spectrum and therefore, white noise assumption is not largely violated. On the other hand, in case where wave loading is dominant, coloured noise contributions are introduced and may affect the identification. Moreover, due to the rotation of the rotor of an operating OWT, the input forces are often more complex and sometimes significant harmonic components may be present in the measured response. Hence, the spectra of the aerodynamic forces is expected not to be flat, but with multiple peaks at frequencies proportional to the rotational frequency, as shown in Figure 1.4.

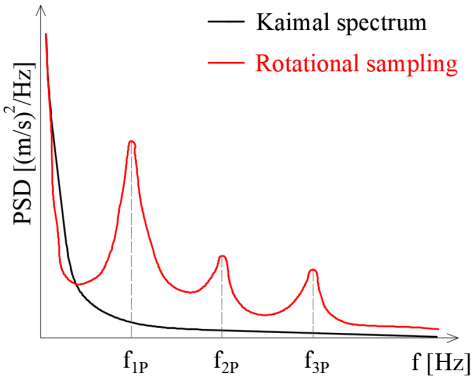

Figure 1.4: Schematic representation of Power Spectral Density (PSD) of input forcing with and without considering rotational sampling

As mentioned before, eliminating the influence of the harmonic components in the modal parameter extraction process is an important and very challenging task. For many years efforts have been continuously devoted in updating several OMA methods to tackle this problem. An interesting approach is proposed by P. Mohanty and D.J. Rixen, where several classic modal identification methods have been modified, in order to obtain the actual structural modes even in cases where harmonics components are close to the natural frequencies of the system. Some of the algorithms that have been modified are the Least-Square Complex Exponential (LSCE)[20], Eigenvalue Realization Algorithm (ERA)[21], Ibrahim Time Domain (ITD)[22] and the Single-Station Time-Domain method (SSTD)[23]. The main concept behind the modification is to force the algorithm to identify virtual modes with zero damping at frequencies equal to the frequencies of the harmonic excitation. Despite the fact that these modified techniques help in differentiating between structural modes and harmonic modes, one of the basic limitations is that the frequency of the harmonics must be exactly known a priori. Apart from IRF-based OMA techniques, classical SSI algorithm has also been recently modified in a similar way as explained before[24].

Another way to deal with the harmonic components in the frequency-domain is by filtering the response spectrum[25][26][27]. This approach aims at filtering-out the harmonic components from the measured response, so that it will explicitly include information related to the system. However, in case where the frequencies of the harmonic components are close to structural frequencies of the system, this approach leads in less reliable results. The main reason is that filtering will probably affect the measured response, causing loss of useful modal information and leading to errors in the identified structural modes.

A different innovative approach is to perform a frequency-domain system identification technique named Transmissibility based OMA (TOMA), as proposed by Devriendt et al.[28][29][30][31]. This type of OMA techniques aim in deriving a function, which has all the information needed to identify the modal parameters, but is also independent of the input loading. Therefore it seems that TOMA makes it possible to derive a modal model, which is not influenced by the violation of the assumption of white noise inputs due to the presence of coloured noise or harmonic components in the input. In case where the structure is loaded at different locations with uncorrelated forces, the transmissibility function as described in TOMA cannot be independent of the input's spectral content. Therefore an alternative approach has been proposed for multiple-input and multiple-output (MIMO) systems[32][33]. The main disadvantage of these methods is that they need at least two sets of measurements that correspond to different spatial loading conditions. An attempt to apply TOMA for one single set of measurements is also proposed by the same research team and is called time-varying TOMA (Tv-TOMA)[34][35]. The concept of using transmissibility functions in OMA has also been investigated by other researchers who have a different perspective. Power Spectrum Density Transmissibility based OMA (PSDT-OMA)[36][37] is another technique that aims at determining the modal parameters from one single set of measurements.

More approaches can be found in literature, along with related benefits and disadvantages. It is clear that

the application of OMA techniques on wind turbines is not a straight forward procedure due to the non-white noise nature of aerodynamic forcing. The performability of these methods needs to be further investigated through application on real OWT.

1.4.2. LTI SYSTEM ASSUMPTION

In OMA techniques, it is a common assumption to consider that the system of interest is an LTI system. Stationarity of the process is another strict assumption used in certain algorithms (*e.g.* NExT). It is clear though that an operating OWT violates this assumption. At first, when the wind velocity is larger than the rated (see Figure 1.5) the blades of the rotor start pitching-off in order to maintain constant power production, equal to the turbine's capacity. Since wind velocity is not steady, the assumption of LTI system is probably violated.

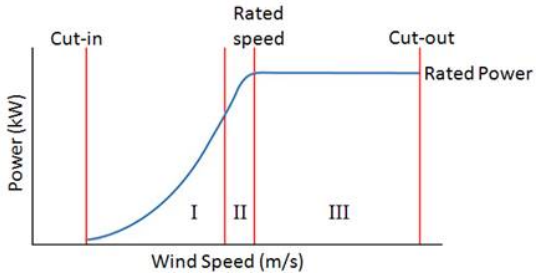

Figure 1.5: Ideal wind turbine power curve

Apart from the pitching of the blades, the measured response may also include transients due to start-up or shut-down. It is reasonable though to apply a system identification technique on a time range where the process is almost stationary and neglect the transients. However, it is important to keep in mind that the duration of the time-series should be long enough to ensure an accurate estimation of modal parameters.

Another parameter that is related to varying system properties is the yaw-motion of the nacelle. However, this does not seriously affect the LTI assumption, since yaw speed is very slow in general. However, it needs to be stressed out that in case where the identification is applied while the nacelle yaws, the measurements obtained at the tower will correspond to a coordinate system that is different to the nacelle coordinate system. Hence, the measurements will include components of the tower response parallel to the direction of the wind. In that case, errors can be introduced in the identification. This can be solved by using a fixed coordinate system for the measurement data.

Finally, the modal parameters of an OWT are also affected by the rotation of the rotor. More in detail, as it is shown in Figure 1.6[38], the natural frequencies of the blades are related to the rotor speed. Additionally, the rotor speed varies when shifting between operating zones. Therefore, in such a case the modal parameters are not constant.

This means that the rotor rotation leads to a violation of the time-invariance assumption. However, for the tower modes the effect of the rotor can be considered to be limited. The fact that the system is now time-variant makes the application of OMA for operational cases in which the yaw angle, blade angle and rotational speed of the rotor vary frequently questionable.

1.4.3. OTHER CHALLENGES

Apart from the violation of the basic assumptions behind OMA system identification algorithms, there are also several challenges that need to be considered when a modal model is derived.

At first, it is expected that the response data is polluted by noise. Stochastic system identification algorithms aim in limiting the effect of noise in the measurements. In case the data contains noise, the number of the identified modes is increased and much larger than the number of the structural modes. The modes that do not correspond to any structural modes are spurious modes and cause problems in the transparency of the identification. Sometimes it is also quiet difficult to differentiate between physical and spurious modes. In literature, the identified modes that correspond to the system modes are named as physical, or structural modes, while the additional modes due to noise as noise, fake, non-structural, spurious modes.

Another challenge is related to the number of sensors that is distributed over the structure. Strain sensors, accelerometers and inclinometers may be used to derive response time-series. However, most of the algorithms don't specify the type of the measurements and the question that arises is whether it is possible to

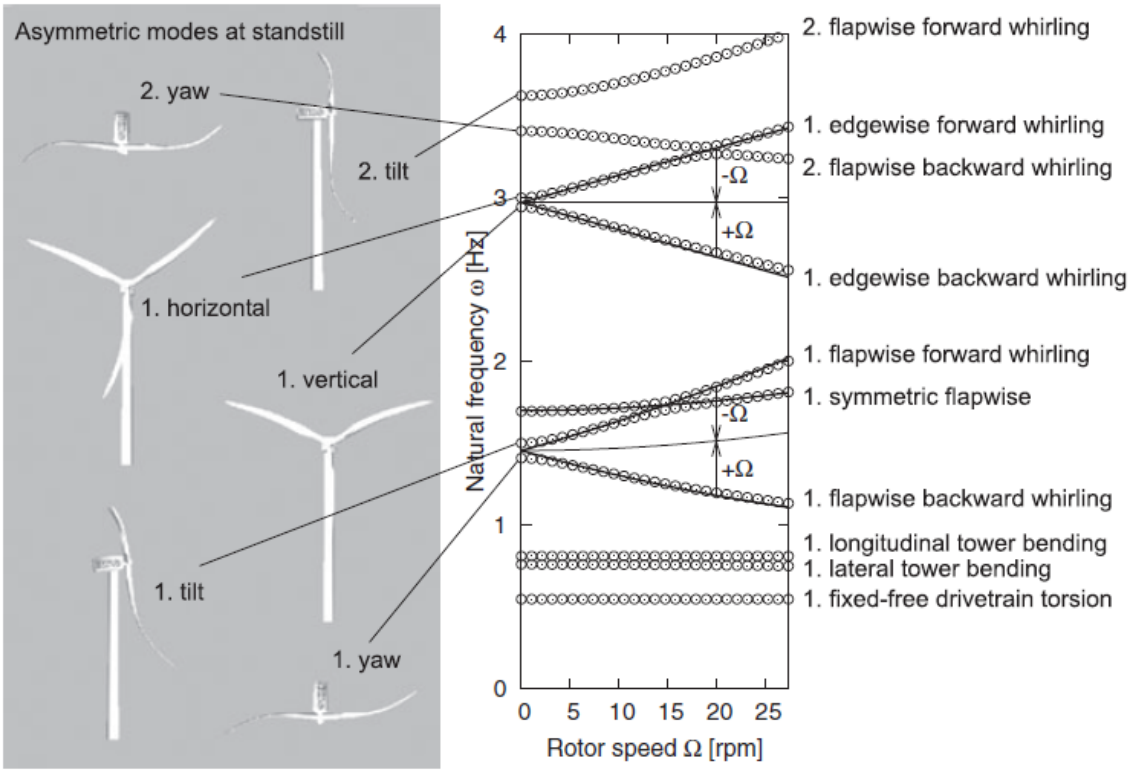

Figure 1.6: Campbell diagram of the first 10 structural modes

combine different types of data, or not. In that way, more information about the dynamic behaviour of the system may be derived from the identification procedure.

1.5. PROBLEM STATEMENT AND THESIS OBJECTIVE

Based on the aforementioned challenges and by also considering the violations of core assumptions in OMA techniques, a question arises.

"Can the existing OMA system identification algorithms be adapted and used on structural response data obtained from operating OWTs?"

In order to answer this question, it is important at first to assess and eliminate the impact of limitations related to loading on the identification. In other words, apply OMA techniques on OWT systems without being influenced by the violation of the white noise assumption. Additionally, it is also vital to investigate the applicability of OMA system identification techniques on measurements that correspond to different operational conditions. Finally, it is always important to examine several ways to optimize the identification procedure (*e.g.* derive clear stabilization diagrams). In order to do so, the possibilities of several existing OMA techniques for the case of offshore wind turbines need to be examined.

Particular attention will be drawn to applying system identification on measurements of different nature (*e.g.* strains and accelerations) and also using responses from different parts of the OWT (*e.g.* tower and blades).

The main objective of this thesis is to investigate the applicability of several existing OMA system identification algorithms on operating OWT structures, but also modify and update, if possible. Therefore, a comparative benchmark study will be performed on different state-of-the-art identification techniques. As different OMA algorithms identify a modal model in a different way, it is reasonable to expect that adopting these methods would result in different numerical conditioning and stability. In that sense, this study may also be used as a guideline for vibrating structures, since it will give advices on which algorithms performs best on operating OWT and it will reveal both pros and cons. Multiple different operational conditions will be considered in order to examine the robustness of the algorithms.

For the purpose of this study simulated data will be used. Two models have been considered: a simple Matlab OWT model and NREL) offshore 5-MW baseline wind turbine. The first model will be used to check initially whether the algorithms are able to identify accurately the dynamic properties of an LTI system with known dynamic properties. Once the algorithms are tested, the second model in FAST (Fatigue Aerodynamics Structures and Turbulence), which is a certified numerical representation of an OWT, can be used to derive simulated response signals as close as possible to a real set of data of a real turbine. The idea is to use a selection of controlled cases of measurements that correspond to different operating conditions. These selected measurement sets will be used in a later stage for the benchmark study of the examined OMA algorithms.

1.6. THESIS OVERVIEW

The thesis is organized as follows. Initially, Chapter 2 presents a description of the benchmark study, the assessment criteria of the algorithms that will be used, and the simulated cases that will be examined. Chapter 3 provides a brief introduction into OWT structures, dynamic properties and modelling. Also, both the model in Matlab and FAST are described in more detail. In this chapter the simulated measurements, which will be used for the benchmark study will be presented in depth. The next five chapters contain the results and analysis of different OMA algorithms that will be used. Chapter 4 and Chapter 5 are dedicated to time-domain OMA algorithms. The first is related to ERA algorithm that will be used together with NExT, while the second will present SSI algorithm, which is one of the most popular approaches. In the next two chapters, frequency-domain OMA techniques will be examined. The results and analysis for the FDD and LSCF algorithm will be presented in Chapter 6 and Chapter 7, respectively. Chapter 8 will present the results and analysis for the TOMA method, which is the last approach of the system identification methods that will be examined. Chapter 9 includes a discussion on using multiple and also different types of sensors. Finally, in Chapter 10 conclusions, recommendations and improvements will be discussed.

2

BENCHMARK DESCRIPTION

In this chapter, the algorithms that will be used for the benchmark study are summarized and an overview is presented, including descriptions about certain criteria based on which the techniques will be evaluated. Within the framework of this study, simulated data need to be generated. Section 2.2 will describe the loading cases that need to be simulated and their role in the benchmark study.

2.1. BENCHMARK OBJECTIVE

For many years Operational Modal Analysis (OMA) techniques have attracted great attention in the field of system identification. Existing techniques are constantly being improved and new approaches are introduced. Many algorithms may implement common ideas, but still each different approach has its own strengths and weaknesses. The main objective of this benchmark study is to identify the modal properties of an operating OWT, reveal these weaknesses and examine several ways to optimize the identification procedure. The algorithms that will be examined are briefly as follows:

- Chapter 4: Eigensystem Realization Algorithm (ERA)
- Chapter 5: Stochastic Subspace Identification (SSI)
- Chapter 6: Frequency Domain Decomposition (FDD)
- Chapter 7: Least-Squares Complex Frequency-domain estimator (LSCF)
- Chapter 8: Transmissibility-based OperationalModal Analysis (TOMA)

These algorithms are governed by fundamental assumptions that are violated when applied on an operating OWT. Particularly, all the algorithms make the assumption that the system is an LTI system. Also, the first four algorithms assume that the ambient excitation can be approximated by a white noise process. Both of these assumptions do not hold when the turbine operates. Therefore, their performance under such adverse conditions need to be assessed. The criteria that will be used in order to evaluate and compare the examined OMA techniques to each other are as follows:

- Deviation of identified modal properties from exact properties of the system (see Table 3.1 for model in Matlab and Table 3.4 & 3.5 for model in FAST)
- Number of identified modes
- Stability of identified modes (using stabilization diagrams)

2.2. EXAMINED REFERENCE LOAD CONDITIONS

For the purpose of this benchmark study, two models have been employed. These models will be used to generate data from several loading cases in order to apply and test the algorithms under controlled conditions. Initially, it is important to validate the algorithms under ideal conditions. Therefore, it is important to simulate data that satisfy the assumptions of the algorithms. Then, according to the main objective, the algorithms will be applied on data from an OWT under different operational conditions. The following two paragraphs will present the loading cases that need to be simulated from each model, and the purpose they serve.

Reference cases from Matlab model

The OWT model in Matlab that will be described in Section 3.2 is going to be used to simulate several sets of data for different types of input. As mentioned before, validating the algorithms is a vital step. Given that most of the OMA techniques mentioned before assume that system is loaded by white noise ambient excitation, the first type of input will be a white noise process. However, as we will see in the coming chapters, data simulated for the impulse load case will also be needed. Particularly, these data will be used as input for the ERA algorithm, since it is the only one that applies on free decay responses. Apart from validating the algorithms, the model in Matlab will be used to test the identification for a simplified wind, wave and current input. Finally, data from white noise and harmonic loading will be used in order to check the robustnesss of OMA techniques against the case where an harmonic excitation is included in the input. Table 2.1 shows a summary of the cases that will be simulated in the model in Matlab with respect to the algorithms that will be applied on them.

Input Type	ERA	SSI	FDD	LSCF	TOMA
Impulse	√	-	-	-	-
White noise	√	√	√	√	-
Wind, Wave & Current	√	√	√	√	-
White noise & Harmonics	√	√	√	√	-
White noise & Amplified Regions	-	-	-	-	√

Table 2.1: Input types that will be used at each algorithm

As it will be explained in Chapter 8, TOMA algorithm is applied on two sets of measurements, which correspond to sufficiently different loading conditions. Additionally, no assumption about the input is made for this algorithm. Thus, two different, modified cases will be examined, where the input is a white noise process with a smoothly increased amplitude around a frequency region. In that way, a coloured input will be generated.

The responses that will be used for the benchmark study are accelerations at four locations along the tower (see Figure 3.9). However, the model is able to generate strain responses. Strain data will be used in Chapter 9.2, where different types of sensors will be examined in the same identification.

Reference cases from FAST model

The second model that will be employed for this study is an existing OWT model developed by NREL, the analysis of which is performed using FAST. This model will be explicitly described in Section 3.3. Given the extended possibilities of the FAST model, a limited number of operating cases will be modelled. Table 2.2 includes a summary of all these cases, together with the mean wind speed at the location of the hub.

Case	Operating Regions	Wind speed (m/s)	Wave
FC1	1½ ↔ 2	7	-
FC2	2 ↔ 2½	9	-
FC3	2 ↔ 2½ ↔ 3	11	-
FC4	3	18	-
FC5	Standstill	18	-
FC6	3	18	on

Table 2.2: Simulated operational conditions in FAST model

The first four examined cases concern four different operating regions according to the controller (see Figure 3.17). It needs to mentioned that in the first three cases the turbine shifts between different operating regions, while in the 4th case, it operates explicitly inside Region 3. In particular, FC1 corresponds to low wind conditions, while FC2 and FC3 concerns intermediate wind speeds. Finally, FC4 refers to high wind speeds, above the rated wind speed. In general, in the cases where the OWT operates in Region 3, the rotational speed of the rotor has minor variations in time by regulating the blade pitch angle. Therefore, the time-invariance of the system depends on the pitching of the blade and not the influence of the rotor speed on the blade modes. Additionally, in all these cases, no wave has been considered in the analysis. The main reason is to purely investigate the decomposed effect of the waves and the harmonic content that originates from the rotor.

Then, in case FC5 the rotor is parked inside Region 3. Since the rotational speed in this case is zero, it is expected that no harmonic component due to the rotation of the rotor will be present in the response data. This conditions are not realistic, since the wind speed that was considered is below the cut-off, but the main purpose of this simulation is to apply the algorithms on FAST model in case where the input includes no harmonic components related to the rotation of the rotor.

Finally, FC6 is similar to FC4, but the structure is also loaded by waves. The main purpose of this simulation is to examine the influence of waves. However, as it will be explained in Section 3.3, the presence of waves in the response data was not significant. Therefore, wave was not included in the benchmark study.

3

SIMULATION OF DATA

Modelling offshore wind turbines aim at formulating a mathematical model that is able to capture all the physics of interest. The system should be as detailed as needed in order to take into account all the important parameters that are relevant to the purpose of the analysis. Hence, it is important to understand both the system and the loading conditions. In this chapter two models will be introduced, which have been used for the simulation of the measurement data. These data serve as input to the OMA algorithms. Before introducing those models, a short introduction to the relevant modelling/simulation considerations is presented. In Section 3.2 a simplified OWT model implemented in Matlab will be presented. The data simulated with this model will be used to verify the implemented OMA algorithms. Section 3.3 will introduce the implemented FAST model, which is a more realistic representation of an OWT. The data simulated with this model will be used to simulate different operational conditions that will be used in the benchmark study.

3.1. AN INTRODUCTION TO OFFSHORE WIND TURBINE STRUCTURES

Offshore wind turbines are structures with a high degree of complexity. Both loading conditions and foundations have attracted great scientific interest. The main components of an OWT are similar to those of an onshore wind turbine, but they are deigned to operate in the much harsher offshore environment. Moreover, the power capacity of an OWT is most of the times much larger than the capacity of onshore, with a much bigger and heavier rotor-nacelle assembly (RNA) as consequence. Additionally, one of the main challenges of OWTs is the type of the foundation. Monopile support structures are used most of the times, but more complex types also exist for larger depths.

3.1.1. OWT SYSTEM COMPONENTS DESCRIPTION

In short, the main components of an OWT are the RNA and the tower. A substructure supports the tower and connects it to the seabed via a transition piece. The substructure supports the tower and embeds it into the seabed. The most common way of foundation is a monopile structure. Other types ranging from a jacket structure to a floating support also exist and find application for larger water depths. The connection between the tower and the monopile is typically referred to as the transition piece. The RNA is composed of the nacelle and the rotor, where the first includes most of the electromechanical components and the latter is consisted of the blades and the hub, and is attached on the nacelle. Figure 3.1 can be used to graphically display the main components of an OWT[39]. In the remaining part of this section the individual components will be described briefly.

Blades

Initially, wind excites the blades thanks to the lift aerodynamic forces. These forces drive the turbine, as shown in Figure 3.2, [40]. The main target of the rotor is to capture the kinetic wind energy, maintain a certain rotation and deliver torque on the main (low-speed) shaft. The blades are designed to be light and long airfoils, commonly made of composite reinforced plastics material.

Furthermore, in order to optimize the behaviour of the blades and capture the kinetic wind energy in the most efficient way, the blades are designed to have a varying, twisted cross-section along their length, as shown in Figure 3.3, [40]. More in detail, this would change the apparent wind velocity over the length of

the blade. Close to the hub the apparent wind direction of the air passing over the blade is very different to the situation at the tip, since the apparent wind speed component introduced by the rotation is significantly lower. The predominant configuration for OWTs is the three-bladed rotor.

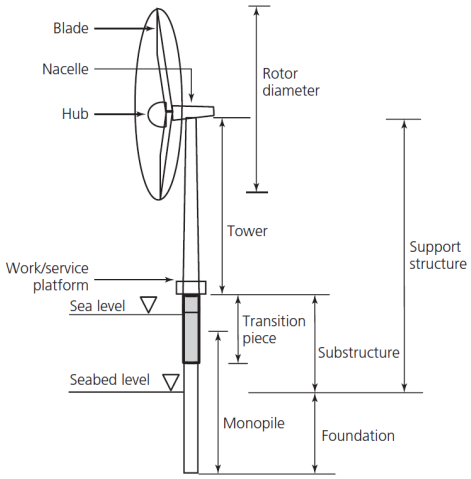

Figure 3.1: General configuration of an OWT monopile system

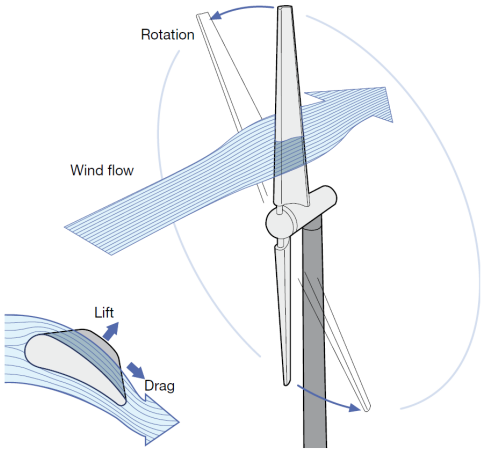

Figure 3.2: Wind aerodynamic lift and drag forces

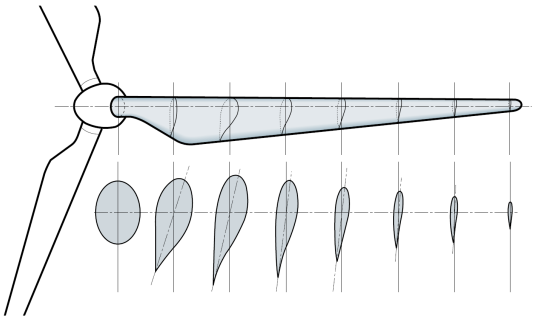

Figure 3.3: Blade cross-sections along blade length

Hub

The blades are connected via the hub to the main shaft. This component is supposed to transfer the loads from the blades to the drive train, and therefore it is expected to be highly stressed. The hub may also contain blade-pitch brakes in order to control the rotation of the rotor, if needed. These brakes work by pitching on and off the bladed such that the amount of generated lift and drag can be controlled. The reduction in the lift aims either at regulating the power production for wind speeds above the rated wind speed, or at parking the turbine for wind speeds above cut-off speed.

Drivetrain

Behind the blades and the hub, the low-speed (main) shaft (LSS) captures the wind energy in terms of rotational energy. The main purpose of this component is to transfer the torque through the gearbox to the high-speed shaft (HSS) (see Figure 3.4, [39]). The LSS is also a critical, highly loaded part, since it will be excited by the torque, generated by the rotor. Next, a gearbox is used in order to amplify the rotational speed of the LSS before converting the rotational mechanical energy into electrical power. This conversion is carried out by a generator that is connected at the end of the HSS. This array of mechanical and electrical parts forms the drivetrain. It should also be noted that this is one typical configuration. For the case of direct-drive generators, the main shaft is directly connect to the generator, without the use of a gearbox. In the end, the generator directs the generated power into the transformer.

Nacelle

All these components of the drivetrain are protected inside the nacelle, as displayed in Figure 3.4. This unit transfers all the aerodynamic loads from the rotor, but also the loads related to the generator and the brake systems to the tower. Nacelles are large and heavy units that accommodate also, apart from the drivetrain, mechanical brakes and other equipment. This whole configuration is able to rotate around the vertical axis thanks to the yaw control system that is located between the nacelle and the tower. This controls the direction of the rotor so that the wind turbine always aligns with the wind.

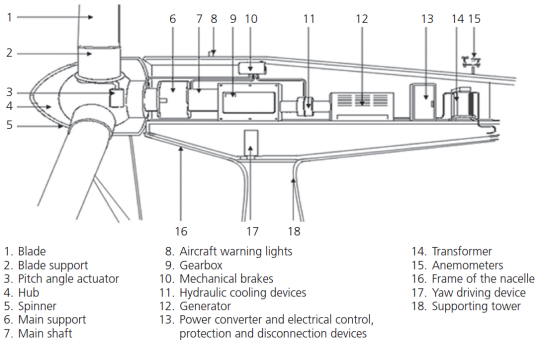

Figure 3.4: Main electromechanical components constituting OWT systems.

Tower

The last component of an OWT that will be discussed here is the tower. This is most of the times a tubular steel structure with varying diameter and thickness along the tower length. The tower is based on the substructure and transmits the loads applied on the nacelle to the foundation. The tower may also include devices that are used to monitor the structure (*e.g.* strain gauges, accelerometers, etc). Power cables, ladders and other equipment may also be present.

Substructure

As mentioned before, the whole RNA/tower assembly is based on the substructure. There are different types of substructures, depending mainly on the water depth (see Figure 3.5, [39]). The grounded designs include the gravity-based, monopile, tripod and jacket solutions. Monopiles are the most commonly used supports and correspond to waterdepth less than ~35m. Additionally, jackets are also very popular for intermediate waters. As wind turbines get larger, and move in deeper water, it becomes inefficient in terms of cost to choose a grounded support structure. Therefore, floating options like tension leg platforms or spar buoys more attractive.

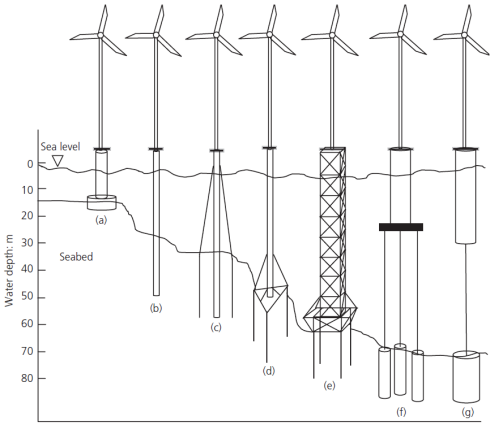

Figure 3.5: Types of substructure: (a) Gravity-based; (b) Monopile; (c) Monopile with guy wire; (d) Tripod; (e) Jacket; (f) Tension Leg Platform; (g) SPAR buoy

3.1.2. DESCRIPTION OF OWT LOADING CONDITIONS

In practice, OWTs are loaded mainly by wind, wave and current. Despite the fact that they are designed to operate under large wind speeds, wave loading may also cause the greatest force on the structure and be driving for the support structure design. In order to consider the loading due to the harsh environmental conditions in the analysis, at first the environmental conditions need to be modelled so that the main features of the wind and wave fields are accurately captured. By examining a short time interval (e.g. 10min), wind seems to have a dominant mean component and a stochastic, turbulent part. As far as wave and current is concerned, the first can be considered to have stochastic nature, while the second has minor fluctuations in time and, therefore, almost deterministic nature. A graphical representation of the environmental conditions can be displayed in Figure 3.6, [41]. Under these conditions, the structure will interact with the wind and wave field and will be excited by the aerodynamic and hydrodynamic loading.

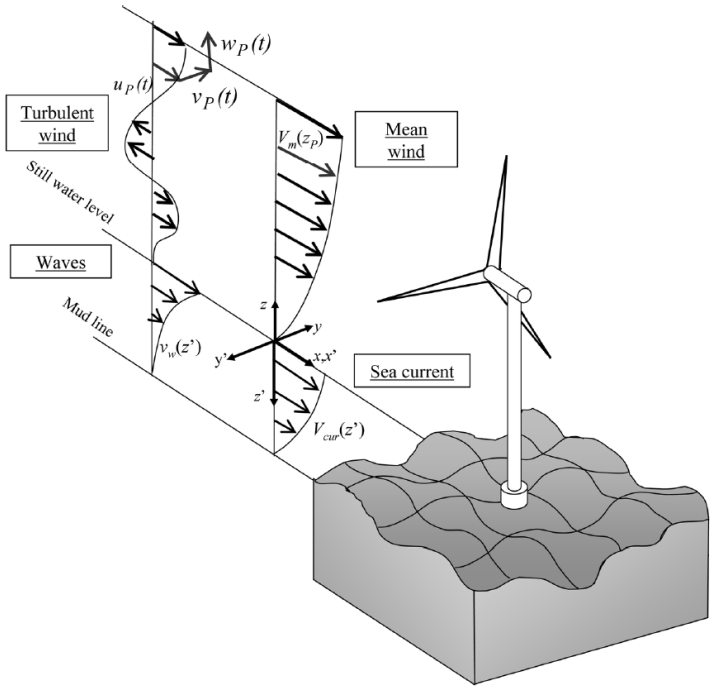

Figure 3.6: Modelling environmental conditions.

Wind loading

Modelling the wind field in a realistic and accurate way is vital for the simulation of the aerodynamic loading. In general wind field has a mean component that varies along the height above the sea surface, following an almost logarithmic trend. In many practical applications the short-term turbulent wind field is modelled using the Kaimal spectrum. This spectrum will also be used within the framework of this thesis. As it is shown in the Kaimal spectrum of Figure 3.7, wind velocity is described by a dominant mean component and by the turbulent, stochastic components that are spread over a wide range of frequencies. Using this spectrum, a stochastic spatial wind field can be generated. Once the wind velocities are specified, the loading on the blades can be determined. Blade Element Theory (BET) and Blade Element/Momentum (BEM)[42][43] theory are two popular methods that are able to determine the thrust wind force on the rotor. An in depth description of the derivation of the aerodynamic loading is out of the scope of this thesis. It is worth mentioning that the structure will not be loaded only at the top, but also along the tower by distributed drag forces.

Wave & current loading

As already stated, offshore wind turbines may also be significantly loaded by wave loads, since the frequency content of this excitation is in many designs closer to the first natural frequency of the structure. In contrast to wind, wave has energy over a shorter frequency range. Moreover, both wave and current contribute in the hydrodynamic loading. In general, a random wind-generated sea state is composed of a set of a

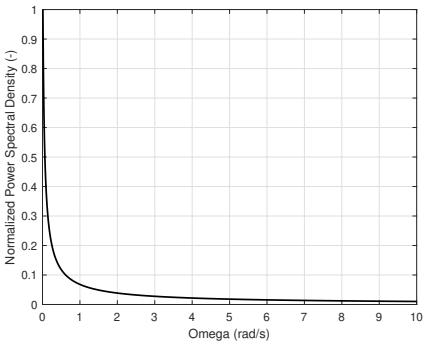

Figure 3.7: Kaimal Spectrum

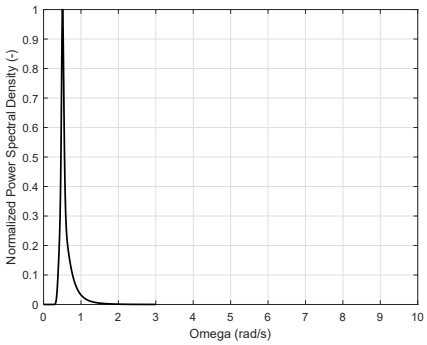

Figure 3.8: JONSWAP Spectrum

large number of harmonic, sinusoidal waves of different frequencies, directions, amplitudes and phases. The "JOint North Sea WAve Project" (JONSWAP) spectra[44] is an empirical way to model the energy distribution of waves over frequencies (see Figure 3.8. This spectrum is many times selected for practical applications, despite the fact that it is developed based on data derived from a large area over the North Sea. Additionally, the Pierson-Moskowitz[45] spectrum is another option in order to model the spectral energy distribution of the random ocean waves. Once these spectra are developed, then the waves can be modelled using wave theories. Airy's and Stokes theory are commonly used in practice to simulate the wave velocity and acceleration field. The linear Airy's theory is appropriate for small wave heights in deep waters (short waves with respect to the water depth), while Stokes theory may be preferred in cases of steeper waves in shallower waters. Using a wave theory, the hydrodynamic field may be determined. Therefore, once the particle kinematics are defined, the drag and inertia hydrodynamic forces can be calculated based on Morison equation. This is a common strategy that is followed in practice in order to find the wave and current loading that is applied on beam-like elements.

Harmonic loading from rotor

An OWT is not only under the wind and wave loading, but also under structural harmonic loads originated from rotating parts. More in detail, during operation, the input includes some harmonic components at frequencies that are related to the rotational frequency of the rotor. These periodic disturbances propagate from the rotor, through the drivetrain to the tower. Of course, once the rotational frequency is known, these harmonics have more or less known frequencies and can be recognized in the response spectrum.

There are multiple different sources that result in these periodic disturbances in an operating OWT. At first, it is obvious that the wind field is not uniform. More specifically, the mean wind velocity varies with height and, therefore, the blades close to the sea surface will be under smaller wind velocities than at larger heights. This phenomenon is called wind shear. Apart from this factor, yawed inflow and rotor tilt are also sources of disturbances, since the rotor plane in such cases is not perpendicular to the direction of the wind. Moreover, the tower is an obstruction that drops locally the wind velocity. By extension, the blade will experience reduced forces whenever it passes through the tower due to tower shadow effect. The last and main source of periodic disturbances that is related to the wind field has to do with the air turbulence. More in detail, while rotating, the blades pass though moving turbulent pockets. This phenomenon is called rotational sampling and leads into harmonic forces mainly at frequencies three times the rotational frequency (3P).

Except for the disturbances related to the wind field, the effect of gravity also results in loading that varies along a complete a revolution. Finally, developing three blades of the same mass with same center of mass and stiffness is almost impossible. Hence, such an imbalance of the blades will lead in a harmonic component at the frequency equal to the rotational frequency (1P).

To conclude, the disturbances discussed before have frequencies related to the fundamental rotational frequency of the rotor P. In particular, these harmonic components of the input will have energy at nP, where n is related to the number of the blades. For the case of an OWT with three blades, the harmonic input will include energy at 1P, 3P, 6P, etc. With regard to the above mentioned, during the design of an OWT, the fundamental natural frequency should be away from these harmonic components to avoid resonance. In general, 1P is close to the frequency band where the wave energy is gathered. A common practice is to design the structure so that the first natural frequency will be between 1P and 3P.

3.2. SIMULATED DATA USING MATLAB

The previous chapter described briefly an OWT structure, together with the loading that excites the system. In order to simulate the response of an OWT, a simple numerical model was developed in Matlab. This model will be used to simulate measurement data that will correspond to simplified physics. Afterwards, the selected OMA techniques will be applied on these data. The dynamic characteristics of the model can be specified exactly and, in that way, it will be possible to validate the applicability of the algorithms. Additionally, the responses considering wind, wave and current input can be used to check the influence of wave loading for this simple model.

3.2.1. SYSTEM DESCRIPTION

The numerical model developed in Matlab is a simple, 2D representation of an OWT and is able to generate dynamical responses in the fore-aft direction. The tower of this simplified OWT model is modelled as a clamped Euler-Bernoulli cantilever beam with constant diameter and thickness. Therefore, no soil-structure interaction is considered in the model. At the top of the tower, a concentrated mass equal to 350tn is added to model the RNA. The hub height is 107.6m and is identical with the tower length. Moreover, the tower has a diameter of 5m and thickness equal to 0.023m along its whole length. Finally, the blade length is 63m, leading in a rotor diameter equal to 126m. A graphical representation of the model can be shown in Figure 3.9. As far as the materials of the model is concerned, the tower is considered to be composed of steel with Young's modulus equal to 210GPa and density 8050kg/m^3. It has to be mentioned that the blades of the rotor are not physically considered in the model. However, the rotor diameter will be used in a later stage to derive directly the resultant thrust on the rotor.

The equation of motion (EoM) for the case of a continuous Euler-Bernoulli beam has the form of Eq. 3.1.

$$\rho A\ddot{w} + EIw'''' = q \tag{3.1}$$

where, ρ is the steel density, A is the cross-section area of the tower, E is the Young modulus, I is the cross-section moment of inertia and w is the deflection of the tower. In order to solve the equation of motion for random loading, a numerical model is derived by discretizing the continuous beam into 10 degrees of freedom (DoF), as shown in Figure 3.9. Then, the EoM takes an equivalent, discrete form using the principles of Finite Difference. The discrete form of the equation of motion can then be solved numerically in time-domain by applying the numerical Runge-Kutta method.

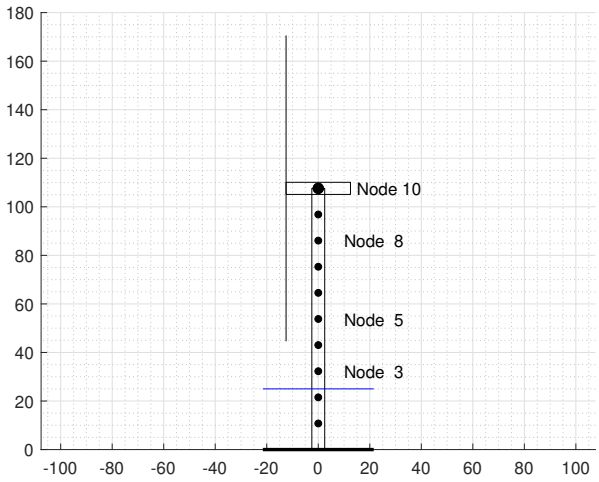

Figure 3.9: Graphical representation of the OWT model in Matlab

Once the discrete EoM is derived, the mass and stiffness matrices can be used to add Rayleigh damping in the model ($\mathbf{C} = \alpha_0\mathbf{M} + \alpha_1\mathbf{K}$). The values of α_0 and α_1 can be calculated in such a way, so that the modal damping ratios related to the first and second natural frequencies are 4% and 2%, respectively (see Eq.3.2).

$$\alpha_0 = \frac{2\omega_1\omega_2\left(\xi_1\omega_2 - \xi_2\omega_1\right)}{\omega_2^2 - \omega_1^2}$$
$$\alpha_1 = \frac{2\left(\xi_2\omega_2 - \xi_1\omega_1\right)}{\omega_2^2 - \omega_1^2} \tag{3.2}$$

The natural frequencies and the related damping ratios can be determined by solving the poly-eigenvalue problem in Matlab, using the mass, damping and stiffness matrices. Table 3.1 summarizes the resulting natural frequencies and the related damping ratios, while Figure 3.10 shows graphically the first four mode shapes of the system.

Mode (-)	Nat. Freq Damped (rad/s)	Damping Ratio (%)
1	1.155	4.000
2	12.303	2.000
3	37.305	5.089
4	73.332	9.832
5	116.923	15.623
6	163.976	21.891
7	210.156	28.051
8	251.261	33.539
9	283.578	37.857
10	304.205	40.614

Table 3.1: Modal properties of Matlab OWT model

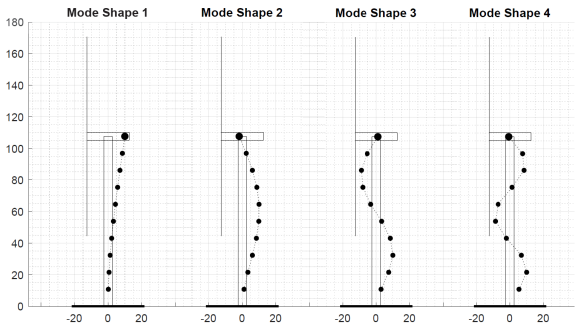

Figure 3.10: First four mode shapes of Matlab OWT model

Since the true modal characteristics of the system are known a priori, employing this Matlab OWT model will be in a later stage beneficial for the validation the OMA techniques.

3.2.2. EXAMINED LOADING CASES

Once the system is defined, the dynamic response can be derived by solving the ordinary differential equation. Different types of output (*e.g.* accelerations and strains) can be derived by post processing the obtained deflections. It needs to be mentioned that four nodes along the tower have been selected to be monitored. The location of these nodes, together with the resulting displacements in time-domain and accelerations in frequency-domain will be displayed for each of the four loading cases explained below.

Impulse loading

The first case corresponds to the special condition where all the nodes have the same initial velocity. In other words, all the DoF are excited by an horizontal unit impulse. This case is a free decay test and can be depicted in Figure 3.11. After approximately 100s, the deflection has almost been damped out. This can be used to decide on the time that will be truncated from the time-series of the other loading cases that will be examined in the coming paragraphs.

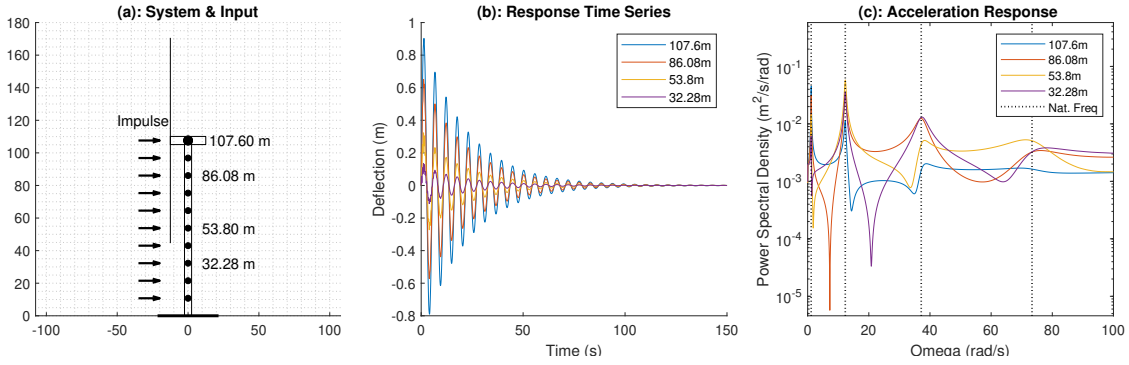

Figure 3.11: Response for Impulse loading case

Wind, wave & current loading

The second case considers that the model is subjected to wind, wave and current excitation. The aerodynamic loading is not considered in a detailed way in the model, but it is grossly simplified by a concentrated force at the top of the structure. This force represents the drag load due to wind, applied on the turbine's blades and can be calculated based on Eq. 3.3.

$$F_{top} = \frac{1}{2}\rho_{air} C_{d,top} A_{top} v_{top} |v_{top}| \tag{3.3}$$

In this expression, ρ_{air} is the air density, $C_{d,top}$ is the drag coefficient, A_{top} is the cross-sectional area of the rotor perpendicular to the flow direction ($= \pi D_{rot}^2/4$), D_{rot} is the rotor diameter and v_{top} is the wind velocity at the top of the structure. The wind velocity is simulated at the hub height using a Kaimal spectrum as input. In the simulations of the model, the average wind speed at the hub height is assumed to be `15m/s` and the turbulence intensity is considered equal to `20%`. Finally, the drag coefficient is considered to be `0.05`.

Apart from wind loading, hydrodynamic loading due to wave and current is also applied over the submerged part of the tower. At first, the waterdepth is selected to be equal to `25m`. A wave spectrum can be generated by considering that the irregular sea state has a significant wave height of `7m` and a peak period equal of `12.4sec`. In the next step, a `JONSWAP` wave spectrum can be developed using these two properties. This spectrum is used as the base in order to simulate a sea state with the aforementioned statistical properties. This can be done by summing up a large number of harmonics with random phase that corresponds to different frequency-amplitude sets derived from the spectrum. Then, the particle velocities and accelerations below the sea surface can be then determined using Airy's theory. Additionally, the particle velocity that is defined using Airy's theory will be superimposed to the current velocity. As far as the current velocity is concerned, the profile described in Eq. 3.4 is used to consider the effect of the current.

$$v_{cur}(z) = v_{cur,0}\left(\frac{z}{d}\right)^{1/7} \tag{3.4}$$

where $v_{cur}(z)$ is the current velocity at vertical location z and d is the waterdepth. The current velocity close to the sea surface is considered to be $v_{cur,0} =$ `0.5m/s`. The resulting hydrodynamic loading is calculated as the summation of the drag and inertia term, according to Morison equation (Eq. 3.5).

$$F_w = F_I + F_D = \rho_w(1+C_a)Va_w + \frac{1}{2}\rho_w C_d A v_{wc}|v_{wc}| \tag{3.5}$$

where, ρ_w, a_w and v_{wc} are the water density, the acceleration due to wave and the total velocity due to wave and current, respectively. The drag coefficient C_d and the added mass coefficient C_a are assumed to be `0.47` and `1`, respectively. Finally, A is the cross-sectional area of the tower perpendicular to the flow direction and V is the related volume.

The response of the system under wind, wave and current loading is obtained, assuming that F_w and F_{top} are applied on the structure. Figure 3.12 displays the nodes that are loaded due to wind and wave. Also, the same figure shows the displacement in time-domain and the accelerations in frequency-domain. This simulation is important to check the algorithms explained in the following for the case where an `OWT` is loaded by wind and wave, in a simplified manner.

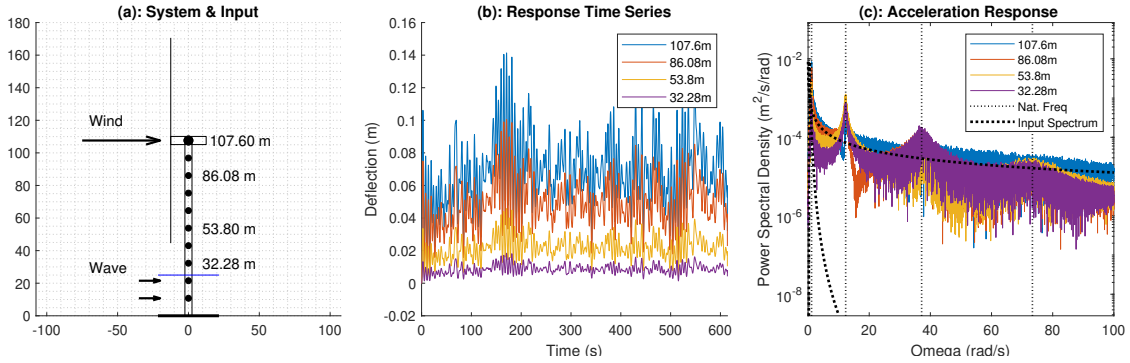

Figure 3.12: Response for Wind, Wave & Current loading case

Figure 3.13 is also exported in order to display clearly the range close to the first natural frequency, as both Kaimal and JONSWAP spectrums contain energy at that range. As it can be shown, wave has a minor influence in the response spectrum, as it has energy away from the first natural frequency of the system.

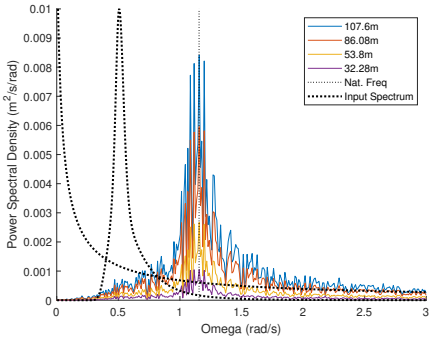

Figure 3.13: Acceleration response for Wind, Wave & Current loading case, zoomed at first mode

White noise loading

The third case corresponds to pure white noise excitation. In this fictional case, the rotor will loaded by a concentrated load on the top, based on Eq. 3.3. The flow velocity in this equation is modelled using a flat-spectrum with no mean component. This white noise signal was developed by adding up a large number of harmonics with same magnitude and random phase for a large number of frequencies below 200rad/s. Additionally, the tower will be loaded by a distributed white noise drag loading as expressed in the Morison equation (Eq. 3.5) using the same white noise flow velocity. In that way, the forces at the nodes along the tower will have same amplitude at every time instant. Practically, this loading is expected to enhance the excitation of modes at higher frequencies. In total, the top of the model receives larger loads than the nodes along the tower. The response for this case can be shown in Figure 3.14. As it is shown, the structure has an amplified response at the resonances.

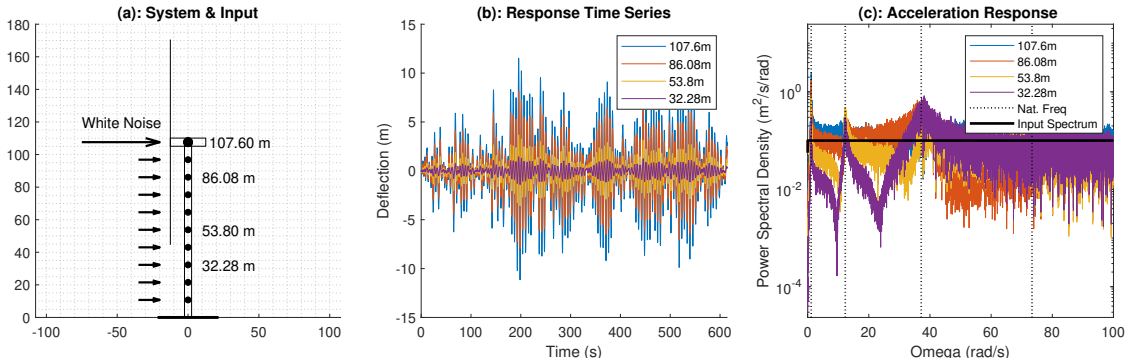

Figure 3.14: Response for White Noise loading case

White noise and harmonic loading

In the fourth case, the system is loaded by a force consisting of a random component, modelled as white noise signal, as well as several harmonic components at the top. An example is displayed in Figure 3.15. In this simulation, three harmonic components have been added at 10rad/s, 20rad/s and 30rad/s. The frequency of the harmonic components may vary according to the needs of the problem.

It needs to be mentioned that in all the cases, the system starts from equilibrium. In other words, the transient part is included in the response data. By looking into the free decay of Figure 3.11, one may notice that removing the first 100s is sufficient.

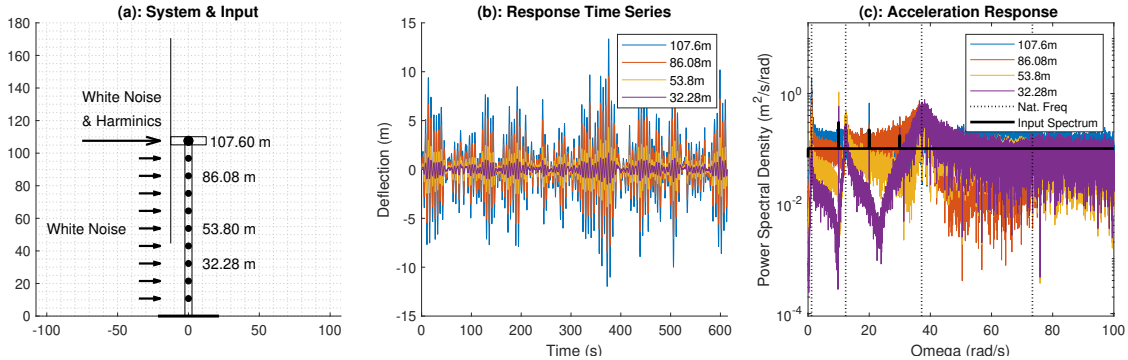

Figure 3.15: Response for White Noise with Harmonics loading case

3.3. SIMULATED DATA USING FAST

In this chapter, the "National Renewable Energy Laboratory (NREL) 5-MW baseline offshore wind turbine" will be introduced in terms of the main parameters, which have been used for the different simulation cases, as well as the corresponding simulation results. It will be shown that an operating turbine violates both the white noise and the LTI system assumption of OMA techniques. The measurements will be used later on to investigate the performance of the selected OMA algorithms for the case of operating OWTs.

This model was developed by NREL[46], as a composite from data obtained from different projects and can be used as a baseline for research. The response data will be simulated using the FAST v7.02 (Fatigue, Aerodynamics, Structures and Turbulence) aeroelastic and structural dynamics simulation code[47]. This software is open source and is widely used in the wind research community.

3.3.1. SYSTEM DESCRIPTION

The NREL 5-MW offshore wind turbine is a conventional three bladed OWT with a drivetrain that includes both LSS, a multiple-stage gearbox and a HSS series, as explained in Section 3.1.1. A feature of great importance that is included in the model is the present of a variable-speed and a variable blade-pitch-to-feather control system. More details about the model will be described below.

Structural geometry

Starting with the geometry of the structure, the blades have a length equal to 61.5m and are attached to the hub that is located 90m above the mean sea level (MSL). Moreover, the hub diameter is 3m, resulting in a total rotor diameter equal to 126m. It can be concluded that the hub is located 5m upwind of the tower centerline and 2.4m above the top of the tower (elevation of the yaw bearing). Next, the hub is connected to the drivetrain, which is modelled as one single equivalent shaft separating the hub and the generator. A more detailed configuration of the whole RNA, together with the tower can be shown in Figure 3.16. The values of each parameter displayed in Figure 3.16 are described and summarized in Table 3.2.

Parameter	Value	Description
TipRad	63.0 m	Distance from the rotor apex to the blade tip
HubRad	1.5 m	Distance from the rotor apex to the blade root
HubCM	0 m	Distance from rotor apex to hub mass
OverHang	-5.01910 m	Distance from yaw axis to rotor apex
ShftTilt	-5.0 deg	Rotor shaft tilt angle
PreCone	-2.5 deg	Cone angle of Blades
TowerHt	87.6 m	Height of tower above MSL
Twr2Shft	1.96256 m	Vertical distance from the tower-top to the rotor shaft

Table 3.2: RNA and tower geometry data

Regarding the weighs of several parts of the structure, the rotor and the nacelle weight is 110tn and 240tn, respectively. Also, the total tower mass is almost 347.46tn. It is worth mentioning that the RNA weighs as much as the tower.

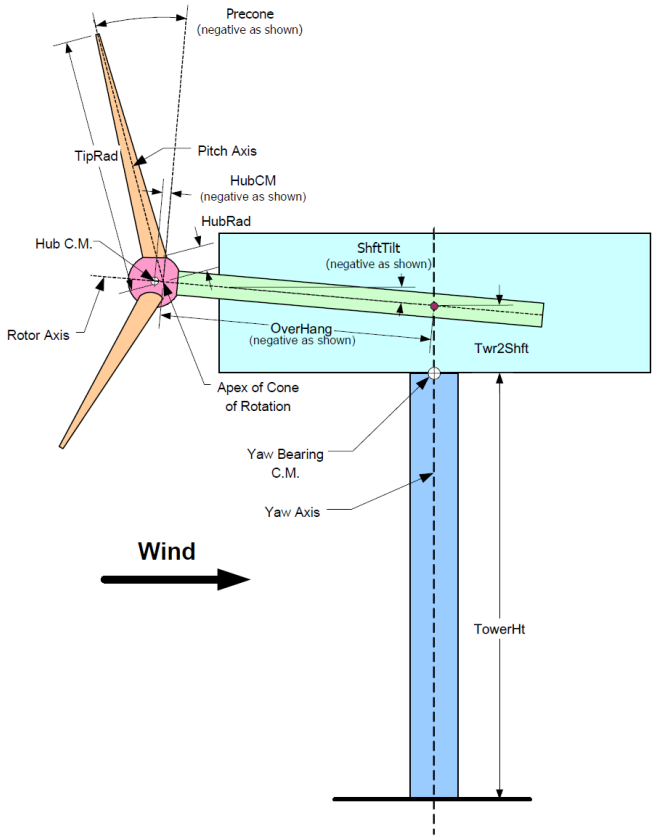

Figure 3.16: RNA and tower layout

Both the blades and the tower are discretized. Each blade has varying structural properties along its length. Edgewise and flapwise stiffness are defined for the discretized blade at each location along the pitch axis. In the same way, the tower structural properties vary along the tower length. More in detail, the diameter and thickness at the base are 6m and 27mm, respectively, while the related values at the top are 3.87m and 19mm.

Regarding the substructure of the turbine, the OC3 monopile foundation configuration has been selected for the purpose of this thesis. The substructure has been modelled in a very simplified way by assuming that the tower is fixed at the mudline, 20m below the MSL. This means that the total length of the tower and the monopile will be 107.6m (87.6m+20m). Finally, no transition piece was included in the model.

Controller

While running a simulation, FAST is also able to control specific output features based on a controller. The NREL 5-MW wind turbine controller that is included in the model is a variable-speed and variable blade-pitch-to-feather control system. The variable-speed generator torque controller aims at optimizing the power production for wind speeds below the rated value, while the collective blade-pitch-to-feather controller regulates the generator torque for wind speeds above the rated value by pitching off the blades, so that the power production will be as high as the capacity of the turbine.

The variable-speed control is an already existing controller in FAST and takes into account five regions, as shown in Figure 3.17. Region 1 is related to the case of idling rotor and very low wind speeds. The second zone is named as Region 1½ and is an intermediate zone between idling and Region 2. In Region 2, the rotor speed is regulated in such a way, so that the power production is optimum. In this zone, the generator torque applied to the HSS follows an exponential relation with the generator speed. The fourth region is named Region 2½ and describes a linear torque-speed transition between Region 2 and Region 3. Finally, in Region 3 the blade-pitch-to-feather controller takes over and the generator power is regulated to be constant for wind speeds larger than the rated wind speed. This is achieved by pitching out the blades and maintaining the rotational speed of the rotor.

It is important to keep in mind that Region 1½ starts when the wind speed reaches the cut-in value (3m/s). In the same way, Region 3 starts when the wind speed exceeds the rated wind speed (11.4m/s) and extends until the cut-out wind speed (25m/s). The rotor rotational speed inside this region is regulated to be constant and equal to 12.1rpm.

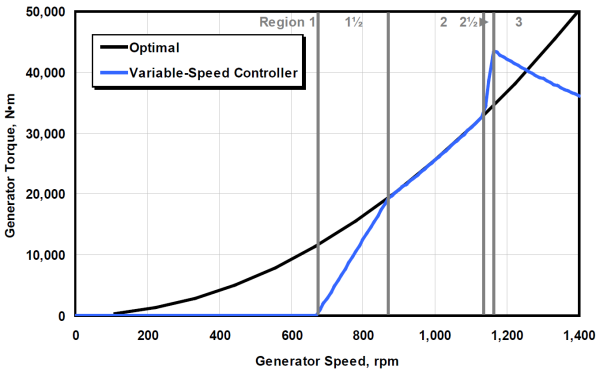

Figure 3.17: Generator Torque/Speed curve for variable-speed control

System DoFs

The model in FAST makes use of the modal properties of the flexible structural components and applies a combined modal and multi-body dynamic analysis. The system will be composed in total from 16 DoF. More in detail, FAST models the blades as beams, rigidly attached to the hub through a cantilever connection, with varying distributed mass and stiffness properties in the flapwise and edgewise direction. Using this information, the first two flap modes and the first edge mode can be defined. These modes are used to model the dynamic behaviour of each blade. For each of these three modes, three combinations (1 collective and 2 asymmetric) are considered leading to 9 blade mode DoF. In a similar way, the tower is also modelled using the first two modes in the fore-aft and the side-side direction. Hence, in total 4 tower bending-mode DoF are considered in the system to account for the tower flexibility. The next DoF corresponds to the drivetrain flexibility DoF that is associated with torsional motion between the generator and the hub. Another DoF that accounts for any variations in generator speed will be referred as Generator DoF. Finally, the last DoF is related to the yaw motion of the nacelle.

The tower and the blade modes are denoted with T and B, respectively. For the case of the tower, the fore-aft and side-side modes are differentiated using FA and SS. Therefore, T−FA2 is the second fore-aft bending tower mode. Additionally, the blade modes are distinguished using B1, B2 and B3 for each of the three blades. Finally, F1/F2 and E1 are used for the first/second flapwise and first edgewise bending blade modes, respectively. Table 3.3 shows the description of the DoF that are considered in the system and the related abbreviation.

Tower		*Blades*	
T-FA1	1st Tower fore-aft bending	B1-F1	1st flapwise bending (collective)
T-SS1	1st Tower side-to-side bending	B2-F1	1st flapwise bending (asymmetric)
T-FA2	2nd tower fore-aft bending	B3-F1	1st flapwise bending (asymmetric)
T-SS2	2nd tower side-to-side bending	B1-E1	1st edgewise bending (collective)
		B2-E1	1st edgewise bending (asymmetric)
Other		B3-E1	1st edgewise bending (asymmetric)
Yaw	Nacelle yaw	B1-F2	2nd flapwise bending (collective)
DrTr	Drivetrain rotational-flexibility	B2-F2	2nd flapwise bending (asymmetric)
		B3-F2	2nd flapwise bending (asymmetric)

Table 3.3: Description and abbreviations of Modes

Dynamic properties

After having defined the geometry and the dynamic characteristics of the structural components, the full system modes can be determined. The selected version of FAST includes a linearization functionality that

can be used to obtain the natural frequencies. Using this option, the non-linear, time-varying aeroelastic model is linearized around a periodic steady state operating point. More in detail, FAST uses the non-linear aeroelastic equation of motion of Eq.3.6.

$$\mathbf{M}(\mathbf{q},\mathbf{u},t)\,\ddot{\boldsymbol{q}}+\mathbf{f}(\mathbf{q},\dot{\boldsymbol{q}},\mathbf{u},\mathbf{u}_d,t)=0 \tag{3.6}$$

where, **M** is the mass matrix, **f** is the non-linear vector of forces, $\mathbf{q}/\dot{\boldsymbol{q}}/\ddot{\boldsymbol{q}}$ is the displacements/velocities/accelerations vector of the DoFs, and t is time. In this equation, the damping has been modelled as part of the loading and includes both structural and aerodynamic damping. Regarding the structural damping, a damping ratio of 0.47% has been used for the blade modes and 1.0% for the tower modes. As for the aerodynamic damping, it refers to the applied aerodynamic forces that depend on structural velocities.

During the linarization procedure, FAST determines at first numerically a periodic steady state solution by solving the equation of motion. Then, when the velocity and the displacement of the system converge to a constant value, FAST applies the linearization of the full system around that operating point. This procedure leads into the system matrix **A**. This matrix includes the mass, stiffness and damping matrices of the linearized system. It is expected that the damping matrix will be non-orthogonal. Therefore, the system possesses complex modes instead of real normal modes. Besides, the modal parameters of the turbine can be calculated by finding eigenvalues of the continuous-time state-matrix **A** with positive imaginary components. Then damping ratio is calculated by dividing the real part with the imaginary part. Finally, the damped natural frequencies can be directly obtained from the imaginary part of the eigenvalues.

Figure 3.18 shows a Campbell diagram, which can be used to illustrate possible resonances of the blade natural frequencies and excitations during operation. In this figure, the coloured, almost horizontal lines are the natural frequencies of the blades, and are plotted against the rotational speed of the rotor.

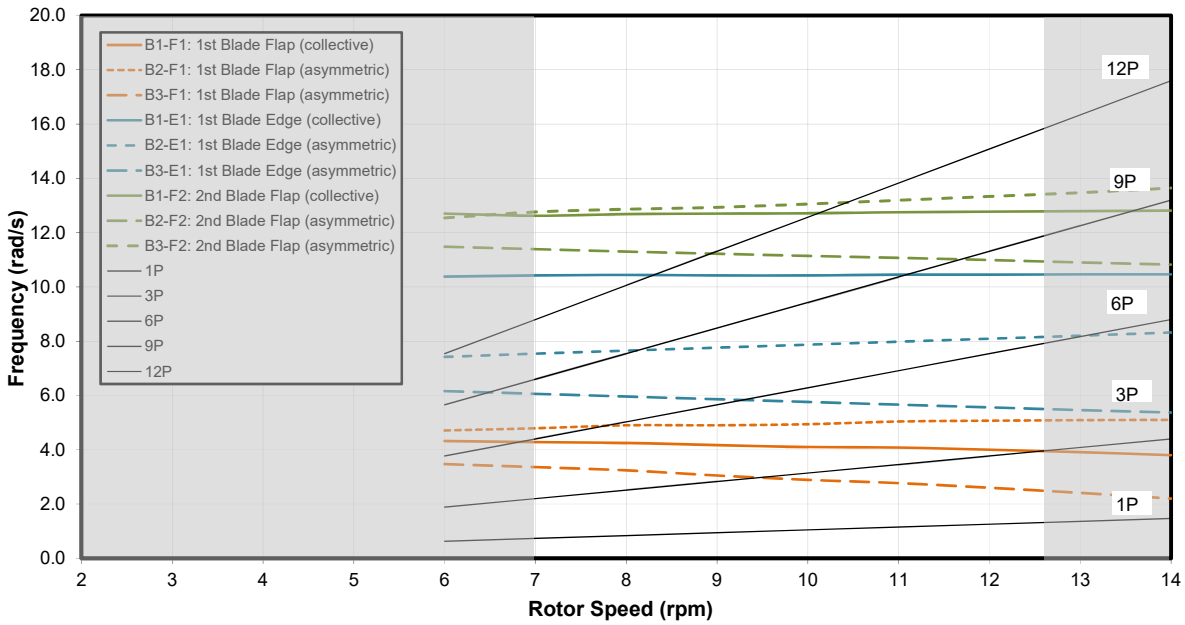

Figure 3.18: Campbell diagram of the NREL 5-MW baseline offshore wind turbine

As it can be deduced from the Campbell diagram, the natural frequencies of the blades vary with wind speed. This clearly indicates that the system is not an LTI system. For the examined 5-MW wind turbine, the flapwise and edgewise blade modes occur in the frequency range 0.5-2.0Hz. Table 3.4 summarizes the natural frequencies derived via the periodic linearization analysis for the different values of rotor rotational speed. This table will be used as a basis of the true dynamic characteristics of the system.

Similarly, the related damping ratios are summarized in Table 3.5. As mentioned before, the damping ratio includes both structural and aerodynamic damping. This can be deduced by looking into the increased damping ratio of the blades in the flapwise direction.

Rotor Speed	6	7	8	9	10	11	12	13	14	(rpm)
T-FA1	1.77	1.77	1.78	1.78	1.78	1.79	1.79	1.80	1.80	(rad/s)
T-SS1	1.77	1.77	1.77	1.77	1.77	1.77	1.77	1.77	1.77	(rad/s)
T-FA2	15.07	15.06	15.05	15.03	15.02	15.01	14.98	14.94	14.89	(rad/s)
T-SS2	14.95	14.95	14.95	14.95	14.95	14.95	14.95	14.95	14.95	(rad/s)
Yaw	38.29	38.34	38.37	38.33	38.33	38.36	38.36	38.35	38.36	(rad/s)
DrTr	24.65	24.58	24.53	24.61	24.63	24.60	24.62	24.64	24.67	(rad/s)
B1-F1	4.32	4.28	4.25	4.17	4.10	4.08	4.00	3.91	3.80	(rad/s)
B2-F1	4.71	4.79	4.90	4.90	4.94	5.04	5.07	5.09	5.10	(rad/s)
B3-F1	3.47	3.36	3.24	3.05	2.89	2.77	2.60	2.41	2.20	(rad/s)
B1-E1	10.38	10.42	10.44	10.42	10.42	10.45	10.45	10.46	10.46	(rad/s)
B2-E1	7.42	7.54	7.65	7.76	7.87	7.98	8.09	8.20	8.32	(rad/s)
B3-E1	6.16	6.06	5.96	5.86	5.76	5.66	5.56	5.46	5.37	(rad/s)
B1-F2	12.70	12.62	12.68	12.70	12.71	12.75	12.77	12.79	12.81	(rad/s)
B2-F2	11.48	11.39	11.30	11.22	11.14	11.07	10.99	10.90	10.82	(rad/s)
B3-F2	12.54	12.76	12.86	12.93	13.05	13.19	13.33	13.47	13.64	(rad/s)

Table 3.4: Natural frequencies per DoF for varying rotor speed values

Rotor Speed	6	7	8	9	10	11	12	13	14	(rpm)
T-FA1	4.7	5.2	5.8	6.5	7.1	7.5	8.0	8.5	9.0	(%)
T-SS1	0.5	0.5	0.5	0.5	0.5	0.5	0.5	0.5	0.6	(%)
T-FA2	2.2	2.4	2.7	3.0	3.3	3.6	3.9	4.3	4.6	(%)
T-SS2	1.5	1.4	1.4	1.5	1.5	1.5	1.5	1.5	1.5	(%)
Yaw	4.1	4.2	4.2	4.3	4.3	4.3	4.4	4.4	4.4	(%)
DrTr	5.6	5.6	5.6	5.7	5.7	5.7	5.7	5.8	5.8	(%)
B1-F1	28.3	31.5	34.2	40.7	45.2	47.2	51.5	55.8	60.0	(%)
B2-F1	26.0	28.3	30.3	35.4	38.7	39.9	43.0	46.0	49.0	(%)
B3-F1	34.4	38.9	42.9	52.0	58.5	62.0	68.2	74.0	79.5	(%)
B1-E1	2.1	2.1	2.1	2.1	2.2	2.2	2.2	2.2	2.2	(%)
B2-E1	0.8	0.8	0.8	0.9	0.9	0.9	0.9	0.9	0.9	(%)
B3-E1	1.0	1.0	1.1	1.1	1.2	1.2	1.3	1.3	1.4	(%)
B1-F2	7.5	7.4	8.5	10.0	11.1	11.9	13.0	14.1	15.2	(%)
B2-F2	8.0	8.9	9.9	11.7	13.2	14.0	15.4	16.9	18.3	(%)
B3-F2	6.9	8.2	8.4	9.7	10.4	10.5	11.2	11.9	12.5	(%)

Table 3.5: Damping ratio per DoF for varying rotor speed values

3.3.2. LOADING CONDITIONS

FAST v7.02 is used in order to run the analysis and simulate the response of the NREL 5-MW turbine under wind and wave loading. As explained in Section 3.1.2, wind and wave have frequency over a broad frequency region. However, most of the energy is mainly concentrated at frequencies below the first natural frequency. Additionally, the input spectrum is expected to include some harmonic components that originate mainly from rotational sampling. These harmonics have frequencies related to the rotational frequency of the rotor.

Wind loading

The aerodynamic loading in the Matlab model described in Section 3.2.2 has been largely simplified. On the other hand, FAST is able to model the aerodynamic loading in a more elaborated way. Initially, TurbSim is used for the generation of a stochastic, 3D turbulent wind field. This code creates a vertical rectangular grid matrix each point of which is characterized by a three dimensional wind speed vector. The hub of the rotor is located at the center of this rectangular grid frame. Once the grid is created, the wind velocities will be simulated based on International Electrotechnical Commission (IEC) 61400-x standards. The IEC Kaimal spectrum that is commonly used in practical applications is also used here as the wind spectral turbulence model. Moreover, a power law wind profile has been selected to simulate the mean wind component. The value of the mean wind speed for each simulation is different and was discussed in Section 2.2. In the next step, AeroDyn calculates aerodynamic loads based on the wind field on both the blades and tower. The aerodynamic loading is approximated by lift and drag forces concentrated at each node along the loaded element. Both blades and tower will be loaded by wind. During the aerodynamic analysis the blades are meshed into segments with varying aerodynamic properties. In total 17 blade nodes have been used. AeroDyn takes into account the influence of turbulence in an iterative way based on the quasi-steady Blade-Element/Momentum (BEM) theory. While determining the aerodynamic forces on the blades, an unsteady airfoil aerodynamic (UA) model will be

used to account for the effect of the dynamic stall in the lift and drag forces. As far as the aerodynamic loading on the tower is concerned, this can be simply calculated as using the drag part of the Morison equation.

Wave loading

Apart from the wind drag loading, the tower will also be directly loaded by waves. In the analysis both calm sea and irregular sea state can be simulated. In both cases, a water depth of 20m has been selected. At first, the irregular sea state is defined using a JONSWAP or Pierson-Moskowitz spectrum for a significant wave height equal to 5m and a spectral peak period equal to 12.4s. These values are default values, and would correspond to a sea state with both high wave height and wave period. The waves are assumed to propagate towards the rotor front. In other words, the direction of the waves is perpendicular to the rotor plane. Using this spectrum, an irregular sea state can be generated, with spectral energy below 1.5rad/s. In the next step, the full wave kinematics are generated using the linear Airy's theory. This theory is able to determine the kinematics only for the particles below the MSL. Therefore, the loading will be underestimated when a wave passes through the monopile. Wheeler stretching has been used to model the kinematics above the MSL by stretching the incident wave kinematics linearly to the instantaneous free surface. Finally, once the hydrodynamic field is specified, the relative form of Morison's equation can be used for the calculation of the hydrodynamic loading. The diameter of the tower in Morison's equation is considered to be 6m. Moreover, both the drag (C_d) and the added mass (C_a) coefficients are set to 1.

Harmonic loading from rotor

The effect of the rotating blades will also result in amplified responses around frequencies proportional to the rotor rotational frequency. The rotor is considered to have three identical blades, and therefore, the loading is not affected by any mass imbalances. Additionally, the wind direction is considered to be almost vertical to the rotor plane. In that case, the rotor tilt does not play an important role. However, harmonic excitation is expected to be amplified mainly due to wind shear and rotational sampling. Finally, the local influence of the tower on the wind field is not considered in the analysis.

A simulated case (FC1, see Section 2.2), where the system operates under relatively low wind speeds is examined as an example here. Under such wind conditions, the rotor will have a time-varying rotational speed, following the same trend as the wind speed, as shown in Figure 3.19(a). Furthermore, rotational sampling induces harmonic loads on the blades at frequencies, 1P, 2P, etc. This can be shown in Figure 3.19(b), which examines the spectrum of the normalized shear force applied at the root of the blade, perpendicular to the rotor frame. These harmonics, when combined with the related loading of the other two blades will lead in a total aerodynamic loading at the RNA with high harmonic content at frequencies 3P,6P, etc. Figure 3.19(c) shows the spectrogram of the acceleration that corresponds to the sensor at 97.3m height and reveals that there is indeed high energy close to 3P that follows the same trend with the rotor speed from Figure 3.19(a). Moreover, this energy decays when going to higher frequencies. It is obvious though that 3P, 6P, 9P and 12P has major contribution in the response spectrum. Finally, it is worth mentioning that the tower will not be excited 1P, since no mass imbalance is considered in the model.

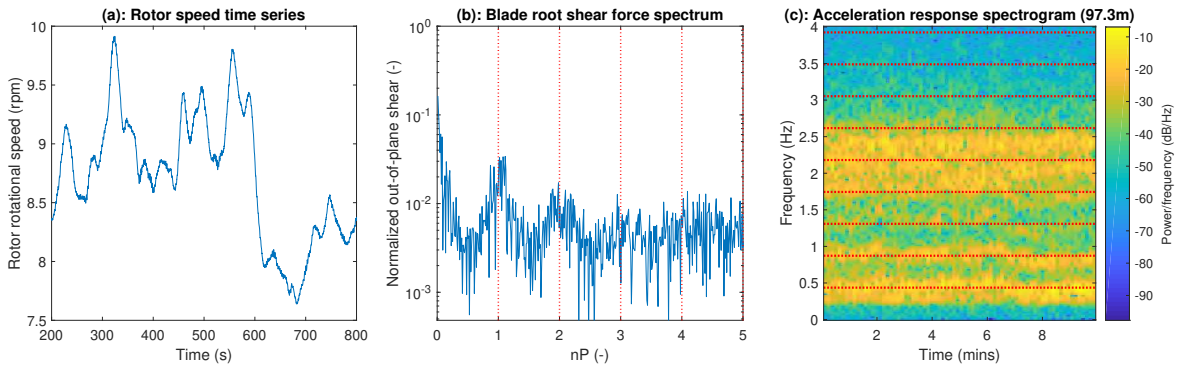

Figure 3.19: Effect of rotational sampling on the tower response (see FC1 in Section 2.2)

It needs to be mentioned that a parked rotor can be simulated by deactivating the controller. In that way, no harmonic excitation will be induced by the wind excitation.

Description of simulated data

Aiming for a typical 10min simulation, the duration of each analysis is 800s considering a truncation of the first 200s. This targets in removing any transient effect that is related to the fact that the system starts vibrating from equilibrium. The time-step in the simulation is 0.0125s and it corresponds to 80Hz sampling frequency. After running the analysis, FAST is able to provide the user with a variety of output results. The structure is monitored in the fore-aft direction using four accelerometers along the tower height. The location of these virtual gauges can be depicted in Figure 3.20. Accelerations are measured only in the direction of the mean wind speed. In the next chapters, the responses will be plotted in frequency domain when a stabilization diagram is used. In these diagrams, Node 1 refers to the sensor at 32.1m, Node 2 and Node 3 correspond to the accelerometers at 53.8m and 75.5m, respectively and Node 4 refers to the sensor at the top of the tower.

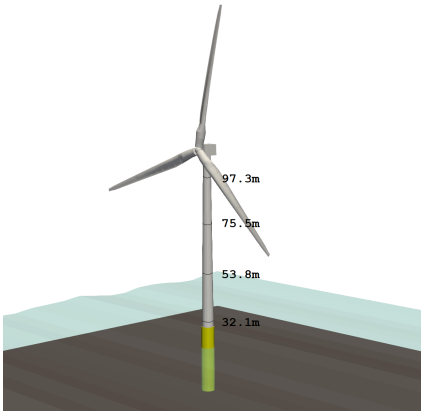

Figure 3.20: Location of accelerometers in FAST model

The acceleration response spectrum for each of the cases that will be analysed are shown in Figure 3.21. Apart from the response spectrum, these figures also include the tower modes (thick solid lines), the 1st flapwise bending blade modes (dashed lines), the 1st edgewise bending blade modes (dotted lines), the 2nd flapwise bending blade modes (dash-dot lines) and the 3P, 6P, 9P, etc. frequencies (red solid lines). When looking into the first four cases, one may conclude that the presence of 3P, 6P and 9P are dominant. Also, it is clear that the both the tower modes are excited. Similar high response is observed around the frequencies that correspond to the 2nd flapwise bending blade modes. In FC1, the first tower mode and the 3P harmonic are very close, but for higher wind speed (i.e. in FC4), this distance increases. The 1st flapwise and 2nd edgewise bending blade modes are mainly between 3P and 9P. Therefore, in all the operating cases these modes are more or less "covered" under the dominant harmonic part of the loading.

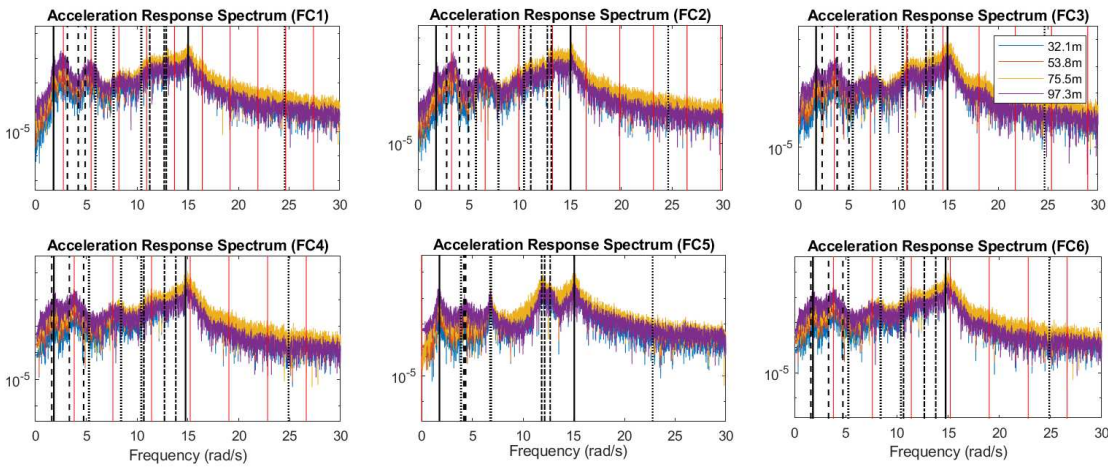

Figure 3.21: Acceleration response spectrum for each simulated case in FAST

Regarding FC6 case, the spectrum is almost identical to the spectrum of FC4. In particular, the responses at frequencies lower than the first fore-aft tower mode, where wave energy is concentrated, are quite identical with and without wave loading. Therefore, it can be concluded that the structure is very stiff with respect to wave loading. Keep in mind that the loading is applied close to the "node" of the first fore-aft mode, and in terms of controllability, it is difficult to amplify the response at frequencies close to the first tower mode.

4

EIGENSYSTEM REALIZATION ALGORITHM

The Eigensystem Realization Algorithm (ERA) is a popular time-domain modal parameter identification technique that is applied mainly on impulse response outputs. This algorithm applied together with the Natural Excitation Technique (NExT) is able to identify the modal properties of a system that operates under white noise excitation. In the first two sections of this chapter the theory behind ERA and NExT will be briefly explained. In the end of this chapter, this algorithm will be used to derive the natural frequencies and modal damping using the simulated data derived from the models in both Matlab and FAST. This chapter will be concluded with a chapter summary and concluding remarks on the usability of the ERA and NExT algorithm for operational offshore wind turbines.

4.1. THEORY BEHIND ERA

The Eigensystem Realization Algorithm (ERA) was developed in 1985 by J.N Juang and R.S Pappa[2][3] and is a time-domain system realization method. The mainn objective of ERA is to derive a realization of the system of interest using only the output measured data. However, ERA is derived for the case of systems exhibiting a free decay response. In other words, this technique aims at extracting the modal parameters of a system excited by an impulse-like input. Therefore, it seems that it is suitable for laboratory impact tests, where impact hammers or drop weights are used.

The unknown dynamical system is supposed to be an LTI system, described by the state-space expression shown in Eq.4.1. The first equation is named as discrete-time state equation, while the second is named as output (or observation) equation.

$$\begin{cases} \mathbf{x}_{k+1} = \mathbf{A}\mathbf{x}_k + \mathbf{B}\mathbf{f}_k \\ \mathbf{y}_k = \mathbf{C}\mathbf{x}_k + \mathbf{D}\mathbf{f}_k \end{cases} \tag{4.1}$$

In this expression, $\mathbf{x} \in \mathbb{R}^{nx1}$ is the state vector, $\mathbf{y} \in \mathbb{R}^{mx1}$ is the system output vector (*e.g.* acceleration measurement) and $\mathbf{f} \in \mathbb{R}^{rx1}$ is the system inputs (or control) vector (*e.g.* forces). Also the index k is used to determine the time step ($t_k = k\Delta t$) to which each vector refers, n is the order of the system (twice the number DoFs), and m is the total number of sensors. Regarding the rest matrices, $\mathbf{A} \in \mathbb{R}^{nxn}$ is the state (or system) matrix that expresses the dynamics of the system, $\mathbf{B} \in \mathbb{R}^{nxr}$ is the input (or control) matrix, $\mathbf{C} \in \mathbb{R}^{mxn}$ is the output matrix and $\mathbf{D} \in \mathbb{R}^{mxr}$ is the feed-through matrix that relates the input directly to the measurements. The main target of ERA is, given a set of measurements, to derive a realization of the system, or in other words the quadruple of the system state-space matrices **A, B, C** and **D**). Then, based on matrix **A** and **C**, the modal properties of the system will be derived.

Before describing the algorithm, it is vital to introduce the Markov parameters, as they are directly related to the impulse response of a system. Let's consider the case, where the system starts vibrating from zero initial conditions, for an impulse loading at one location. This means that at t =0, x_0 =0, $f_0$1 for the remaining time steps, f_k =0. In that way, the input vector is more or less defined for all the time steps. Substituting in Eq.4.2, the following relation is derived.

$$\begin{aligned}
\mathbf{x}_0 &= 0 & \mathbf{y}_0 &= \mathbf{C}\mathbf{x}_0 + \mathbf{D}f_0 = \mathbf{D}f_0 = \mathbf{Y}_0 f_0 \\
\mathbf{x}_1 &= \mathbf{A}\mathbf{x}_0 + \mathbf{B}f_0 = \mathbf{B}f_0 & \mathbf{y}_1 &= \mathbf{C}\mathbf{x}_1 + \mathbf{D}f_1 = \mathbf{C}\mathbf{B}f_0 = \mathbf{Y}_1 f_0 \\
\mathbf{x}_2 &= \mathbf{A}\mathbf{x}_1 + \mathbf{B}f_1 = \mathbf{A}\mathbf{B}f_0 & \mathbf{y}_2 &= \mathbf{C}\mathbf{x}_2 + \mathbf{D}f_2 = \mathbf{C}\mathbf{A}\mathbf{B}f_0 = \mathbf{Y}_2 f_0 \\
\mathbf{x}_3 &= \mathbf{A}\mathbf{x}_2 + \mathbf{B}f_2 = \mathbf{A}^2\mathbf{B}f_0 & \mathbf{y}_3 &= \mathbf{C}\mathbf{x}_3 + \mathbf{D}f_3 = \mathbf{C}\mathbf{A}^2\mathbf{B}f_0 = \mathbf{Y}_3 f_0
\end{aligned} \tag{4.2}$$

This is a direct relation of the measurements time series (vector $\mathbf{y}$) to the fundamental system properties, named as Markov parameters and the input. In a shorter expression, a matrix of Markov parameters can be written as $\mathbf{Y}_0 = \mathbf{D}$, and $\mathbf{Y}_k = \mathbf{C}\mathbf{A}^{(k-1)}$ for $k > 0$. ERA takes advantage of this relation and aims at determining these system matrices based on the measured time series of $\mathbf{y}$. Amongst the four matrices of the system, only **ABC** need to be determined, as $\mathbf{D}$ is directly related to the initial values of the measurements.

In upcoming part, the algorithm will be presented in a step wise fashion. The algorithm is broken down in seven 7 steps, which will be explained having an actual implementation of the algorithm in mind.

Step 1 - Hankel Matrix

In the first step of ERA, two block-Hankel matrices will be formed. A general expression of this matrix $\mathbf{H}_{k-1} \in \mathbb{R}^{mpxrq}$ is shown in Eq.4.3. In that expression, $p \geq n$ and $q \geq n$ denote the number of blocks in the vertical and horizontal direction, respectively. This means that the bottom right block will refer to a time step $k+p+q-2$.

$$\mathbf{H}_{k-1} = \begin{bmatrix} \mathbf{Y}_k & \mathbf{Y}_{k+1} & \cdots & \mathbf{Y}_{k+q-1} \\ \mathbf{Y}_{k+1} & \mathbf{Y}_{k+2} & \cdots & \mathbf{Y}_{k+q} \\ \vdots & \vdots & \ddots & \vdots \\ \mathbf{Y}_{k+p-1} & \mathbf{Y}_{k+p} & \cdots & \mathbf{Y}_{k+p+q-2} \end{bmatrix} \tag{4.3}$$

In the expression above, $\mathbf{Y}_k \in \mathbb{R}^{mxr}$ is one block of the Hankel matrix. Each block is represented by the measurement data of a given time step k, as shown in Eq.4.2. Therefore, the block-Hankel matrix can be directly constructed based only on the free decay measurements that are available. It has to be noted that for multiple inputs r, each block in the Hankel matrix will have dimension mxr. These blocks can be calculated as $\mathbf{Y}_k = \mathbf{y}_k \mathbf{f}_0^+$, where $\mathbf{f}_0$ is the impulse vector and $(\bullet)^+$ denotes the Moore-Penrose pseudo-inverse of a matrix. Due to the fact that the impulse input is most of the times unknown, one may directly use a single vector $\mathbf{y}_k$ to express $\mathbf{Y}_k$. This case is similar to assuming that the system is loaded by a single input (scalar f_0). Hence, the identified matrix $\mathbf{B}$ will be a $nx1$ vector $\mathbf{b}$. The latter case also matches to the conditions of a single impulse at one location, which is very common in practice. In the extends of system identification, matrix $\mathbf{B}$ does not play an important role and a single vector $\mathbf{y}_k$ can be used to represent each block of the Hankel matrix.

Based on Eq.4.3, two expression of the block-Hankel matrix will be derived and used for the identification. These will refer to two consecutive time steps. Thus, The first block-Hankel matrix $\mathbf{H}_0$ will be formed for $k = 1$, while the second $\mathbf{H}_1$ will be shifted one time step ($k = 2$). These two matrices will be used as the basis for obtaining a realization of the dynamical system. Unfortunately, the direct transmission matrix $\mathbf{D}$ is not included in the Hankel matrix. This is a direct outcome from the fact that the input is considered to be an impulse.

Step 2 - Observability and controllability matrices

An important observation is that the block-Hankel matrix $\mathbf{H}_0$ can be written as the product of the matrix $\mathbf{P} \in \mathbb{R}^{pmxn}$ and $\mathbf{Q} \in \mathbb{R}^{nxqr}$, which are the observability and controllability matrices, respectively. This simple derivation can be briefly displayed in Eq.4.4.

$$\begin{aligned}
\mathbf{H}_0 &= \begin{bmatrix} \mathbf{Y}_1 & \mathbf{Y}_2 & \cdots & \mathbf{Y}_q \\ \mathbf{Y}_2 & \mathbf{Y}_3 & \cdots & \mathbf{Y}_{q+1} \\ \vdots & \vdots & \ddots & \vdots \\ \mathbf{Y}_p & \mathbf{Y}_{p+1} & \cdots & \mathbf{Y}_{p+q-1} \end{bmatrix} = \begin{bmatrix} \mathbf{C}\mathbf{B} & \mathbf{C}\mathbf{A}\mathbf{B} & \cdots & \mathbf{C}\mathbf{A}^{q-1}\mathbf{B} \\ \mathbf{C}\mathbf{A}\mathbf{B} & \mathbf{C}\mathbf{A}^2\mathbf{B} & \cdots & \mathbf{C}\mathbf{A}^{q}\mathbf{B} \\ \vdots & \vdots & \ddots & \vdots \\ \mathbf{C}\mathbf{A}^{p-1}\mathbf{B} & \mathbf{C}\mathbf{A}^{p}\mathbf{B} & \cdots & \mathbf{C}\mathbf{A}^{p+q-2}\mathbf{B} \end{bmatrix} = \\
&= \begin{bmatrix} \mathbf{C} \\ \mathbf{C}\mathbf{A} \\ \vdots \\ \mathbf{C}\mathbf{A}^{p-1} \end{bmatrix} \begin{bmatrix} \mathbf{B} & \mathbf{A}\mathbf{B} & \cdots & \mathbf{A}^{q-1}\mathbf{B} \end{bmatrix} = \mathbf{P}\mathbf{Q}
\end{aligned} \tag{4.4}$$

In the same way, Eq.4.5 can be used in order to express also the shifted block-Hankel matrix $\mathbf{H}_1$ as a function of $\mathbf{P}$ and $\mathbf{Q}$.

$$\mathbf{H}_1 = \begin{bmatrix} \mathbf{Y}_2 & \mathbf{Y}_3 & \dots & \mathbf{Y}_{q+1} \\ \mathbf{Y}_3 & \mathbf{Y}_4 & \dots & \mathbf{Y}_{q+2} \\ \vdots & \vdots & \ddots & \vdots \\ \mathbf{Y}_{p+1} & \mathbf{Y}_{p+2} & \dots & \mathbf{Y}_{p+q} \end{bmatrix} = \begin{bmatrix} \mathbf{CAB} & \mathbf{CA^2B} & \dots & \mathbf{CA}^q\mathbf{B} \\ \mathbf{CA^2B} & \mathbf{CA^3B} & \dots & \mathbf{CA}^{q+1}\mathbf{B} \\ \vdots & \vdots & \ddots & \vdots \\ \mathbf{CA}^p\mathbf{B} & \mathbf{CA}^{p+1}\mathbf{B} & \dots & \mathbf{CA}^{p+q-1}\mathbf{B} \end{bmatrix} = \mathbf{PAQ} \tag{4.5}$$

At this step it needs to be highlighted that all the system states of interest $\mathbf{x}_k$ need to be controllable (excited) and observable. As described in [3], the system is observable and controllable if and only if matrix $\mathbf{P}$ and $\mathbf{Q}$ have rank n, respectively. Practically, the state equation is considered to be non-controllable when a force is applied at a node of a given mode. In other words, a force applied at a node of the mode cannot control the related mode and reproduce the corresponding state. In a similar way, the output equation is considered to be non-observable when a sensor is located at a node of a mode.

For the special case of noise-free output, the rank of $\mathbf{H}_0$ is n, and is also equal to the order of the system. Unfortunately, the most common case is when measurement noise is present in the outputs. Therefore, matrix $\mathbf{H}_0$ is commonly of full rank. More details about defining the true system order will be given in the next step.

Step 3 - Singular Value Decomposition

In the second step, ERA factorizes the block-Hankel matrix $\mathbf{H}_0$ using singular value decomposition (SVD). Using SVD is a possible way to decompose the Hankel matrix and obtain a new relation as shown in Eq.4.6. In the last part of this equation it can be deduced that an expression of both the observability and the controllability matrices can be obtained.

$$\mathbf{H}_0 = \mathbf{USV}^T = \left(\mathbf{US}^{1/2}\right)\left(\mathbf{S}^{1/2}\mathbf{V}^T\right) = \mathbf{PQ} \tag{4.6}$$

where, $\mathbf{U} \in \mathbb{R}^{mpxmp}$ is the matrix of the left-singular vectors, $\mathbf{V} \in \mathbb{R}^{rpxrp}$ is the matrix of the right-singular vectors and $\mathbf{S} \in \mathbb{R}^{mpxrp}$ includes the singular values of $\mathbf{H}_0$. The non-zero singular values of matrix $\mathbf{S}$ characterize the true system order (number of dynamic states in the system). Under ideal conditions, where no measurement noise is present in the response data, the first n singular values will be the only non-zero elements of the $\mathbf{S}$ matrix. However, these noise-free data are observed at extremely rare, perfect conditions.

In fact, when using real data, all the diagonal terms of $\mathbf{S}$ matrix are non-zero. This happens due to the influence of noise and complicates the identification since the order of the system defines the dimension of the resulting realization. In order to approximate the true order of the system, the smallest singular values are truncated from $\mathbf{S}$ matrix. Unfortunately, most of the times there is no clear gap in the singular values that will indicate the point of the truncation. Hence, instead of trying to find the true order of the system, the algorithm is most of the times applied iteratively in order to build a stabilization diagram that relates the identified modes to the order that has been considered in each iteration. The true order of the system is important, but not the target of the identification and a stabilization diagram may overcome this barrier.

Step 4 - Truncation

Considering that the elements of matrix $\mathbf{S}$ are sorted in a descending order, then the first n singular values will be the most important and will be retained, while the rest will be truncated. Therefore, Eq.4.6 does not hold precisely, but approximately. Using the truncated matrices, the Hankel matrix $\mathbf{H}_0$ can be derived in a same way, as shown in Eq.4.7.

$$\mathbf{H}_0 \approx \mathbf{U}_n\mathbf{S}_n\mathbf{V}_n^T = \left(\mathbf{U}_n\mathbf{S}_n^{1/2}\right)\left(\mathbf{S}_n^{1/2}\mathbf{V}_n^T\right) = \mathbf{P}_n\mathbf{Q}_n \tag{4.7}$$

where, $\mathbf{U}_n \in \mathbb{R}^{mpxn}$, $\mathbf{V}_n \in \mathbb{R}^{rpxn}$ and $\mathbf{S}_n \in \mathbb{R}^{nxn}$ are the truncated versions of the matrices obtained by applying SVD on $\mathbf{H}_0$. As it is shown in the dimensions of these matrices, $\mathbf{S}$ is replaced by the diagonal $\mathbf{S}_n$ matrix, and the two matrices that include the singular vectors have been constructed by retaining the first n columns.

Step 5 - System realization matrices

In this step, the system realization matrices (**A**, **B** and **C**) will be calculated based on the expressions of Eq.4.7 and Eq.4.5. Due to the fact that only a small part of the singular values was kept, the resulting realization is referred to as the "minimum realization" that is used to express the system. At first matrix **A** can be determined as presented in the Eq.4.8, below.

$$\begin{aligned} \mathbf{H}_1 = \mathbf{PAQ} = \mathbf{U}_n\mathbf{S}^{1/2}\mathbf{AS}^{1/2}\mathbf{V}_n^T \rightarrow \\ \mathbf{A} = \mathbf{S}^{-1/2}\mathbf{U}_n^T\mathbf{H}_1\mathbf{V}_n\mathbf{S}^{-1/2} \end{aligned} \tag{4.8}$$

It should be noted that, **A** is one possible realization of the state matrix. In general, any unknown system has infinite possible realizations that may be used to predict the output from a specific input. However, this does not affect the identification, since the eigenvalues of **A** are preserved.

Then, the expressions of **B** and **C** can be determined in a very straightforward way, by just looking into the observability and controllability matrices of Eq.4.4. As it can be deduced, both the matrices **B** and **C** are just a part of the controllability and observability matrices, respectively. More in detail, the top mxn part of the observability matrix **P** (first mxn block) is equal to **C**, and the first n columns of **Q** are equal to **B** (first nxr block).

Step 6 - Eigenvalue problem

All the system properties are included in the realized state matrix **A**. In order to obtain the modal properties of the system, the eigenvalue problem is initially solved for matrix **A** ($\boldsymbol{A} = \boldsymbol{\Psi}_d\boldsymbol{\Lambda}_d\boldsymbol{\Psi}_d^{-1}$). Then two matrices will be obtained that will include the eigenvalues ($\boldsymbol{\Lambda}_d \in \mathbb{C}^{nxn}$) and the eigenvectors ($\boldsymbol{\Psi}_d \in \mathbb{C}^{nxn}$) as shown in Eq.4.9.

$$\begin{aligned} \boldsymbol{\Lambda}_d = diag\left(\lambda_1, \lambda_2, \ldots, \lambda_n\right) \\ \boldsymbol{\Psi}_d = \left[\boldsymbol{\psi}_1, \boldsymbol{\psi}_2, \ldots, \boldsymbol{\psi}_n\right] \end{aligned} \tag{4.9}$$

where, $\lambda_1, \lambda_2, \ldots, \lambda_n$ are the eigenvalues that correspond to $\boldsymbol{\psi}_1, \boldsymbol{\psi}_2, \ldots, \boldsymbol{\psi}_n$ eigenvectors. After deriving the eigenvalues, they will be converted from discrete-time to continuous time domain using the expression of Eq.4.10.

$$\begin{aligned} \boldsymbol{\Lambda} = \ln\left(\boldsymbol{\Lambda}_d\right)/\Delta t \\ \boldsymbol{\Psi} = \boldsymbol{\Psi}_d \end{aligned} \tag{4.10}$$

The damped natural frequency and the modal damping ratios of the system can be determined from the real and the imaginary part of each obtained complex pair of eigenvalues as shown in Eq.4.11 and Eq.4.12.

$$\omega_{d,i} = Im\left(\lambda_i\right) \tag{4.11}$$

$$\zeta_i = -\frac{Re\left(\lambda_i\right)}{|\lambda_i|} \tag{4.12}$$

The mode shapes $\boldsymbol{\Phi}$ at the locations of the sensors can be obtained by multiplying the eigenvectors with the output matrix **C**.

$$\boldsymbol{\Phi} = \mathbf{C}\boldsymbol{\Psi} \tag{4.13}$$

Finally, the modal participation factor can also be derived using the mode shapes $\boldsymbol{\Psi}$ and the realization of **B**, but deriving this factor is out of this thesis scope.

Step 7 - Filter the Stabilization diagram

When ERA was developed, several attempts were made to remove the influence of noise in the identification[48]. One suggested way to quantify the degree of modal purity of an identified mode and remove "noise" modes is to use a Modal Amplitude Coherence (MAC) factor. This factor is a measure of how much a mode is excited by a specific input. The expression of this factor is shown in Eq.4.14 and is the dot product (or coherence) of two vectors. The first vector is composed from a number of modal amplitude time-steps related to the identified mode, while the second is an ideal, extrapolated vector based on the impulse response data and the given identified eigenvalue. More details about can be found in [48] and [3].

$$MAC = \frac{|\tilde{\boldsymbol{q}}_i \boldsymbol{q}_i^*|}{\sqrt{|\tilde{\boldsymbol{q}}_i \tilde{\boldsymbol{q}}_i^*||\mathbf{q}_i \mathbf{q}_i^*|}} \tag{4.14}$$

Through the development of ERA, it is clear that the analyst needs to take several decisions. One of those is the number of rows p and columns q that are used when forming the block-Hankel matrix. Additionally, it is suggested to use a stabilization diagram for multiple iterations on the order of the system in order to avoid taking decisions on the truncation of the singular values.

Other ERA-based algorithms found in literature

The strategy that was followed in the present thesis is to use ERA together with NExT. However, Juang[3] proposed an alternative approach of ERA, known as Eigensystem Realization Algorithm with Data Correlation (ERA/DC). As mentioned by Juang, ERA/DC forms two square data correlation matrices $\mathbf{R}_{hh}(0) = \mathbf{H}(0)\mathbf{H}(0)^T$ and $\mathbf{R}_{hh}(1) = \mathbf{H}(1)\mathbf{H}(0)^T \in \mathbb{R}^{pmxpm}$. These are smaller matrices and thus it requires less computational time than ERA. In general the identification procedure is the same, but the data correlation matrices are used instead of the two block-Hankel matrices.

This classical identification algorithm was modified by Mohanty and Rixen[21], in order to be able and obtain the modal parameters of a system for the case where a harmonic excitation component is present, with known frequency that is close to the natural frequency of a mode. Thus, they focused on removing the influence of harmonic excitation. However, the simulated data from the examined operational conditions in the OWT model in FAST, has a broader frequency range over which harmonic excitation is present in the response. Therefore, the modified version of ERA algorithm was not included in the benchmark study.

4.2. NATURAL EXCITATION TECHNIQUE

In the description of ERA, it is clear that the algorithm works for impulse input. However, in many practical cases, the structures are tested under random ambient excitation. Therefore, ERA cannot be applied directly on response data, which are caused by stochastic inputs. The solution to that problem came when G. James et al.[6] suggested the so-called Natural Excitation Technique (NExT). This technique triggered the application of IRF-based algorithms on white noise input. ERA is such an algorithm and therefore, ERA/NExT can be considered to be the "OMA version" of ERA.

The underlying idea of NExT is that the cross-correlation function of the response will have the same properties as an impulse response, assuming that the input is a white noise stochastic process. The correlation function $R_{ij}(t)$ between the outputs i and j can be expressed by Eq.4.15. The theoretical derivation of this equation can be found in [6].

$$R_{ij}(t) = \sum_{l=1}^{n} \frac{\psi_{il} G_{j,l}}{m_l \omega_{d,l}} \exp\left(-\zeta_l \omega_{n,l} t\right) \sin\left(\omega_{d,l} t + \theta_l\right) \tag{4.15}$$

In this equation, ψ_{il} is the i^{th} element of eigenmode l, $G_{j,l}$ is a constant multiplier related to the input, m_l is the l^{th} modal mass, $\omega_{d,l}$ is the l^{th} damped natural frequency, $\omega_{n,l}$ and ζ_l are the l^{th} undamped natural frequency and modal damping ratio, respectively. Finally, θ_l is a random phase. By looking into this expression, it can be concluded that this summation of decaying sinusoids is similar to the response of the system at output i, when it is excited by an impulse at node j. In other words, $R_{ij}(t)$ describes the free decay of an output i of a single-input-multiple-output (SIMO) multiple degree of freedom (MDoF) system loaded by an impulse at input j.

Practically, once the measurement data (*e.g.* strains, accelerations, etc) have been collected, the auto and cross-correlation functions of the responses using a reference response are first derived. An example can be

shown in Figure 4.1, where the responses of a system loaded by white noise are converted into the related correlation functions using a single reference signal.

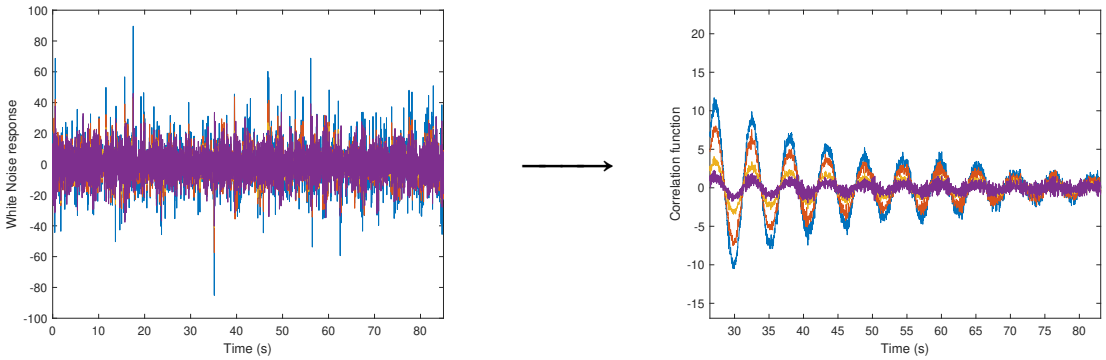

Figure 4.1: White noise and related auto/cross-correlation functions for a single reference signal (from 4 sensors of model in Matlab

In the next step, ERA will be applied on the correlation functions, by considering a minor modification. As described in Eq.4.16, the Markov parameters can be derived directly from the responses of the system. Here, multiple reference signals will be used, and in particular all the responses will be taken into account. Therefore, for each response signal, a set of m correlation functions will be derived. The Markov parameters for the time step k can be derived as explained in Eq.4.2.

$$[\mathbf{y}_k^1\, \mathbf{y}_k^2 \cdots \mathbf{y}_k^m] = \mathbf{Y}_k\, [\mathbf{f}_0^1\, \mathbf{f}_0^2 \ldots \mathbf{f}_0^m] = \mathbf{Y}_k \mathbf{I} = \mathbf{Y}_k \tag{4.16}$$

where, y_k^i the correlation function for reference signal i, and f_0^i is the input vector that has all elements equal to zero, apart from the i^{th}, which is equal to one.

It needs to be mentioned that when applying NExT, it is important to use data with long time series to improve the accuracy of the correlation function. However, it is important to keep in mind that the first part of the correlation function will already include most of the modal content.

4.3. NUMERICAL RESULTS

In this section, the theory explained in the previous two sections will be applied on simulated data obtained from the OWT Matlab model described in Section 4.3.2. At first, the algorithm of ERA will be applied on the special case of impulse loading to validate the applicability on IRFs. The identified modal parameters can be verified with the known values of Table 3.1. Then, ERA/NExT will be applied and validated on the case where the system is loaded by white noise. Additionally, the influence of several inputs defined by the user in the algorithm (*e.g.* number blocks that will be arrayed in the Hankel matrix) will be investigated. Also, the robustness against harmonic excitation will be checked for the case of combined white noise and harmonic excitation. In the end, the identification on the OWT simulated in Matlab, under wind, wave and current excitation will be attempted. In the Section 3.3, the algorithm will be applied on responses simulated from the NREL offshore 5-MW baseline wind turbine. The main target is to investigate the applicability of the algorithm on different operating regimes as explained in Section 2.2. Table 3.4 and Table 3.5 can be used for the validation of the identified natural frequency and the related damping ratio.

4.3.1. SIMULATED RESPONSES USING MATLAB MODEL

ERA for impulse input

Initially, ERA algorithm is be applied on simulated responses that correspond to the case where all the DoF of the system are excited by impulse loading. More details about this simulated case can be found in Section 3.2.2. In this example, the accelerations at the four selected nodes will be fed into the algorithm after including some random measurement noise. This can be done by using a Signal-to-Noise Ratio (SNR) equal to 50. Also, the sampling frequency is 63.7Hz and the duration of the signal is 10min.

At first, a number of p =400 row blocks and q =1400 column blocks will be used. The time-series of each signal has 39086 discrete samples, which means that the bottom right block of the Hankel matrix $\mathbf{H}(0)$ corresponds to the element $k+p+q-2$=1+400+1400−2=1799 of the time vector. Therefore, only a part of the whole response signal will be used (almost 4.6%). However, by looking into the time-series one may realize that this part contains all the modal content of the response, while in the rest part the response is almost damped out. In addition, using a larger part of the response will result in a very slow identification with minor improvements on the resulting modal properties. Another input to the algorithm is the order of the system n. Instead of selecting a specific number of n, the algorithm will be applied in an iterative way to visualize the influence of the order in the identified modal properties.

As it can be shown in Figure 4.2, the first 4 modes are identified in a stable way, while the fifth mode is relatively shifted from the actual natural frequency. Different scales of black and colors are used for each node as an indicator of the modal damping. More in detail, red denotes damping ratio larger than 75%, green corresponds to damping larger than 50%, and cyan is used for values larger than 25%. Below 25%, scales of black have been used with white used for damping ratio equal to 0%. Apart from the identified modes, Figure 4.2 also displays the output spectrum at the location of the sensors. Node 10 is the location of the RNA, while the rest nodes can be found in Section 3.2.2. Finally, it needs to be mentioned that a MAC factor of 90% is used to filter the non-structural modes and result in a clear stabilization diagram.

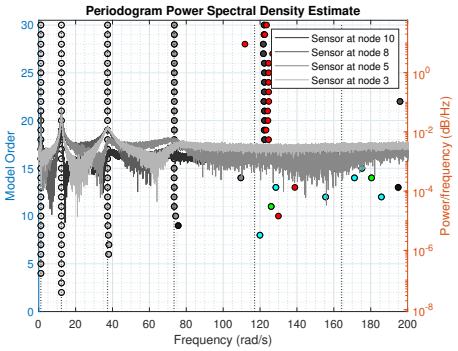

Figure 4.2: Stabilization diagram – ERA on impulse response

The results of the identification are summarized in Table 4.1 together with the natural frequencies and the damping ratio derived analytically.

ERA/NExT for white noise input

The algorithm of ERA will now be applied on the auto/cross correlation functions as proposed by NExT in Section 4.2. Therefore, the correlation function $\mathbf{c}(t) \in \mathbb{R}^{mxm}$ will be used for the identification, instead of the output vector $\mathbf{y}(t) \in \mathbb{R}^{mx1}$. Here, it was implicitly said that a square matrix $\mathbf{c}(t)$ will be employed and not a vector of correlations. This happens since all the responses will be used as reference signals. For instance, the first column will be determined by using the first response signal as reference signal, the second column will correspond to using the second response signal as reference signal, and so on.

The time-series have the same sampling properties as described in the aforementioned case of impulse input. However, the first 100s will be truncated from the response time-series before calculating the correlation functions, in order to remove the transient part and keep only the steady state part of the response. In the same way as before, a MAC factor equal to 90% has been selected, the maximum order of the stabilization diagram will be n =30 and the number of rows and column blocks will be p =400 and q =1400, respectively. Finally, measurement noise is added to corrupt the response time-series with an SNR equal to 50.
As it can be shown, the first three modes were identified using ERA/NExT. Also, the algorithm resulted in an almost stable mode close to the fourth natural frequency. However, the damping ratio related to this mode is too high, and therefore be considered as an acceptable mode. The results of the identification are summarized in Table 4.1 together with the exact values of the modal properties.

Investigate the influence of p and q

When applying ERA, one has to decide the number of blocks $\mathbf{Y}_k$ that will be used to build the block-Hankel matrix of Eq.4.3. In this paragraph, the influence of the way the blocks are arrayed in Hankel matrix will be

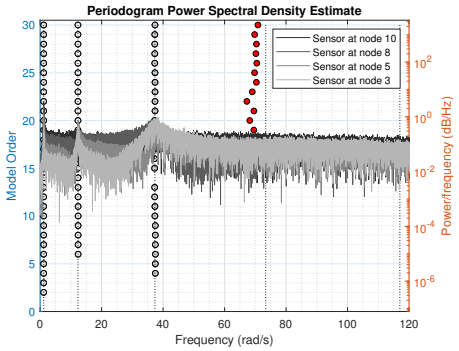

Figure 4.3: Stabilization diagram – `ERA/NExT` for white noise input

Mode	Exact		ERA (impulse)			ERA/NExT (white noise)		
	ω_d (rad/s)	ζ (%)	ω_d (rad/s)	ζ (%)	MAC (%)	ω_d (rad/s)	ζ (%)	MAC (%)
1	1.155	4.00	1.156	4.01	100.00	1.149	2.99	100.0
2	12.303	2.00	12.304	2.00	100.00	12.299	1.94	98.9
3	37.305	5.09	37.316	5.09	99.99	37.363	4.87	97.3
4	73.332	9.83	73.526	10.22	99.95	-	-	-

Table 4.1: Identified and exact modal properties for `ERA` and `ERA/NExT` (for $n_{max} = 30$)

investigated. Measurement noise is deactivated, since the task is to check thoroughly only into the influence of the blocks on the identification. Also, as it is displayed in Figure 4.3, an order equal to 30 is already much larger than the actual order of the system and thus, such an order may be used for the purpose of this investigation.

The strategy that was followed is to obtain the natural frequencies and damping ratios factor for q and p that take values in the range 100−1900 with step 200. In Figure 4.4, the difference between the identified and the exact 1st natural frequency is displayed with respect to the values of p and q.

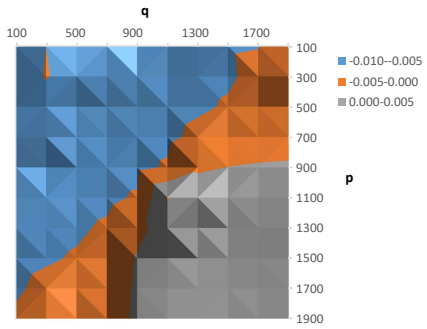

Figure 4.4: Difference of identified with exact fundamental natural frequency with respect to p and q values

It was found out that increasing the total number of both p and q does not strictly mean that the resulting identified modal parameters will get closer to the exact values. Also, all the figures from the rest identified natural frequencies showed similar behaviour to Figure 4.4. More specifically, a region was observed where the difference was minimum. A possible set of p and q close to that region is p =900 and q =1300. Keep in mind that selecting large values of p and q might lead into very large $\mathbf{H}(0)$ and $\mathbf{H}(1)$ matrices, which also leads to slow identification procedure. Therefore, a set of p =400 and q =1400 is a balanced option between accuracy and speed.

Investigate the influence of the reference signals

The selection of one single signal for the calculation of the correlation functions might be tempting as it will lead to faster calculations. Additionally, selecting different reference signals will probably affect the identification. This is the reason why the influence of using a poly-reference version of `ERA/NExT` needs

to be investigated. At first, the number of the row and column blocks has been chosen to be p =400 and q =1400, respectively. Also, measurement noise is deactivated in order to remove any random influence on the results. Based on that settings, all the possible combinations of the four signals were used and the identification was held for a system orders n =30. Considering four output responses, the total number of possible combinations of reference signals is 15. For each combination of reference signals, the related values of the identified natural frequencies and modal damping were obtained. It was found out that the selection of the reference signal affects the identification. Figure 4.5 shows an example for the case of the 2nd identified natural frequency.

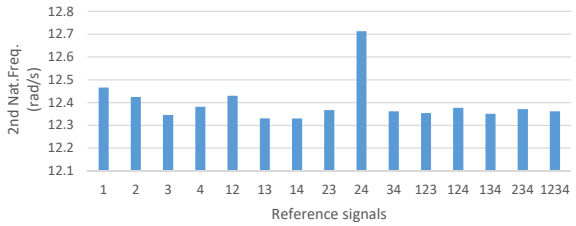

Figure 4.5: Influence of the reference signals on the 2nd identified natural frequency

Particularly, the parameters that were identified using a single reference signal, or couple of reference signals were quite different with respect to each other. This difference was smoothed out when three signals were used, instead. Finally, the option of using all the reference signals resulted in a solution that follows the general tendency observed in all other combinations.

Additionally, the identification was also applied by iterating over the system order until the value of n =30 was reached. It was found out that the option of poly-reference ERA/NExT leaded into more stable identification.

It needs to be mentioned here that no combination of reference signals resulted in an identification, in which all the modal parameters were simultaneously closer to the related exact values.

Investigate the influence of SNR

ERA/NExT was be able to identify the first three modes of the system loaded by white noise for an SNR equal to 50. The value of SNR is defined as the standard deviation of a signal over the standard deviation of noise. Therefore, by reducing this value noise becomes more and more dominant. It was found out that for an SNR=0.1, the natural frequencies were stably identified, but the damping ratio were largely deviating. In addition, even lower SNR would lead into problems in identifying the second and the third natural frequencies. Such values of SNR are very extreme cases of noise, though. Table 4.2 shows the resulting modal properties for several values of SNR. As it can be shown, the even for low values of SNR, the identified modes are not largely affected.

SNR	ω_1 (rad/s)	ζ_1 (%)	ω_2 (rad/s)	ζ_2 (%)	ω_3 (rad/s)	ζ_3 (%)
1	1.149	2.87	12.340	2.19	37.194	6.44
10	1.149	2.97	12.305	1.93	37.309	4.71
50	1.149	2.97	12.301	1.94	37.319	5.03
100	1.149	2.99	12.307	1.90	37.377	4.91
500	1.149	3.00	12.307	1.89	37.335	4.98
1000	1.149	2.99	12.306	1.92	37.370	4.90
Not incl.	1.149	2.99	12.307	1.90	37.377	4.93

Table 4.2: Identified modal properties for varying SNR (for n = 30)

ERA/NExT for white noise and harmonic input

An important parameter that needs to be investigated is the presence of harmonic components in the input. The theory behind ERA/NExT makes the assumption of white noise excitation. It is expected that in case where the loading includes harmonic components, the algorithm will be tricked and will not be able to differentiate between a structural mode and a fake mode that corresponds to the harmonic excitation.

In this section, three identifications were applied on simulated data derived from white noise excitation, combined with an harmonic component at a specific frequency. The first analysis corresponds to an harmonic excitation of 1.31rad/s, the second to 1.45rad/s and the third 1.76rad/s. Also, the amplitude of this harmonic was selected to be as high as needed, so that the response at the excitation frequency would be similar to the response at the resonance frequency. The target is to add an harmonic component close to the first natural frequency of the system and see whether the identified mode is affected. Figure 4.6 shows the stabilization diagrams for the three cases.

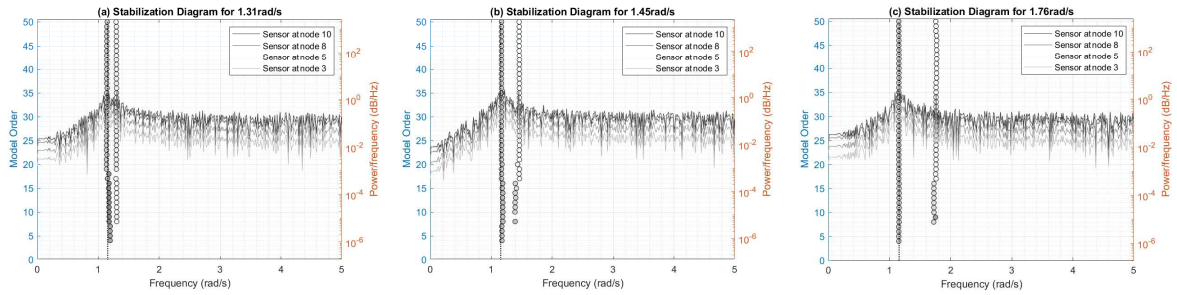

Figure 4.6: Stabilization diagram, zoomed at the fundamental natural frequency for three different harmonic components

As it can be shown, the harmonic is identified as a mode with almost zero damping (almost white marker). That makes sense, since the response at that given frequency is too high with respect to the neighbouring frequencies and an almost infinite response corresponds to a mode with zero damping.

Another point to mention is that the identified first mode was slightly affected for low system orders (close to n =20), but for larger orders the mode was nicely identified. This showed a robustness of ERA/NExT against the case where an harmonic component is close to a structural mode.

ERA/NExT for wind, wave and current excitation

The OWT model in Matlab was developed to derive responses data which is simulated using more realistic load conditions. Here, an attempt will be made to identify the system loaded by non-white noise input. More in detail, the model in Matlab is excited by hydrodynamic loads due to wave and current and also by wind forces at the top of the OWT. Hence, the hydrodynamic loading cannot be considered as a broadband white noise excitation. The same inputs to ERA/NExT algorithm as in the identification for white noise excitation were also used here. The only difference is that the stabilization diagram was generated for a maximum order of 50, instead of 30. By looking into the resulting stabilization diagram of Figure 4.7, one may see that the first three modes were nicely identified.

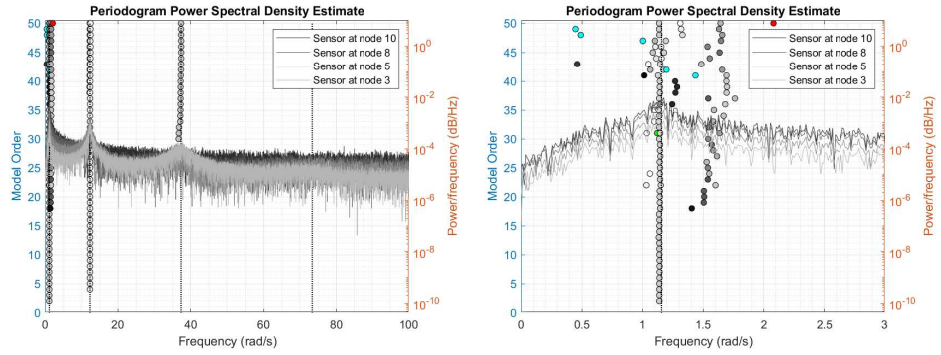

Figure 4.7: Stabilization diagram – ERA/NExT for wind, wave and current excitation over full frequency range (left) and zoomed in first natural frequency (right)

Given that the biggest part of the wave energy is concentrated at frequencies close to ~0.5rad/s, it can be deduced from the response spectra that the simulated OWT in Matlab is mainly dominated by wind loading, as the wave loads do not result in significant amplification. For a short range of system order, between 40~45,

Mode	Exact		ERA/NExT (env.cond.)		
	ω_d (rad/s)	ζ (%)	ω_d (rad/s)	ζ (%)	MAC (%)
1	1.155	4.00	1.145	3.91	99.95
2	12.303	2.00	12.288	1.67	99.70
3	37.305	5.09	37.278	5.67	93.86

Table 4.3: Identified and exact modal properties – ERA/NExT for wind, wave and current excitation (for $n_{max} = 30$)

the first mode got unstable, but it cannot be attributed to the presence of wave. The identified modes can be shown in Table 4.3, together with the related exact values.
As it can be shown, the first identified mode has a natural frequency quite smaller than the exact value. However, this deviation is similar to the difference observed for the case of white noise excitation. In other words, there is no clear shifting of the identified natural frequency due the presence of wave loading.

4.3.2. SIMULATED RESPONSES USING MODEL IN FAST

In this section ERA/NExT algorithm will be applied on responses obtained from the model in FAST, where at the same time both the white noise loading and the LTI assumptions are violated. The load cases that will be examined are summarized in Table 2.2.

Four acceleration time-series have been used for the identification based on the sensors located as shown in Figure 3.20 in Section 3.3.2. Node 4 corresponds to the sensor located at the highest point amongst the other accelerometers. The time vector that corresponds to the response time-series consists of 38199 data points and has a duration of 10min. Keep in mind that the first 200s were already truncated from the initial 800s time-series by FAST to remove any transients related to the initial conditions. Additionally, the responses have been corrupted by adding measurement noise of SNR equal to 50.

Regarding the input variables to ERA/NExT, the value of row and column blocks have been selected to be p =400 and q =1400, respectively. Moreover, for each case, a stabilization diagram up until an order of 80 was constructed. Finally, the MAC factor was selected to be 80%, which is quite small in order to allow more modes to be present in the stabilization diagram, even if they are non-structural modes. In the subsequent parts the results for the load cases presented in Table 2.2 will be presented.

Case FC1

The first load case examined here is FC1, which corresponds to low wind speeds and low wind and rotor speed. In that case, the harmonic content at 3P gets closer to the first fore-aft tower bending mode. However, as it can be shown in Figure 4.8, the first tower mode could be identified in a stable way. Another observation is that all the external harmonic excitations 3P and 6P were identified as modes, which can cause problems in identifying the blade modes around that region. Besides that, two blade modes (B2-F1 and B3-E1) were identified in an unstable way around the 6P region. The related damping was much smaller for all the flapwise bending modes. Then, close to the region dominated by the second flapwise bending modes, the algorithm resulted in two lines of identified modes, which may refer to B2-F2 and B3-F2. Still, one may observe that the values of damping are much smaller than the values from the linearisation procedure. In the end, the second tower mode was identified in a stable way and both damping and natural frequencies were very close to the exact values.

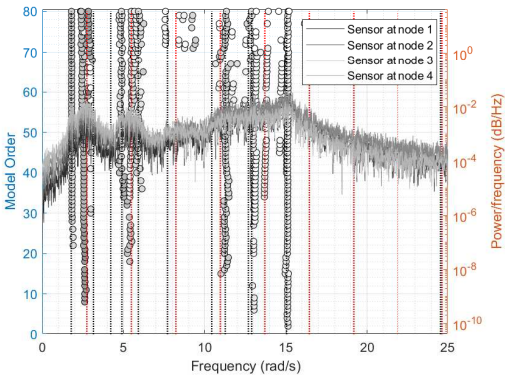

Figure 4.8: ERA - Stabilization diagram for FC1

Mode	Exact (8.5rpm)		ERA/NExT (FC1)		
	ω_d (rad/s)	ζ (%)	ω_d (rad/s)	ζ (%)	MAC (%)
T-FA1	1.78	6.15	1.79	4.84	99.2
B2-F1	4.90	32.85	4.87	2.97	97.7
B3-E1	5.91	1.10	5.92	3.44	95.1
B2-E1	7.71	0.85	7.59	0.61	80.7
B2-F2	11.26	10.80	11.34	3.34	94.0
B3-F2	12.90	9.05	12.88	3.17	91.7
T-FA2	15.04	2.85	15.14	2.30	98.3

Table 4.4: ERA - Identified modal properties for FC1

Case FC2

In FC2, the 3P and 6P harmonic components of the excitation start moving away from the first tower mode, since the rotor rotational speed increases. Similar to the loading case FC1, both tower modes were identified with an acceptable difference from the exact values, while the damping from the flapwise bending modes deviate largely from the related exact values. One may observe that all the identified blade modes are not stable, and in many cases the MAC factor drops below the threshold of 80%.

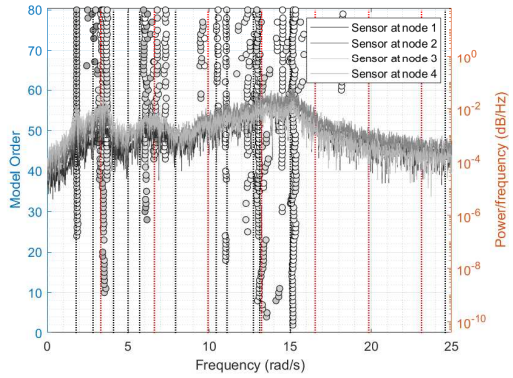

Figure 4.9: ERA - Stabilization diagram for FC2

Mode	Exact (10.5rpm)		ERA/NExT (FC2)		
	ω_d (rad/s)	ζ (%)	ω_d (rad/s)	ζ (%)	MAC (%)
T-FA1	1.79	7.30	1.82	5.05	98.9
B3-E1	5.71	1.20	5.95	6.67	95.1
B1-E1	10.44	2.20	10.54	0.47	91.1
B2-F2	11.11	13.60	11.08	1.40	83.6
B1-F2	12.73	11.50	12.38	2.11	95.8
B3-F2	13.12	10.45	12.94	2.84	98.9
T-FA2	15.02	3.45	15.19	1.41	98.0

Table 4.5: ERA - Identified modal properties for FC2

Case FC3

In the third case, the first tower mode was identified, but the difference of the related damping seems to be larger than in the previous examined cases. Also, the second tower mode was identified, even though many non-structural modes are in parallel present around it. The first flapwise bending modes are highly affected by the presence of 3P loading, and no stable mode was found. Same happened for the edgewise modes, which are affected by 6P loading. Finally, in larger frequencies, where the influence of nP has significantly decayed, two blade modes were identified, but with poor damping estimation.

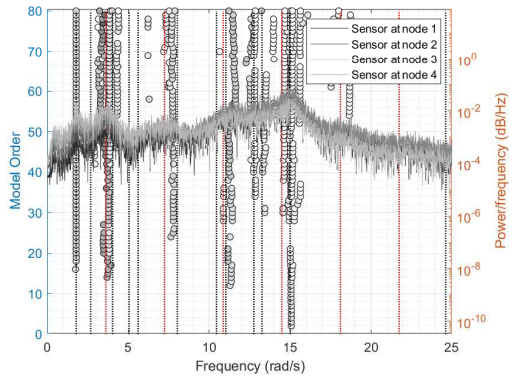

Figure 4.10: ERA - Stabilization diagram for FC3

Mode	Exact (11.5rpm)		ERA/NExT (FC3)		
	ω_d (rad/s)	ζ (%)	ω_d (rad/s)	ζ (%)	MAC (%)
T-FA1	1.79	7.75	1.79	2.91	99.4
B2-F2	11.03	14.70	11.22	5.40	92.2
B3-F2	13.26	10.85	13.23	6.21	89.4
T-FA2	15.00	3.75	15.04	1.56	99.8

Table 4.6: ERA - Identified modal properties for FC3

Case FC4

This is the fourth and last case where the turbine is considered to be under operating conditions. Here, the turbine does not shift between different operating regimes, and therefore, the rotational speed of the rotor is varying only slightly around a constant rotational speed. In that case, one can see that the 3P, 6P and 9P loading were all identified as structural modes. Apart from that, one edgewise and one flapwise mode were identified. This is the first case where the first tower mode is identified in a very high accuracy. This may be attributed to the fact that it coincides with the first flapwise blade bending mode.

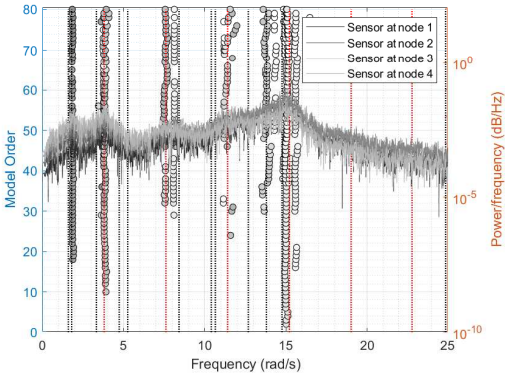

Figure 4.11: ERA - Stabilization diagram for FC4

Mode	Exact (12.1rpm)		ERA/NExT (FC4)		
	ω_d (rad/s)	ζ (%)	ω_d (rad/s)	ζ (%)	MAC (%)
T-FA1	1.80	10.20	1.84	11.04	95.0
B3-F1	1.60	90.83			
B2-E1	8.42	0.90	8.13	1.06	94.8
B3-F2	13.80	15.36	13.60	5.02	93.5
T-FA2	14.76	4.34	15.06	2.25	98.0

Table 4.7: ERA - Identified modal properties for FC4

Case FC5

In the end, the case of a parked turbine is examined. In FC5 no harmonic component excites the system. This results in much more stable identification and also in the largest number of identified modes amongst the other cases. It needs to be highlighted here that the damping of the blades is still much different than the real values only for the three flapwise bending modes (B3-F1, B2-F1 and B1-F1), which are almost coincident. The rest five blade modes have relatively small deviations from the actual damping ratios.

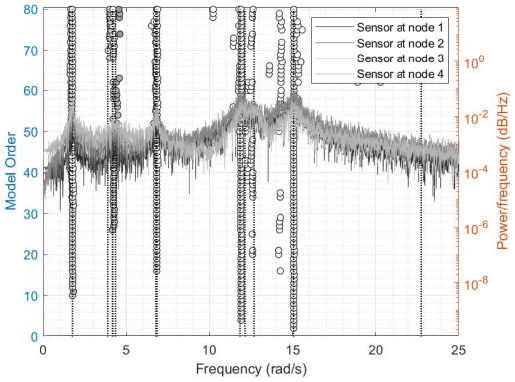

Figure 4.12: ERA - Stabilization diagram for FC5

Mode	Exact (0rpm)		ERA/NExT (FC5)		
	ω_d (rad/s)	ζ (%)	ω_d (rad/s)	ζ (%)	MAC (%)
T-FA1	1.76	0.28	1.75	2.54	99.8
B3-F1	4.19	0.67	4.01	4.04	96.4
B2-F1	4.35	0.69	4.20	0.25	92.4
B1-F1	4.16	0.66	4.56	9.91	86.9
B2-E1	6.85	1.09	6.83	1.37	99.2
B3-E1	6.78	1.08	6.88	0.69	94.2
B2-F2	11.84	1.88	11.90	2.17	98.9
B1-F2	12.68	2.02	12.62	1.07	81.4
T-FA2	15.05	2.40	15.07	1.60	99.4

Table 4.8: ERA - Identified modal properties for FC5

4.4. CONCLUSIONS

In short, ERA/NExT was applied on the simulated results from the OWT model in Matlab for white noise excitation and resulted in a stable identification with modal properties close to the actual properties. The largest difference was between the actual and the identified damping ration related to the fundamental natural frequency (1% lower). Apart from that a discussion about several input parameters was held and in the end the algorithm was checked against SNR and harmonic excitation (not extreme amplitude). It was found out that ERA/NExT is quite robust.

Regarding the application using data from FAST, it was found out that ERA/NExT was able to identify the tower modes in a stable way even for the cases where the turbine is operating. In addition, the damping ratios related to the T-FA1 tower mode in FC3 was highly underestimated. However, the main attention was attracted by the inability of the algorithm to capture the extremely high ($\gg$10%) damping ratios of all the flapwise blade modes of the cases where the rotor was rotating.

The estimation of large damping ratios using ERA is possible, but when the natural frequency is also high, then such a mode is damped out very fast, showing a very small number of cycles in the impulse response. Therefore, in such cases, ERA would deal serious problems in obtaining a stable mode with high precision. However, in the present case ERA did identify modes but failed in obtaining the related damping ratio. One possible explanation could be that the impulse response is probably affected by the presence of the closely spaced nP external excitation, which will show more cycles in the free decay, and will be related to lower damping ratios.

As for the stability of the identification, the stable blade modes in FC5 indicate that the unstable blade modes of the rest cases are directly linked to the rotation of the rotor. This observation has two folds, since the modes could be either affected by the harmonic excitation or by the fact that they change with the rotational speed, which is not constant. Besides this, several modes were present in the stabilization diagrams.

5

STOCHASTIC SUBSPACE IDENTIFICATION

Stochastic Subspace Identification (SSI) is a widely used and powerful time-domain system identification method, with multiple applications on real structures under operating conditions. The basics features behind the mathematically complex algorithm of this technique will be presented in the next paragraphs. In the end of this chapter, the algorithm will be tested on simulated responses from the model in Matlab, and also on measurements from the OWT in FAST, under multiple operating conditions.

5.1. THEORY BEHIND SSI

In this chapter, Stochastic Subspace Identification (SSI) technique will be presented, aiming at making the main features behind the algorithm clear to the reader. It is an undoubted fact that SSI is the most popular time-domain OMA system identification technique. This can be explained by the robustness and the good numerical conditioning of the algorithm for OMA applications. The real break-through of SSI happened when the pioneering work of P. Van Overschee et al. [8] was publishing back in 1996. Since then, SSI has been effectively applied widely on various types of real and simulated structures under operational conditions [49][50][51][52]. Unfortunately, due to its mathematical complexity, most of engineers with classical structural background have difficulties in understand the basic concepts behind SSI. Hence, in the present chapter, an attempt will also be made to relate the steps of SSI with several steps of ERA, described in Chapter 5. It needs to be noted that SSI will be presented in a more user-friendly way. A more detailed, in-depth description of the theory behind SSI can be found in the book of Van Overschee[8], which is also accompanied by already existing, detailed and user-friendly Matlab files.

Before explaining SSI method, it needs to be clarified that several different approaches are available in literature, which might be confusing for the reader. SSI techniques can be classified into Covariance-Driven Stochastic Subspace Identification (Cov-SSI) and Data-Driven Stochastic Subspace Identification (DD-SSI). The approaches described by of Van Overschee[8][9] can be treated as the first DD-SSI method. Both types of algorithms have several pros and cons. In this chapter, DD-SSI method will be presented even though it is not as fast as Cov-SSI due to the use of QR factorization. The main idea behind DD-SSI, as it will be explained later on, is to project the row space of "future" into "past". Due to that, the algorithm may also be referred to as projection-driven SSI method. Many variants of DD-SSI can be found in literature. Three major methods according to the weighting matrices that are applied on Hankel matrix exist[53][50], which are namely the Principal Component (PC) method, the Canonical Variant Analysis (CVA) method and the Unweighted Principal Component (UPC) method. Here, no weighting will be used, since the identified properties are not largely affected by it.

To start with, the aim of SSI is to identify the modal parameters of a vibrating structure, which is considered to be excited by unknown stochastic forces. The algorithm is based on the assumption that this external excitation can be simplified as a zero-mean, Gaussian white noise process. Based on this assumption, SSI is applied directly on measured stochastic response of the system of interest. Therefore, the discrete-time state-space formulation of an LTI vibrating structure described by Eq.4.1 may also be employed for this technique, after making some minor modifications. At first, modelling and sensor uncertainties will be included in the state-space equation of motion by means of two unmeasurable vectors that are assumed to be zero-mean, Gaussian white noise processes. Considering these two vectors, Eq.4.1 will be changed into the expression of

Eq.5.1.

$$\begin{cases} \mathbf{x}_{k+1} = \mathbf{A}\mathbf{x}_k + \mathbf{B}\mathbf{f}_k + \mathbf{w}_k \\ \mathbf{y}_k = \mathbf{C}\mathbf{x}_k + \mathbf{D}\mathbf{f}_k + \mathbf{v}_k \end{cases} \tag{5.1}$$

where, $\mathbf{w}_k \in \mathbb{R}^{nx1}$ is the process noise and $\mathbf{v}_k \in \mathbb{R}^{mx1}$ is the measurement noise. The description and the dimensions of the rest matrices can be found together with Eq.4.1. A more compact way to describe the dynamics of the system under unknown stochastic input, considering the presence of process and measurement noise, is possible by combining the unknown input with the unknown noise. The final expression of the state-space equation, which reflects the state of the dynamic system under consideration, is given in Eq.5.2.

$$\begin{cases} \mathbf{x}_{k+1} = \mathbf{A}\mathbf{x}_k + \mathbf{w}_k \\ \mathbf{y}_k = \mathbf{C}\mathbf{x}_k + \mathbf{v}_k \end{cases} \tag{5.2}$$

where, $\mathbf{w}_k$ is now an excitation vector including both process noise and the impact of the input on the state vector and $\mathbf{v}_k$ expresses the direct transition of the input to the output, including measurement noise. The statistical properties of these vectors remain the same, since both the input and noise is assumed to be a Gaussian white noise process. This is the final form of the discrete state-space equation that will be used in `SSI`. Next, the procedure of the `SSI` method will be explained in a step-by-step manner. It needs to be mentioned beforehand that this algorithm uses robust numerical techniques (*e.g.* `QR`-factorization, `SVD` and least squares) from linear algebra. Extended explanation of these techniques are out of this thesis scope.

Step 1 - Hankel Matrix

The algorithm starts by constructing the block-Hankel matrix. This matrix can be formed by arranging the measured response vector at time k into blocks $\mathbf{Y}_k \in \mathbb{R}^{mx1}$, where m is the number of measurement stations. The block-Hankel matrix will be created by using $2i$ rows and j columns of blocks $\mathbf{Y}_k$ (q and p in `ERA`, respectively). Eq.5.3 shows the expression of the whole block-Hankel matrix $\mathbf{H}_{0|2i-1} \in \mathbb{R}^{2mixj}$.

$$\mathbf{H}_{0|2i-1} = \frac{1}{\sqrt{j}} \left[\begin{array}{ccccc} \mathbf{Y}_0 & \mathbf{Y}_1 & \mathbf{Y}_2 & \dots & \mathbf{Y}_{j-1} \\ \mathbf{Y}_1 & \mathbf{Y}_2 & \mathbf{Y}_3 & \dots & \mathbf{Y}_j \\ \vdots & \vdots & \vdots & \ddots & \vdots \\ \mathbf{Y}_{i-1} & \mathbf{Y}_i & \mathbf{Y}_{i+1} & \dots & \mathbf{Y}_{i+j-2} \\ \hline \mathbf{Y}_i & \mathbf{Y}_{i+1} & \mathbf{Y}_{i+2} & \dots & \mathbf{Y}_{1+j-1} \\ \mathbf{Y}_{i+1} & \mathbf{Y}_{i+2} & \mathbf{Y}_{i+3} & \dots & \mathbf{Y}_{1+j} \\ \vdots & \vdots & \vdots & \ddots & \vdots \\ \mathbf{Y}_{2i-1} & \mathbf{Y}_{2i} & \mathbf{Y}_{2i+1} & \dots & \mathbf{Y}_{2i+j-2} \end{array}\right] = \left[\frac{\mathbf{H}_{0|i-1}}{\mathbf{H}_{i|2i-1}}\right] = \left[\frac{\mathbf{H}_p}{\mathbf{H}_f}\right] \tag{5.3}$$

where, $\sqrt{j}$ is a scale factor used for statistical reasons. Additionally, in this expression one may notice that the matrix is divided into two parts. The top matrix $\mathbf{H}_{0|i-1} \in \mathbb{R}^{mixj}$ includes the first i block rows and is named shortly as $\mathbf{H}_p$, while the bottom matrix $\mathbf{H}_{i|2i-1} \in \mathbb{R}^{mixj}$ includes the rest i block rows of $\mathbf{H}_{0|2i-1}$ and is denoted by $\mathbf{H}_f$. Each new block row can be interpreted as a time shift. To underline this, the subscripts p and f of these two sub-matrices have been used to represent "past" and "future", respectively. Given that, the maximum number of block columns is $n_t + 2 - 2i$, where n_t is the total number of time samples.

Step 2 - Projection of "future" onto "past" row space

Once the two matrices have been formed, a projection (or subspace) matrix $\mathbf{O}_i \in \mathbb{R}^{mixj}$ will be defined as the orthogonal projection of the row space of future outputs $\mathbf{H}_f$ on the row space of past outputs $\mathbf{H}_p$. This step is the reason why this technique is named as subspace identification method. This matrix $\mathbf{O}_i$ can be computed as shown in Eq.5.4 from these two row space matrices.

$$\mathbf{O}_i = E\left(\mathbf{H}_f | \mathbf{H}_p\right) = \mathbf{H}_f \mathbf{H}_p^T \left(\mathbf{H}_p \mathbf{H}_p^T\right)^+ \mathbf{H}_p \tag{5.4}$$

where $(\bullet)^+$ denotes the Moore-Penrose pseudo-inverse of a matrix. This definition holds for semi-infinite matrices. Therefore, the number of column blocks need to be quite large ($j \to \infty$). In practice instead of using the above formula, an alternative expression of the projection matrix $\mathbf{O}_i$ is adopted. The main reason

is to avoid inverting matrix $\mathbf{H}_p\mathbf{H}_p^T$, as $\mathbf{H}_p$ is usually very large matrix. This alternative derivation is based on QR-decomposition of the whole block-Hankel matrix $\mathbf{H}_{0|2i-1}$ as shown in Eq.5.5.

$$\mathbf{H}_{0|2i-1} = \mathbf{R}\mathbf{Q}^T = \begin{bmatrix} \mathbf{R}_{11} & 0 \\ \mathbf{R}_{21} & \mathbf{R}_{22} \end{bmatrix} \begin{bmatrix} \mathbf{Q}_1^T \\ \mathbf{Q}_2^T \end{bmatrix} \tag{5.5}$$

In this expression, $\mathbf{R} \in \mathbb{R}^{2mix2mi}$ is a lower triangular matrix and $\mathbf{Q} \in \mathbb{R}^{jx2mi}$ is an orthogonal matrix. These two matrices are divided into the submatrices $\mathbf{Q}_1/\mathbf{Q}_2 \in \mathbb{R}^{jxmi}$ and $\mathbf{R}_{11}/\mathbf{R}_{21}/\mathbf{R}_{22} \in \mathbb{R}^{mixmi}$, respectively. Then the projection matrix $\mathbf{O}_i$ can be calculated using two submatrices, as described in Eq.5.6.

$$\mathbf{O}_i = E\left(\mathbf{H}_f|\mathbf{H}_p\right) = \mathbf{R}_{21}\mathbf{Q}_1^T \tag{5.6}$$

It needs to be noticed that the projection matrix $\mathbf{O}_i$ has dimensions $mixj$, while the block-Hankel matrix $\mathbf{H}_{0|2i-1}$ is $2mixj$. Therefore, this step results in a significant reduction of the data that will be used in the identification. The concept of matrix projection is considered to be the most complex part of SSI method in terms physical understanding. Looking into the matrices of the projection, matrix $\mathbf{H}_f\mathbf{H}_p^T$ can be interpreted as a correlation matrix. In that sense, the projection matrix is related to covariances and therefore, it leads into responses that represent impulse responses of the system, as described by NExT. Mathematically, this projection is also named as conditional expectation or conditional mean of $\mathbf{H}_f$ on $\mathbf{H}_p$. Finally, a more geometrical interpretation of the projection is given by Van Overschee. According to this, the projection aims at finding the principal components of the two row spaces, which are related to the main harmonics that are present in the signal. In that way, the random effect of noise is removed, while the harmonic components match and reveal the presence of a specific mode.

Step 3 – Observability Matrix & Kalman States

Next, based on the main theorem of SSI, the projection matrix $\mathbf{O}_i$ can be factorized into the product of the observability matrix $\mathbf{P}_i$ and a matrix $\hat{\boldsymbol{X}}_i$. This matrix includes a series of vectors, which is the Kalman filter state sequence. This factorization of matrix $\mathbf{O}_i$, together with the expression of the observability matrix are shown in Eq.5.7.

$$\mathbf{O}_i = \mathbf{P}_i\hat{\boldsymbol{X}}_i = \begin{bmatrix} \boldsymbol{C} \\ \boldsymbol{CA} \\ \boldsymbol{CA}^2 \\ \vdots \\ \boldsymbol{CA}^{i-1} \end{bmatrix} \begin{bmatrix} \hat{\boldsymbol{x}}_i & \hat{\boldsymbol{x}}_{i+1} & \dots & \hat{\boldsymbol{x}}_{i+j-1} \end{bmatrix} \tag{5.7}$$

where $\mathbf{P}_i \in \mathbb{R}^{mixn}$, $\hat{\boldsymbol{X}}_i \in \mathbb{R}^{nxj}$, and n is the order of the system. The above expression shows that the observability matrix is formed using Markov parameters. Each column of $\mathbf{P}_i$ can be also interpreted as a free decay of the system under unknown initial conditions. This equation is the first indicator that the system state-space matrices can be derived from the measurement data. Unfortunately, since only $\mathbf{O}_i$ is known amongst the three matrices, the observability matrix cannot be directly calculated.

Step 4 – Singular Value Decomposition

In this step, the projection matrix $\mathbf{O}_i$ will be decomposed by a SVD process. This is a trick that aims at estimating the observability matrix and the Kalman states mentioned in the previous step (see Eq.5.8). It is obvious that matrix $\mathbf{O}_i$ will be initially of full rank and, therefore, the number of singular values will be equal to the minimum dimension of $\mathbf{O}_i$.

$$\mathbf{O}_i = \mathbf{U}\mathbf{S}\mathbf{V}^T = \begin{pmatrix} \mathbf{U}_1 & \mathbf{U}_2 \end{pmatrix} \begin{pmatrix} \mathbf{S}_1 & 0 \\ 0 & \mathbf{S}_2 \approx 0 \end{pmatrix} \begin{pmatrix} \mathbf{V}_1^T \\ \mathbf{V}_2^T \end{pmatrix} \approx \mathbf{U}_1\mathbf{S}_1\mathbf{V}_1^T \tag{5.8}$$

where $\mathbf{U} \in \mathbb{R}^{mixmi}$ and $\mathbf{V} \in \mathbb{R}^{jxmi}$ are the left and right singular vectors and $\mathbf{S} \in \mathbb{R}^{mixmi}$ is a diagonal matrix containing singular values in descending order. As it is shown in Eq.5.8, the number of the singular values can be reduced after truncating part of the small singular values. The remaining singular values are gathered in $\mathbf{S}_1 \in \mathbb{R}^{nxn}$, where n is the order of the system and also the rank of the observability matrix (it is assumed that $n \leq mi$). This truncation leads in the reduced matrices $\mathbf{U}_1 \in \mathbb{R}^{mixn}$, $\mathbf{V}_1 \in \mathbb{R}^{jxn}$ and $\mathbf{S}_1 \in \mathbb{R}^{nxn}$. It needs to be mentioned that the true order of the system remains still unknown. In practice, this problem is avoided

by applying SSI in an iterative way for several orders in order to build a stabilization diagrams. Moreover, the truncation of the lowest part of singular values does not affect the identification, since it removes only singular values that are related to noise.

Based on the approximation of the projection matrix $\mathbf{O}_i$,the following expressions can be used for $\mathbf{P}_i$ and $\hat{\boldsymbol{X}}_i$.

$$\begin{aligned} \mathbf{P}_i &= \mathbf{U}_1 \mathbf{S}_1^{1/2} \\ \hat{\boldsymbol{X}}_i &= \mathbf{S}_1^{1/2} \mathbf{V}_1^T \end{aligned} \tag{5.9}$$

The above estimated matrices are not unique. Any different way to express them will affect the individual matrices, but not the estimated modal parameters of the system.

Step 5 – System matrices & Eigenvalue problem

In the fifth step, the desired system matrices will be calculated from the observability matrix. There are several ways that can be utilized to obtain **A** and **C** matrices. Here, the derivation will be explicitly based on matrix $\mathbf{P}_i$. At first, state matrix **A** can be calculated in a least squares sense by using $\underline{\mathbf{P}}_i$ and $\bar{\boldsymbol{P}}_i$, which are the first $i-1$ and last $i-1$ blocks of observability matrix, respectively. The derivation can be shown in Eq.5.10.

$$\begin{bmatrix} \boldsymbol{C} \\ \boldsymbol{CA} \\ \vdots \\ \boldsymbol{CA}^{i-2} \end{bmatrix} \mathbf{A} = \begin{bmatrix} \boldsymbol{CA} \\ \boldsymbol{CA}^{2} \\ \vdots \\ \boldsymbol{CA}^{i-1} \end{bmatrix} \rightarrow \underline{\mathbf{P}}_i \mathbf{A} = \bar{\boldsymbol{P}}_i \rightarrow \mathbf{A} = \underline{\mathbf{P}}_i^{+} \bar{\boldsymbol{P}}_i \tag{5.10}$$

Then, the output matrix **C** can be determined in a very straightforward way, as it is equal to the first block (m rows) of the $\mathbf{P}_i$.

Once the discrete system matrices have been identified, then the modal parameters can be calculated following the same procedure described in Step 5 of ERA algorithm. In short, eigenvalues and eigenvectors can be calculated by solving the eigenvalue problem, while also consulting Eq.4.9 & Eq.4.10. Using the eigenvalues, the natural damped frequencies and the related damping ratio can be obtained from Eq.4.11 and Eq.4.12, respectively. Finally the mode shapes are calculated by Eq.4.13.

Other SSI-related algorithms found in literature

The approach SSI that was described here is one of the most commonly found in many applications. However, one may find multiple alternatives of the way SSI is applied. One alternative is presented by P. Van Overschee et al. back in 1993 [9]. The algorithm is nicely presented in a step-by-step manner at the related paper. In short, this approach applies twice a generalized SVD on parts of the **R** matrix. This matrix has been divided into parts in a way that can be related to the shift in ERA (using $\mathbf{H}(0)$ and $\mathbf{H}(1)$) or to the shift of the observability matrix of Eq.5.10.

Apart from the classical SSI method, several authors have proposed techniques to modify SSI in order to be able and identify modes in cases where the input includes also harmonic components[54][24]. However, such modification is not able to remove the influence of the nP input from FAST, since the excitation extends over a wider region.

5.2. NUMERICAL RESULTS

In the previous Section 5.1, the steps of the algorithm behind SSI were discussed. This algorithm will be referred to in this section as SSI-a. Apart from that algorithm, the proposed approach of P. Van Overschee et al. [9] will also be used. This will be named here as SSI-b. The last algorithm that will be applied on the data is the already existing algorithm that accompanies the book of P. Van Overschee et al. [8]. The acronym SSI-Ov will be used for this third algorithm. All these three SSI algorithms will be used in the present section on measurements derived from both the OWT model Matlab and in FAST for the purpose of the benchmark study. To summarize, the SSI algorithms that will be used in this section are:

- SSI-a: Algorithm explained in Section 5.1
- SSI-b: Algorithm from paper [9]
- SSI-Ov: Existing algorithm from P. Van Overschee [8]

5.2.1. SIMULATED RESPONSES USING MATLAB MODEL

SSI for white noise input

The algorithm of SSI is in general applied on cases where the input to the system is a white noise process. Here, given that this condition is met, the three employed algorithms will be compared to each other. Before using the response signals for the identification, the first 100s of the time-series are truncated and the rest is corrupted using an SNR equal to 50. It was found out that most of the non-structural modes that were identified by SSI are highly affected by the randomness of the measurement noise. In other words, running the same analysis twice will result in spurious modes that are different. An explanation could be that these modes are present due to exceeding the actual order of the structure. Therefore, several relatively low singular values will be included and not truncated. These singular values are probably affected by the additional noise and minor variations would lead into jumps in the identified non-structural modes. On the other hand, a stable mode is probably related to the largest singular values, which are not influenced by noise. This observation was exploited in order to filter out these modes by running the identification twice and by matching the stable modes from the two stabilization diagrams. This would slow down the identification, but in parallel will result in a clear stabilization diagram.

Regarding the input parameters to SSI algorithms, a total number of i =100 row blocks have been selected due to the fact that, according to the theory of SSI, the number of column blocks j should be infinite. Given that the total number of data is 32720, this leads into $j = n_t+2-2i$ =32522. Finally, as it can be shown in Figure 5.1, the maximum system order was selected to be 30.

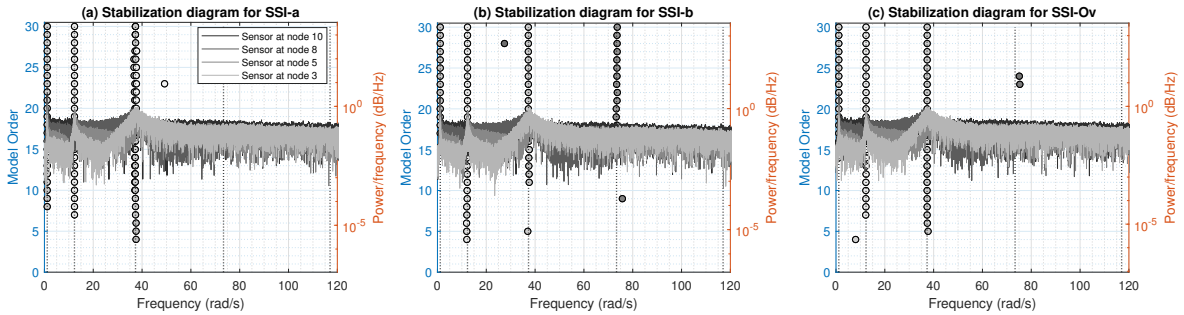

Figure 5.1: Stabilization diagram - SSI for white noise input

By looking into these stabilization diagrams one may observe that SSI-b resulted into the identification of four modes, while SSI-a was able to identify only the first three modes. Additionally, it seems that SSI-Ov also identified the fourth mode, but only for a couple of orders. For the rest orders the fourth mode was filtered out due to excessive instability (>1rad/s). Table 5.1 shows a summary of the identified modes together with the exact values. As it can be shown, the identified modes for an order n =30 are very close to the actual modal properties of the system.

Mode	Exact		SSI-a		SSI-b		SSI-Ov	
	ω_d (rad/s)	ζ (%)	ω_d (rad/s)	ζ (%)	ω_d (rad/s)	ζ (%)	ω_d (rad/s)	ζ (%)
1	1.155	4.00	1.149	4.15	1.142	5.25	1.150	4.10
2	12.303	2.00	12.322	1.88	12.309	1.89	12.314	1.88
3	37.305	5.09	37.322	4.68	37.233	4.96	37.354	5.07
4	73.332	9.83	-	-	73.644	10.55	75.316	12.96

Table 5.1: Identified and exact modal properties for SSI-a, SSI-b and SSI-Ov (for n_{max} = 30)

Investigate the influence of number of block rows i

As explained in the theory of SSI, the algorithm starts by forming a semi-infinite block-Hankel matrix. In this matrix the number of the column blocks j is supposed to tend asymptotically to infinity. Therefore, once the number of row blocks are defined, then the number of blocks j is automatically determined after filling

all the data in the Hankel matrix. Here, several options of the number of rows i will be investigated. Table 5.2 shows that for i =50 the first mode was not accurately identified in all the SSI algorithms. For larger values, it was found out that the differences in the identified modal were not significantly different to each other and also there was no clear tendency towards the real values.

i	SSI-a			SSI-b			SSI-Ov		
	ω_1 (rad/s)	ω_2 (rad/s)	ω_3 (rad/s)	ω_1 (rad/s)	ω_2 (rad/s)	ω_3 (rad/s)	ω_1 (rad/s)	ω_2 (rad/s)	ω_3 (rad/s)
50	1.178	12.311	37.471	-	12.314	37.284	1.012	12.319	37.306
100	1.153	12.316	37.508	1.156	12.312	37.271	1.153	12.315	37.407
200	1.154	12.318	37.188	1.155	12.303	37.298	1.153	12.318	37.481
300	1.155	12.320	37.197	1.153	12.307	37.314	1.154	12.315	37.398
400	1.156	12.319	37.219	1.153	12.304	37.292	1.153	12.315	37.377

Table 5.2: First three identified modes using SSI-a, SSI-b and SSI-Ov for varying row number i (n_{max} = 30)

In SSI-a and SSI-b algorithms, exceeding the value of i =400 resulted in too slow identification process due to the computational demanding calculation of the projection matrix $\mathbf{O}_i$. Therefore, a value of i =100 seems to result in both fast and and accurate enough identification.

Investigate the influence of SNR

SSI is popular for its resistance against noise and its numerical stability. In this paragraph, the influence of SNR will be investigated. Table 5.3 shows the resulting identified modal properties using SSI-a for multiple values of SNR and a given order n =30. As it can be shown, there is no big difference between the results for an SNR equal to 50 and 1000. Therefore, inside that physically meaningful range of noise, it can be concluded that the presence of measurement noise does not affect the identification. For values lower than 0.1, it was found out that the modal parameters were in general influenced by the dominant presence of measurement noise.

SNR	SSI-a					
	ω_1 (rad/s)	ζ_1 (%)	ω_2 (rad/s)	ζ_2 (%)	ω_3 (rad/s)	ζ_3 (%)
0.1	1.128	9.01	12.427	2.49	37.573	4.30
1	1.142	4.39	12.322	1.83	37.107	4.73
10	1.149	5.74	12.319	1.88	37.263	5.45
50	1.153	4.09	12.319	1.86	37.165	5.00
100	1.145	4.49	12.319	1.86	37.180	4.83
500	1.143	4.94	12.319	1.89	37.167	4.92
1000	1.153	3.61	12.314	1.90	37.190	5.18
Not incl.	1.153	3.95	12.316	1.90	37.208	4.15

Table 5.3: Identified modal properties for varying SNR (for n_{max} = 30)

SSI for white noise and harmonic input

Another factor that is going to be investigated in the present section is the case where the input is not pure white noise, but it includes an harmonic component at frequency that is close to a natural frequency of the system. Additionally, it is considered that the response at the frequency of the harmonic excitation is comparable with the response at the natural frequency. The first harmonic has a frequency of 1.31rad/s, while the second is 1.45rad/s and is quite further away from the fundamental natural frequency.Figure 5.2 shows the stabilization diagrams for the two different harmonics, considering the three different algorithms of SSI.

As it can be shown, the algorithm of SSI-a is the only one that resulted in a stable mode. Still, for the case where the harmonic is very close to the natural frequency, the identified mode is shifted. In the rest two SSI algorithms no stable algorithm was identified. This leads to the conclusion that, despite the fact that SSI-b and SSI-Ov are able to identify modes hardly excited (*e.g.* fourth mode), they struggle in differentiating between closely spaced modes. As it is displayed in Figure 5.2, SSI-b attempted to obtain two sets of modes, but still the mode related to resonance is way unstable.

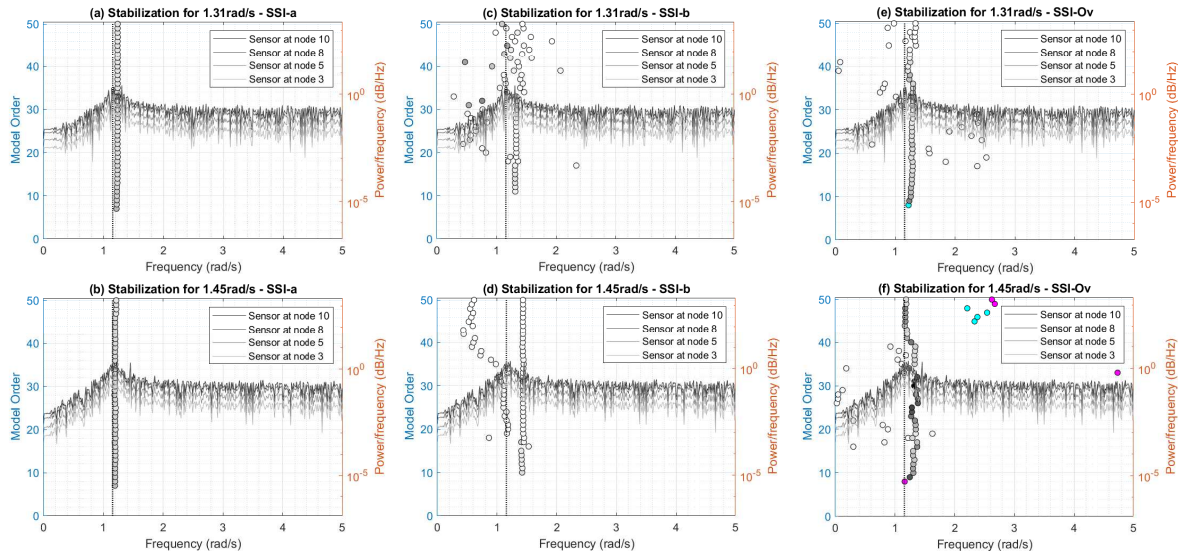

Figure 5.2: Stabilization diagram using SSI, zoomed at the fundamental natural frequency for two different harmonic components

SSI for wind, wave and current excitation

The simulated results that correspond to the OWT model in Matlab under environmental conditions will be also used for the identification of the modal parameters. All the inputs to the SSI algorithms are the same as described in the case of white noise input. The excitation input in this case is not a white noise process any more. Figure 5.3 shows the stabilization diagram for the algorithm of SSI-a.

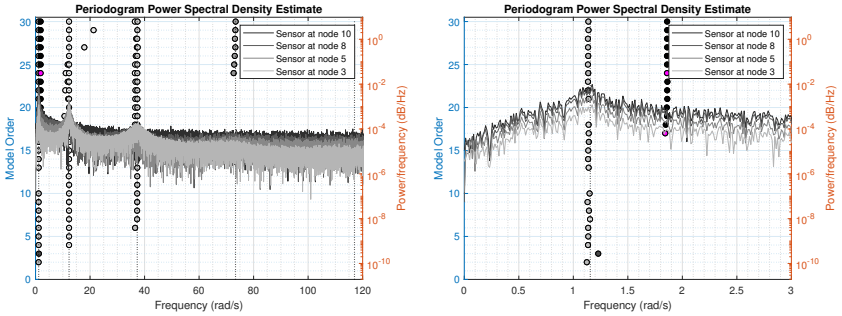

Figure 5.3: Stabilization diagram – SSI-a for wind, wave and current excitation

As it can be shown, all the first four modes are identified regardless the fact that the input was not white noise. Additionally, no mode was identified close to the region where wave energy is present. This can be mainly attributed to the fact that the system is relatively stiff with respect to the wave loading. The total results from all the three SSI algorithms can be shown in Table 5.4. An interesting observation is that SSI-a was also able to identify the fourth mode, while for the case of white noise input it was not. Finally, the fundamental natural frequency was in all the cases shifted towards lower frequencies and the related damping ratio was overestimated. The shift of the identified frequency may be attributed to the presence of wave, but it is unclear whether the larger values of damping are also related to the coloured input.

Mode	**Exact**		**SSI-a**		**SSI-b**		**SSI-Ov**	
	ω_d (rad/s)	ζ (%)	ω_d (rad/s)	ζ (%)	ω_d (rad/s)	ζ (%)	ω_d (rad/s)	ζ (%)
1	1.155	4.00	1.138	5.96	1.120	7.18	1.139	5.26
2	12.303	2.00	12.293	2.12	12.318	2.06	12.301	2.07
3	37.305	5.09	37.408	5.38	37.404	5.47	37.383	5.43
4	73.332	9.83	73.411	9.76	73.152	9.96		

Table 5.4: Identified and exact modal properties – SSI for wind, wave and current excitation (for $n_{max} = 30$)

5.2.2. SIMULATED RESPONSES USING MODEL IN FAST

In Section 5.2.1, three different SSI algorithms were applied on data derived from the OWT model in Matlab. It was found out that SSI is a pretty powerful technique, able to obtain stabilization diagrams that include the modes of mildly excited modes. Here, all these three algorithms will be applied on simulated data derived from the NREL offshore 5-MW baseline wind turbine. More information about the simulated cases can be found in Table 2.2.

The obtained data are accelerations at four points along the tower as shown in Figure 3.20 in Section 3.3.2. Time-series with 10min duration, and already truncated by FAST transient parts have been used for the identification. Additionally, measurement noise with SNR equal to 50 has been used to account for uncertainties and imperfections related to the data.

As far as the input variables to SSI algorithms is concerned, the value of row blocks has been selected to be i =100. Considering that and also the total number of data in each time-series is 38199, which leads in j =38199-2*100+2=38001 column blocks. The second important input to the SSI algorithms is the order of the system n. The problem of selecting a specific order has been tackled by generating stabilization diagrams of maximum order m_{max} =80. Finally, the sampling frequency was selected to be 63.66Hz.

Case FC1

FC1 is the first case, and corresponds to relatively small wind velocities, leading also into low rotor rotational speeds. Table 5.5 shows that the algorithms were able to identify almost all the flapwise blade bending modes, with a corresponding high value of damping, but still relatively smaller than the actual values. Apart from that, close to the regions where response is dominated by the harmonic excitation of 3P and 6P, no mode was able to be identified. This is attributed to the presence of the harmonic excitation. Regarding the tower modes, only the second was identified with also a good damping ratio. Unfortunately, the first mode was not identified.

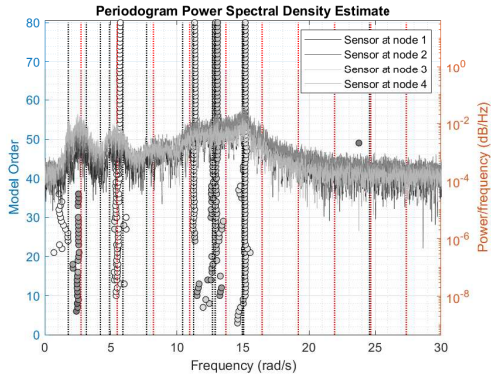

Figure 5.4: SSI-Ov - Stabilization diagram for FC1

Mode	Exact (8.5rpm)		SSI (FC1)		
	ω_d (rad/s)	ζ (%)	ω_d (rad/s)	ζ (%)	Alg.
B2-F2	11.260	10.80	11.308	0.95	SSI-b
			11.345	1.384	SSI-Ov
B1-F2	12.690	9.25	12.784	5.10	SSI-a
			12.778	7.57	SSI-b
			12.911	5.37	SSI-Ov
B3-F2	12.895	9.05	12.933	8.14	SSI-a
			12.895	5.26	SSI-b
			13.066	5.57	SSI-Ov
T-FA2	15.040	2.85	15.162	1.96	SSI-a
			15.153	2.73	SSI-b
			15.168	2.48	SSI-Ov

Table 5.5: SSI - Identified modal properties for FC1

Case FC2

In the second operating case, one may see several similarities to FC1. However, the harmonic excitation becomes stronger and the sensitive to mildly excited modes algorithms of SSI resulted in an almost stable mode at the region where 18P is present. This means that even the second bending tower mode might be affected by the presence of the neighbouring 15P excitation. As it can be shown, B1-F2 and B1-F3 are both quite shifted towards higher frequencies, probably due to 12P. Apparently, the related damping ratios are also in this case lower than the exact damping.

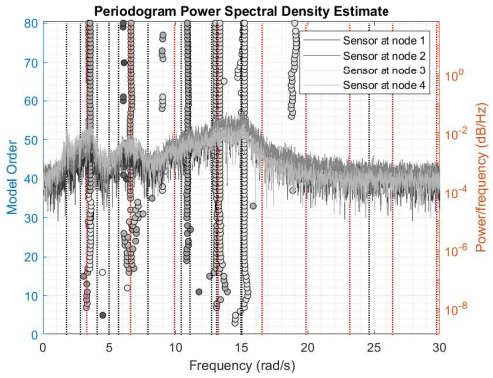

Figure 5.5: SSI-Ov - Stabilization diagram for FC2

Mode	Exact (10.5rpm)		SSI (FC2)		
	ω_d (rad/s)	ζ (%)	ω_d (rad/s)	ζ (%)	Alg.
B2-F2	11.105	13.60	10.839	8.33	SSI-a
			10.756	9.01	SSI-b
			10.910	8.41	SSI-Ov
B1-F2	12.730	11.50	13.048	3.90	SSI-a
			13.100	5.08	SSI-b
			13.032	4.43	SSI-Ov
B3-F2	13.120	10.45	13.360	3.34	SSI-a
			13.397	3.45	SSI-b
			13.359	3.14	SSI-Ov
T-FA2	15.015	3.45	15.138	2.07	SSI-a
			15.195	1.95	SSI-b
			15.132	1.23	SSI-Ov

Table 5.6: SSI - Identified modal properties for FC2

Case FC3

In FC3 the external excitation seems to dominate over the full frequency band of the identification. This can be concluded due to the fact that modes were identified only around nP regions. An attempt was made by SSI-b to find double stable modes around 3P, but it is unclear whether it is related to mode B1-F1, or not. Another questionable mode is the flapwise blade bending mode B2-F2 which coincides with 9P. Therefore, in under these operating conditions, the only mode that was identified is the second fore-aft tower bending mode.

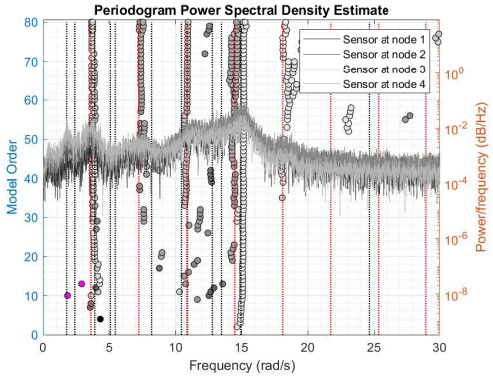

Figure 5.6: SSI-Ov - Stabilization diagram for FC3

Mode	Exact (11.5rpm)		SSI (FC3)		
	ω_d (rad/s)	ζ (%)	ω_d (rad/s)	ζ (%)	Alg.
B1-F1	4.040	49.35	3.912	5.48	SSI-b
B2-F2 (& 9P)	11.030	14.70	11.028	4.30	SSI-a
			11.016	7.87	SSI-b
			10.954	4.99	SSI-Ov
T-FA2	14.995	3.75	15.140	1.89	SSI-a
			15.031	1.90	SSI-b
			15.117	1.88	SSI-Ov

Table 5.7: SSI - Identified modal properties for FC3

Case FC4

In the last operating loading case, only the second bending mode of the tower has been identified. Here, the external harmonic excitation is considerably larger than before, and as it can be shown in Figure 5.7 non-structural forcing modes have been identified from 3P up until 21P. The region close to 9P seems to have gathered several modes, since several semi-stable modes have been identified. In case they are related to blade modes, they are highly shifted due to the external loading.

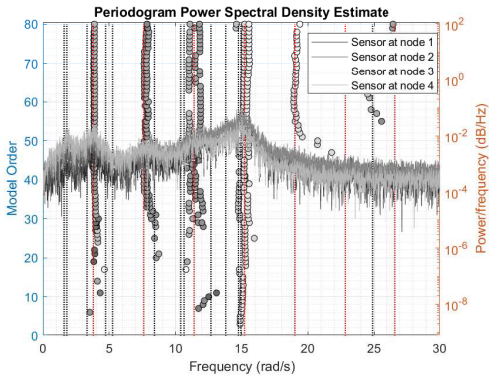

Figure 5.7: SSI-Ov - Stabilization diagram for FC4

Mode	Exact (12.1rpm)		SSI (FC4)		
	ω_d (rad/s)	ζ (%)	ω_d (rad/s)	ζ (%)	Alg.
T-FA2	14.758	4.34	15.12	2.73	SSI-a
			15.08	2.81	SSI-b
			15.23	2.73	SSI-Ov

Table 5.8: SSI - Identified modal properties for FC4

Case FC5

Finally, FC5 corresponds to a parked turbine, without any external harmonic excitation. As it can be shown in Figure 5.8, the number of modes that have been identified is way larger than in previous cases. Both the tower modes have been identified, together with several blade modes. Starting with the flawpise first blade bending modes, it is shown that they are very close to each other and this is probably the reason behind the excessively large values of damping ratios. Then, the flapwise bending modes are coincident and the identification leaded into a single mode with good damping values, regardless of the algorithm that was used. Finally, one collective flawpise second blade bending mode (B1−F2) and one asymmetric (B2−F2) were nicely identified with minor differences in the damping ratios.

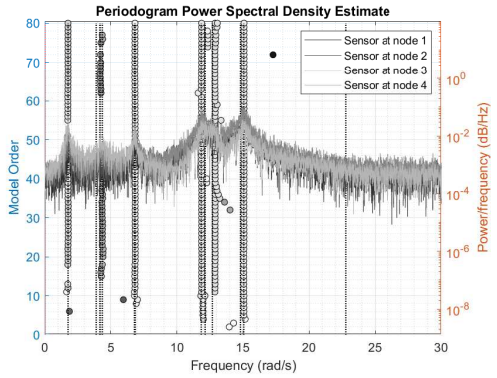

Figure 5.8: SSI−Ov - Stabilization diagram for FC5

Mode	Exact (0rpm)		SSI (FC5)		
	ω_d (rad/s)	ζ (%)	ω_d (rad/s)	ζ (%)	Alg.
T-FA1	1.760	0.28	1.79	4.11	SSI-a
			1.76	4.60	SSI-b
			1.76	4.16	SSI-Ov
B3-F1	4.187	0.67	4.19	7.37	SSI-b
			4.21	8.65	SSI-Ov
B2-F1	4.350	0.69	4.37	10.11	SSI-a
B2-E1	6.847	1.09	6.83	1.09	SSI-a
			6.83	1.10	SSI-b
			6.83	1.01	SSI-Ov
B2-F2	11.836	1.88	11.89	2.02	SSI-a
			11.89	2.33	SSI-b
			11.87	2.25	SSI-Ov
B1-F2	12.680	2.02	12.90	2.38	SSI-a
			12.90	2.82	SSI-b
			12.91	2.76	SSI-Ov
T-FA2	15.055	2.40	15.06	1.84	SSI-a
			15.06	1.54	SSI-b
			15.07	1.54	SSI-Ov

Table 5.9: SSI - Identified modal properties for FC5

5.3. CONCLUSIONS

In the end of this chapter, three different approaches of SSI method were used for the identification of simulated data using the OWT model in Matlab. Initially, several inputs to SSI algorithms were investigated, and then they were used for the identification considering white noise excitation with or without a harmonic components and also considering the simplified environmental conditions used in the model in Matlab. It was found out that SSI is quite stronger that ERA in identifying not highly excited modes, but it is less powerful when it comes to closely spaced modes and modes. In general, it resulted in acceptable damping ratios when applied to white noise input.

Then, in 5.2.2, the algorithms were applied on simulated data obtained from the OWT model in FAST, which accounted for the complex influence of more accurate environmental conditions. It was found out that SSI obtained more stable modes, but was able to identify less modes. A possible reason could be the fact that the projection matrix $\mathbf{O}_i$ is derived from a multiplication of Hankel matrices that include shifted data. This results in some kind of covariance matrix, which has removed the influence of the stochastic white noise input. A similar idea was presented in Section 4.2, when the theory behind NExT was explained. However, the difference is that in ERA/NExT, only the first part of the correlation function is considered for the identification (almost 5%), while in SSI the whole time-series will be used. Therefore, several transient parts related to the input, or/and the time-invariant behaviour of the system might result in a less impulse-like signal and affect the identification of stable modes. This could be the reason why SSI was largely affected by the violation of the OMA assumptions.

Another observation that is in agreement with the results of ERA/NExT is that the high damping ratios related to the flapwise blade bending modes were also largely underestimated. Finally, all the SSI algorithms run twice for each identification, to filter out the unstable modes. In that step, the first fore-aft tower bending mode was also removed due to unstable damping.

6

FREQUENCY DOMAIN DECOMPOSITION

Frequency Domain Decomposition (FDD) is an OMA technique, able to derive the modal properties of an unknown system by working with the auto/cross - Power Density Spectra of the responses in frequency domain. In this chapter the theory behind both FDD and also Enhanced FDD will be explained and in the end the algorithm will be applied on simulated data.

6.1. THEORY BEHIND FDD

Frequency Domain Decomposition (FDD) is probably the most popular OMA system identification technique that operates in frequency-domain instead of time-domain. The main reason of being so widely used is the high speed and the ease of implementation compared to other OMA techniques. This user-friendly method was initially introduced by Brincker et al.[55] in 2000, aiming at the determination of the natural frequencies and the mode shapes of the system of interest. However, as it will be explained later on, the accuracy of the natural frequencies obtained by FDD is largely affected by the frequency resolution of the output cross power spectral densities. An expansion to FDD was introduced one year later by Brincker et al.[56], which in literature may be referred to as Enhanced Frequency Domain Decomposition (EFDD). This approach allows also the estimation of damping, while in parallel it leads into a more precise estimate of the natural frequencies by tackling the aforementioned resolution problem. As we will see later on, FDD does not need to make assumptions about the order of the system as in time-domain techniques, due to the fact that the modes are simply selected by the user via visual inspection. This implies that FDD is not as automated as the methods described in the past chapters, even though several studies have been made to apply FDD in an automated way[57]. In presence of harmonic excitation, FDD method may be affected in case where the harmonic has a frequency close to a mode. In that way, the estimate will probably be biased. Therefore, harmonic components should be relatively far from the structural modes. In 2006, Jacobsen et al. proposed a way to remove the influence of with closely spaced harmonics based on the statistical properties of the random and harmonic signals.

Similar to most of OMA frequency-domain methods, FDD starts by assuming that the system is an LTI system. Therefore, the output spectrum $\mathbf{X} \in \mathbb{C}^{mx1}$ will be just the product of the input spectrum $\mathbf{F} \in \mathbb{C}^{rx1}$ and the system's frequency response function $\mathbf{H} \in \mathbb{C}^{mx1}$. The number of sensors is denoted by m, and the (unknown) number of forces by r.

$$\mathbf{X}(\omega) = \mathbf{H}(\omega)\,\mathbf{F}(\omega) \tag{6.1}$$

The relationship between the input and output auto/cross-PSD matrices for stochastic process can be obtained by post-multiplying Eq.6.2 by its Hemitian matrix (conjugate transpose).

$$\begin{aligned} \mathbf{X}(\omega)\mathbf{X}^H(\omega) = \mathbf{H}(\omega)\,\mathbf{F}(\omega)\,\mathbf{F}^H(\omega)\,\mathbf{H}^H(\omega) \rightarrow \\ \mathbf{S}_{xx}(\omega) = \mathbf{H}(\omega)\,\mathbf{S}_{ff}(\omega)\,\mathbf{H}^H(\omega) \end{aligned} \tag{6.2}$$

where, $\mathbf{S}_{xx} \in \mathbb{C}^{mxm}$ and $\mathbf{S}_{ff} \in \mathbb{C}^{rxr}$ are output and input auto/cross-PSD matrix, respectively.

The second assumption in FDD is that the input is supposed to be approximated by a broadband white noise stochastic process. By definition, a zero-mean white noise process has autocorrelation function that satisfies the Eq.6.3.

$$\mathbf{C}_{ff}(\tau) = E(\mathbf{f}(t+\tau)\mathbf{f}(t)) = \mathbf{C}\delta(\tau) \tag{6.3}$$

where, $\mathbf{C} \in \mathbb{C}^{rxr}$ is a constant matrix proportional to the identity matrix. This means that the auto-correlation function of the input is similar to an impulse at time equals to τ. The auto-PSD of the input can be determined by apply Fourier transform on the autocorrelation function. The resulting spectrum will be constant, as shown in Eq.6.4.

$$\mathbf{S}_{ff}(\omega) = \mathbf{C} \tag{6.4}$$

Here, one may better understand the theory of NExT, by looking into the problem in frequency-domain. From that perspective, $\mathbf{S}_{ff}$ is directly related to impulse response. Therefore, by inverting $\mathbf{S}_{ff}$, the cross-correlation functions that will be obtained are directly linked to the free response.

By substituting Eq.6.4 into Eq.6.2, the following expression can be derived.

$$\mathbf{S}_{xx}(\omega) = \mathbf{H}(\omega)\mathbf{C}\mathbf{H}^{H}(\omega) \propto \mathbf{H}(\omega)\mathbf{H}^{H}(\omega) \tag{6.5}$$

Eq.6.5 is of great importance, since it shows that the output holds the modal characteristics of the system. This equation is the starting point of most of frequency-domain OMA techniques. Finally, the structure is assumed to be excited at multiple locations, so that all the modes of interest are excited (controllable), by uncorrelated white noise forces (off-diagonal terms of the **C** are zero).

Before describing the steps of FDD, two approaches will be presented to explain the modal decomposition of the output PSD matrix.

1st Approach

In the first approach, the FRF will be expressed using the partial fraction expansion form (poles and residues) of Eq.6.6.

$$\mathbf{H}(\omega) = \sum_{k=1}^{n} \frac{\mathbf{R}_k}{i\omega - \lambda_k} + \frac{\bar{\mathbf{R}}_k}{i\omega - \bar{\lambda}_k} \tag{6.6}$$

where, in this equation n is the total number of DoF, λ_k, $\bar{\lambda}_k$ are the poles (pair of complex conjugate roots of the denominator), and $\mathbf{R}_k \in \mathbb{C}^{mxr}$ is the residue matrix. Also, when using this formulation of **H**, the residue can be calculated as $\mathbf{R}_k = \boldsymbol{\phi}_k \boldsymbol{\gamma}_k^T$, where $\boldsymbol{\phi}_k \in \mathbb{C}^{mx1}$ is the mode shape vector of mode k and $\boldsymbol{\gamma}_k \in \mathbb{C}^{rx1}$ is the related modal participation factor vector. By substituting 6.6 in the first part of 6.5, and after several mathematical manipulations, the output PSD matrix can be also written in its pole/residue form.

$$\mathbf{S}_{xx}(\omega) = \sum_{k=1}^{n} \frac{\mathbf{A}_k}{i\omega - \lambda_k} + \frac{\bar{\mathbf{A}}_k}{i\omega - \bar{\lambda}_k} + \frac{\mathbf{A}_k^{\mathrm{T}}}{-i\omega - \lambda_k} + \frac{\mathbf{A}_k^{\mathrm{H}}}{-i\omega - \bar{\lambda}_k} \tag{6.7}$$

where, $\mathbf{A}_k \in \mathbb{C}^{mxm}$ is the residue matrix and can be determined by considering the influence of all n modes of the system as shown in Eq.6.8.

$$\mathbf{A}_k = \sum_{s=1}^{n} \left(\frac{\mathbf{R}_s}{-\lambda_k - \lambda_s} + \frac{\bar{\mathbf{R}}_s}{-\lambda_k - \bar{\lambda}_s} \right) \mathbf{C}\mathbf{R}_k^T \tag{6.8}$$

Since for $s = k$, the denominator in Eq.6.8 tends to zero, it can be concluded that the residue of $\mathbf{S}_{xx}$ close to mode k is dominated by the presence of mode $\boldsymbol{\phi}_k$. In other words, the rest modes apart from mode k have a minor influence on $\mathbf{A}_k$. Additionally, for sub-critically damped systems it can be proved that $\mathbf{A}_k \approx \mathrm{d}_k \boldsymbol{\phi}_k \boldsymbol{\phi}_k^T$. By substituting this approximation of the residue into Eq.6.7, in the vicinity of a natural frequency k, the output PSD matrix can be expressed by the following equation.

$$\mathbf{S}_{xx}(\omega) \approx \sum_{kESub(\omega)}^{n} \left(\frac{\mathrm{d}_k \boldsymbol{\phi}_k \boldsymbol{\phi}_k^T}{i\omega - \lambda_k} + \frac{\mathrm{d}_k \bar{\boldsymbol{\phi}}_k \bar{\boldsymbol{\phi}}_k^T}{-i\omega - \bar{\lambda}_k} \right) = \boldsymbol{\Phi}\, diag\left(Re\left(\frac{2\, d_k}{i\omega - \lambda_k} \right) \right) \boldsymbol{\Phi}^H \tag{6.9}$$

This expression describes the modal decomposition of the output PSD matrix and implies that close to a specific frequency ω, only a small number of modes will play an important role in the PSD. The full derivation is explained by Brincker et al.[55] and also in [58].

2nd Approach

An easier way to understand the modal decomposition of the output PSD matrix can also be illustrated by starting from the main principle of modal analysis. In that way, the response $\mathbf{x} \in \mathbb{R}^{mx1}$ of the system can be written as the superposition of the modal coordinates, considering also the related mode vectors.

$$\mathbf{x}(t) = \sum_{k=1}^{n} \boldsymbol{\phi}_k \boldsymbol{q}_k(t) = \boldsymbol{\Phi}\mathbf{q}(t) \tag{6.10}$$

Then, the correlation matrix $\mathbf{C}_{xx}$, which includes all the correlation functions of the responses, can be calculated as follows.

$$\mathbf{C}_{xx}(t) = E\left[\mathbf{x}(t)\mathbf{x}(t)^T\right] = E\left[\boldsymbol{\Phi}\mathbf{q}(t)\,\mathbf{q}(t)^T\boldsymbol{\Phi}^T\right] = \boldsymbol{\Phi}E\left[\mathbf{q}\mathbf{q}^T\right]\boldsymbol{\Phi}^T = \boldsymbol{\Phi}\mathbf{C}_{qq}\boldsymbol{\Phi}^T \tag{6.11}$$

An equivalent relation in frequency-domain can be derived after applying Fourier transform.

$$\mathbf{S}_{xx}(\omega) = \boldsymbol{\Phi}\mathbf{S}_{qq}(\omega)\boldsymbol{\Phi}^H \tag{6.12}$$

In case where the modal coordinates are uncorrelated, then $\mathbf{S}_{qq}$ will be diagonal. Also, for orthogonal mode shapes $\boldsymbol{\Phi}$, this expression is equivalent to Eq.6.9.

Step - 1 Auto/cross-PSD matrix

As shown before, the theory of FDD is ends at an expression which includes the auto/cross-PSD matrix $\mathbf{S}_{xx} \in \mathbb{R}^{mxm}$. Therefore, the first step of this algorithm is the determination of this matrix. In practice, this is most of the times done by using already existing Matlab functions (*e.g.* `cpsd`) for all possible combinations of the response time series.

Step - 2 Singular Value Decommission

Once the PSD matrix is computed at discrete frequency lines, then it is decomposed into three matrices by performing SVD.

$$\mathbf{S}_{xx}(\omega) = \mathbf{U}\mathbf{S}\mathbf{V}^H \tag{6.13}$$

where $\mathbf{U}$ and $\mathbf{V} \in \mathbb{C}^{mxm}$ are orthogonal matrices that hold the singular vectors and $\mathbf{S} \in \mathbb{C}^{mxm}$ is the diagonal matrix that includes the singular values of $\mathbf{S}_{xx}$. In case where all the outputs are used as references in the PSD matrix, then $\mathbf{U}$ and $\mathbf{V}$ are identical. As explained before by the theory behind of FDD, at a given frequency range a small number of modes will be dominant. Assuming that inside a given frequency region only the k^{th} mode is dominating, then the PSD matrix at that given frequency range will have rank equal to one. In other words, one singular value will be non-zero compared to the others and the PSD matrix will be approximated by the following equating.

$$\underset{\omega \to \omega_k}{\mathbf{S}_{xx}}(\omega) \approx \mathbf{u}_{1k} s_{1k} \mathbf{u}_{1k}^H \tag{6.14}$$

Hence, for given frequency lines, the related first singular vector of matrix $\mathbf{U}$ can be directly related to mode shape k as shown in Eq.6.15.

$$\boldsymbol{\phi}_k = \mathbf{u}_{1k} \tag{6.15}$$

For the case of multiple closely spaced modes, or even overlapping modes, the rank of PSD matrix will be equal to the number the modes that dominate that given frequency region. Therefore, displaying graphically the singular values along the frequency range is a common practice to indicate the locations where resonance occurs. The natural frequency of the relative mode can be directly obtained by the frequency line of the peak. Additionally, multiple peaks with more than one singular values non-zero will indicate that multiple modes are present at that region. Another advantage of FDD is that instead of using a bunch of output PSDs, the identification is based on a smaller number of singular value functions in frequency domain, which summarize all the modal information of the output PSDs.

It need to be mentioned that for the case where the system is excited also by an harmonic component, almost all the modes will be excited significantly and this will lead in almost full-rank PSD matrix at the frequency region around the frequency of the harmonic.

FDD, as explained by Brincker et all.[55], stops at that step. This means that this technique is incapable of obtaining the modal damping ratios of the system modes. From now on the so-called EFDD comes into play and aims at obtaining a more elaborated estimate of the natural frequency and of course modal damping.

Step - 3 Modal Assurance Criterion

In this step, EFDD suggests a way to obtain a Single-Degree-Of-Freedom (SDoF) bell function around an identified mode. The main idea is that, due to resonance, a whole range will be dominated by the given mode. Inside this range, the system may be assumed to behave as a SDoF, decomposed from the rest modes of the system. In that range, the PSD matrix will have singular vectors that are largely close to the mode shape. The limits of that region can be defined by calculating a Modal Assurance Criterion (MAC) between the singular vector of the frequency line that corresponds to a peak of the singular values $\mathbf{u}_{1k} \in \mathbb{C}^{mx1}$ (reference vector) and the singular vectors of the neighbouring frequency lines $\mathbf{u}_{1i} \in \mathbb{C}^{mx1}$.

$$MAC = \frac{\left|\mathbf{u}_{1k}^H \mathbf{u}_{1i}\right|^2}{\left(\mathbf{u}_{1k}^H \mathbf{u}_{1k}\right)\left(\mathbf{u}_{1i}^H \mathbf{u}_{1i}\right)} \tag{6.16}$$

The singular values that correspond to a MAC factor larger than a user-specified MAC threshold level will be included in the frequency region, while the rest will be neglected. A small threshold will lead into larger number of singular values, but with less intense presence of the corresponding mode.

Step - 4 Auto-PSD of SDoF

Once the limits of the frequency range around a mode k have been determined according to the MAC factor, a SDoF spectral bell is defined as the part of the singular values around the selected peak with large MAC factor. Outside the limits of the frequency range the values of the SDoF spectral bell is set to zero. This part of the singular values can be interpreted as the auto-PSD of the modal coordinates ($\mathbf{S}_{qq}(\omega)$, for ω close to the k^{th} peak) and can be used for the determination of the modal damping ratio and the natural frequency. Therefore, the estimates might be biased in case where the bell expands over a frequency range with harmonic input components.

One way to obtain an averaged mode shape is to calculate the mode shape as a weighted average of the mode shapes along the SDoF bell, using as weights frequency of the correspondent frequency line.

Step - 5 Derive modal parameters from free decay

In the last step, all the auto-PSD functions, which have been collected from each pick of the singular value plot, will be inverted from frequency-domain into time-domain using the inverse discrete Fourier transform (IDFT). As it can be deduced, by inverting the auto-PSD functions, the related cross-correlation functions will be obtained. These functions are more or less the free decay response of each SDoF system. Hence, for each peak, both the corresponding natural frequency and damping ratio can then calculated by the logarithmic decrement technique. Therefore, EFDD identifies the modal parameters from time-series and can be characterized as a combined frequency-time-domain method.

At first, the natural frequency is determined by looking into the zero-crossing times of the free decay. Then by applying linear regression ($y = \alpha + \beta x$) on time moments of each crossing (y) and the relative crossing times (x), the natural frequency may be calculated as $\omega_k = 2\pi/T$, for $T = \alpha + 2\beta$. In that way, the accuracy on the estimated natural frequency increases and is not affected by the frequency resolution as much as in FDD.

Finally, damping can be obtained from the logarithmic decrement. The extremes r_j of each peak and trough j of the free decay time-series are at first collected. Then the logarithmic decrement δ is governed by expression Eq.6.17 and can be calculated via linear regression ($y = \alpha + \beta x$) for $y = ln\left(\left|r_j\right|\right)$ and $x = -j/2$.

$$\delta = \frac{2}{j}\ln\left(\frac{r_0}{\left|r_j\right|}\right) \rightarrow \frac{\delta j}{2} = \ln(r_0) - \ln\left(\left|r_j\right|\right) \rightarrow \ln\left(\left|r_j\right|\right) = \ln(r_0) - \frac{j}{2}\delta \tag{6.17}$$

Then, after determining the logarithmic decrement δ, the damping ratio of the SDoF can be calculated based on Eq.6.18.

$$\zeta = \frac{\delta}{\sqrt{\delta^2 + 4\pi^2}} \tag{6.18}$$

In that way, both natural frequencies and damping ratio can be obtained, at the selected peaks of the singular value diagram.

6.2. NUMERICAL RESULTS

FDD and EFDD will be applied in the current section on simulated data. As described in Section 6.1, FDD is applied in a non-automated way, by selecting manually peaks from the singular value diagram. This is the first user-made decision. Once the peak has been selected and the SDoF auto-PSD has been determined and re-inverted back to time-domain, then the user needs to select the part of the time-domain impulse response in order to obtain the modal properties. Aiming at increasing the accuracy of the algorithm, the selection of the free decay is performed multiple times, and based on the resulting modal properties, a pseudo-stabilization diagram is built. In that diagram, the model order is replaced by the number of the iterations. In the end, the identified modal properties are obtained as the mean values of all the iterations. Despite the fact that when damping is also identified the algorithm is named as EFDD, from now on the algorithm that will be applied to the responses will be referred to as FDD.

6.2.1. SIMULATED RESPONSES USING MATLAB MODEL

FDD for white noise input

At first, FDD will be applied on simulated responses from the OWT model in Matlab, loaded by a white noise input. More details about the loading cases can be found in Section 3.2.2. In the first step, the auto/cross PSDs are calculated based on the response time-series. Before deriving these spectra, the time-series are corrupted by measurement noise of SNR equal to 50 and are divided into two blocks to obtain an averaged estimation of the PSDs and limit the influence of noise. Keep in mind that the first 100s of the time-series are truncated from the responses to remove the transient part. Using these PSD matrices, the spectrum of singular values can be obtained via SVD. Then three peaks can be selected as shown in Figure 6.1(a). These parts of the spectrum represent the auto-PSDs of each SDoF and are isolated from the rest singular values according to the selected value of MAC factor (here =80%). In the next step, these spectra and inverted into time-domain in order to derive the impulse response of each of the three modes. The related free decay for the first mode can be displayed in Figure 6.1(b). In the end this impulse response is used to derive the modal properties. This whole procedure is very fast and can be applied in an iterative manner to derive a pseudo-stabilization diagram. Figure 6.1(c) shows this diagram for 20 iterations.

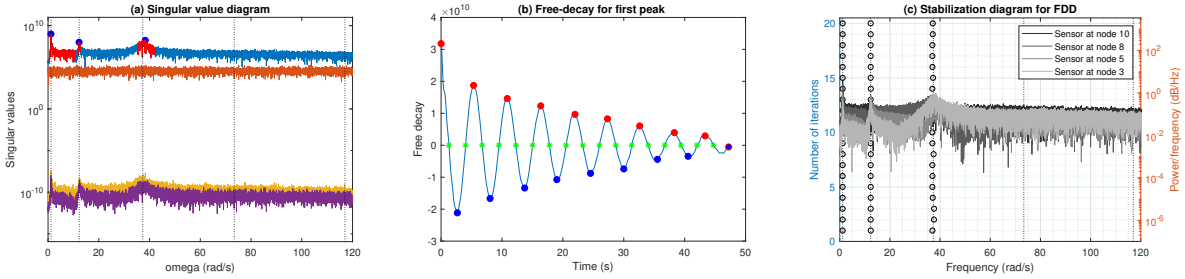

Figure 6.1: Stabilization diagram - FDD for white noise input

The average value of all these 20 iterations can be shown in Table 6.1. The derived modal properties are close to the exact values. However, the singular values did not show any amplification close to the fourth mode, and therefore, this mode was not able to be identified.

Mode	Exact		FDD (white noise)	
	ω_d (rad/s)	ζ (%)	ω_d (rad/s)	ζ (%)
1	1.155	4.00	1.155	3.94
2	12.303	2.00	12.407	2.15
3	37.305	5.09	37.692	5.12

Table 6.1: Identified and exact modal properties - FDD for white noise input

FDD for white noise and harmonic input

In this paragraph, the influence of a harmonic component on the identification is investigated. This can be done by adding an harmonic component in the white noise excitation. Three cases have been considered

for harmonics at frequencies 1.31rad/s, 1.45rad/s and 1.76rad/s. Hence, it is clear that attention will be focused on the first mode. Measurement noise has been deactivated for the purpose of this given task. The rest settings are the same as described in application for white noise input. Figure 6.2 shows the stabilization diagrams for 20 iterations. As it can be shown, for the case where the harmonic is very close to the fundamental natural frequency, the identified mode is very unstable. However, when the harmonic starts moving away from the mode, the identification becomes more and more stable.

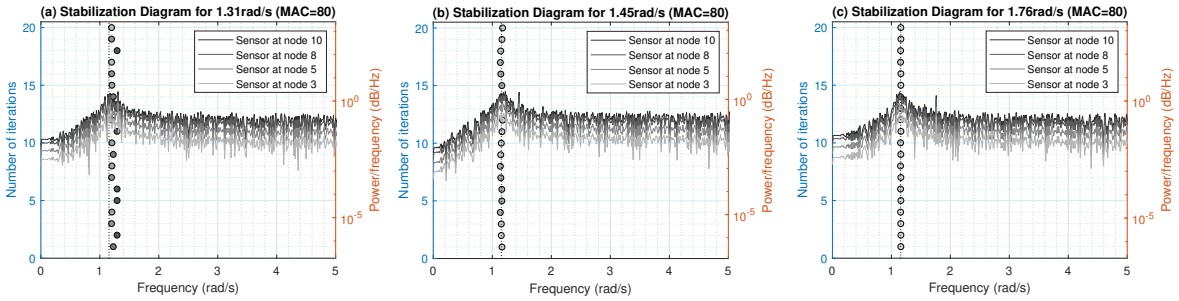

Figure 6.2: Stabilization diagram, zoomed at the fundamental natural frequency - FDD for white noise and harmonic input

An alternative attempt was made to reduce the MAC factor from 80% to 95% so that the harmonic will outside the SDoF bell, but still the identification was unstable for 1.31rad/s.

FDD for wind, wave and current excitation

Similar to the past two algorithms, the algorithm will be tested also for the case where the OWT model is loaded by wind, wave and current. The settings of FDD are the same as described in the case of white noise input. What changes is that for a MAC equal to 80%, the SDoF of the third mode was too small and this leaded in an underestimation of the modal damping. Therefore, a MAC factor of 75% has been selected to derive a wider SDoF bell. According to Figure 6.3, the three first modes have been stably identified. An attempt was made also to identify the fourth mode, but even for small MAC factors, no SDoF bell curve was able to be determined. In other words, there is no dominant mode at that frequency region.

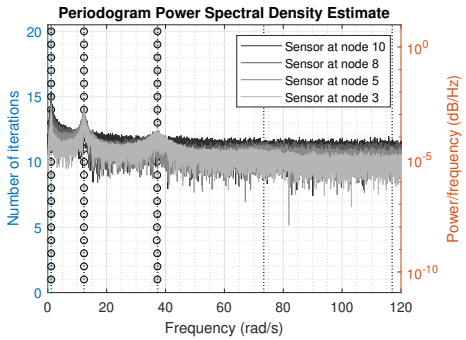

Figure 6.3: Stabilization diagram - FDD for wind, wave and current input

The results of the identification can be shown in Table 6.2. Similar to ERA/NExT and SSI, the first mode is slightly shifted towards smaller frequencies. It is still unclear whether this shift is related to the presence of wave, or this small difference is a typical deviation from the exact values.

Mode	Exact		FDD (env.cond.)	
	ω_d (rad/s)	ζ (%)	ω_d (rad/s)	ζ (%)
1	1.155	4.00	1.146	5.18
2	12.303	2.00	12.307	2.29
3	37.305	5.09	37.240	4.25

Table 6.2: Identified and exact modal properties - FDD for wind, wave and current excitation

6.2.2. SIMULATED RESPONSES USING MODEL IN FAST

In the present section FDD algorithm will be applied on the simulated cases from the model in FAST described in Section 2.2. These data correspond to input loading and system that violate both white noise and LTI assumption. In addition, FDD assumes that the system is lightly damped. In case where this condition is violated, the expression of Eq.6.9 is not valid any longer. Still, Eq.6.12 holds and the singular values can be used as an indicator of the auto-PSD of the modal coordinates.

Regarding the algorithm of FDD, the user is asked to determine the peaks that might correspond to modes. Therefore, the identification is not an automated procedure like ERA/NExT and SSI. Additionally, one shall be critical about the SDoF bell curve that is determined using a given MAC factor, since, as showed in the application on the data from the model in Matlab for wind, wave and current input, the bell curve might be too narrow. This will probably result in an underestimation of the damping ratio. On the other hand, using a highly decreased MAC factor will result in a SDoF where the presence of the given mode is less dominant. Hence, the MAC factor that will be used is up to the engineer's judgement.

Before going into details, the response time-series derived from FAST are initially corrupted with measurement noise, and then divided into blocks. This aims at obtaining averaged PSDs and smoothing out the influence of measurement noise. The sampling frequency is selected to be 63.66Hz, so that the maximum energy inside the spectrum would be 200rad/s. This takes into account the Nyquist frequency, and ensures that no aliasing would affect the response spectra. In fact, most of the energy of the response spectra is gathered below 20rad/s. Then, the singular value spectrum can be derived by applying SVD on the auto/cross PSD. This spectrum for the first loading case FC1 can be shown in Figure 6.4.

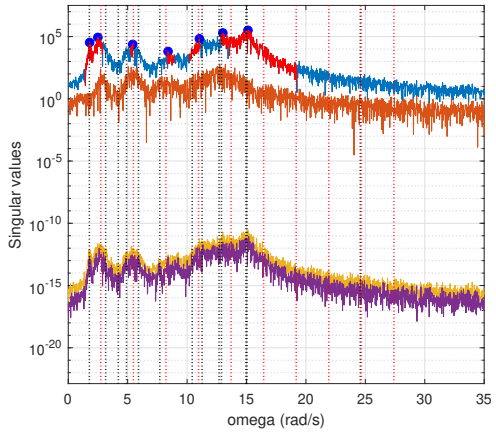

Figure 6.4: Singular value spectrum, including selected peaks for FC1 and MAC = 95%

As described in theory, the singular values are an indicator of the number of modes that contribute significantly in the PSD at a given frequency range. In case where the second mode shows also a peak at a given frequency range, then there might be a second mode close to the first one. However, the case where all the singular values are amplified, can be explained by the presence of external loading. An important observation is that the peaks at the region of the tower bending modes are not repeated at the second singular value plot. This is not the case for the nP and the region where blade modes are dominant. Therefore, probably the blade modes are interpreted as external loading and not a mode.

In Figure 6.4 one may see that in total 7 peaks have been selected. The SDoF bell curves have been determined using a MAC factor of 95%. Initially, a value of 75 was used, but the 5^{th} peak resulted in a SDoF bell curve that covered a very wide range, including the second tower bending mode. When the mac factor was educed to 85%, the range of the SDoF bell reduced, but still included the 6^{th} peak. In order to obtain a mode that corresponded only to the 5^{th} peak, the MAC had to increase to 95%. The same procedure has been followed for all the peaks so that the identified mode corresponds to the selected peak (do not shift) and also have as wide as possible SDoF bell curve for better damping ratio estimation.

Case FC1

As it can be shown in Figure 6.5, four modes were identified using FDD. However, the first fore-aft tower bending mode needed an extremely higher value of MAC in order to derive a SDoF that does not expand at

frequencies close to 3P. Additionally, two flapwise blade bending modes have been identified with relatively high damping ratio, but still lower than the corresponding exact values. Further than that, the second tower bending mode was identified with also a good estimate of damping. The rest region at lower frequencies was dominated by the presence of the input harmonic components and no mode was able to be identified.

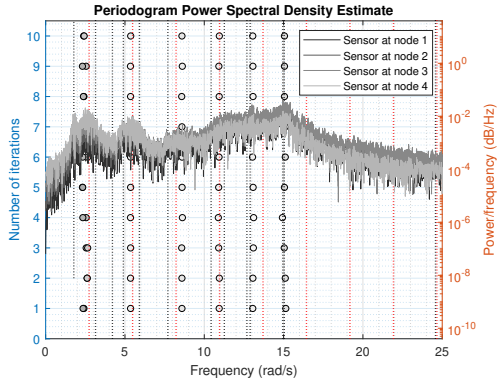

Figure 6.5: FDD - Stabilization diagram for FC1 and MAC = 95%

Mode	Exact (8.5rpm)		FDD (FC1)		
	ω_d (rad/s)	ζ (%)	ω_d (rad/s)	ζ (%)	MAC (%)
T-FA1	1.780	6.15	1.8232	3.71	99.2
B2-F2	11.260	10.80	11.932	7.12	95
B3-F2	12.895	9.05	13.044	6.75	90
T-FA2	15.040	2.85	15.041	3.39	90

Table 6.3: FDD - Identified modal properties for FC1

Case FC2

The stabilization diagram of Figure 6.6 corresponds to 7 peaks for MAC factor equal to 95%. As it can be shown, only one mode was identified in a stable way (B2-F2). The second bending mode of the tower was unstable due to the influence of the neighbouring flapwise blade modes. However, using larger MAC factors isolated the SDoF bell curves from the rest singular values for both the tower modes and resulted in stable identification. Unfortunately, the region close to 12rad/s seemed to include a mode, but even for very large MAC values it was not able to differentiate from tower mode. Finally, the rest modes shown in the figure are nP.

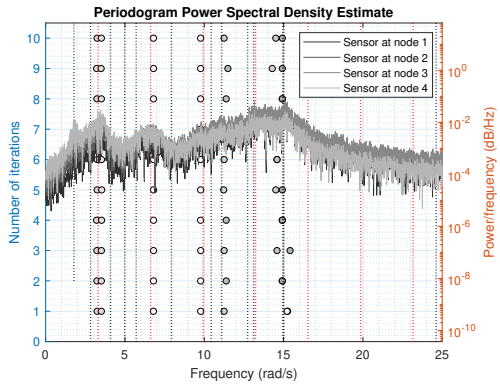

Figure 6.6: FDD - Stabilization diagram for FC2 and MAC = 95%

Mode	Exact (10.5rpm)		FDD (FC2)		
	ω_d (rad/s)	ζ (%)	ω_d (rad/s)	ζ (%)	MAC (%)
T-FA1	1.785	7.30	1.823	5.01	96
B2-F2	11.105	13.60	11.249	4.95	90
T-FA2	15.015	3.45	15.24	3.44	99

Table 6.4: FDD - Identified modal properties for FC2

Case FC3

As it can be shown from Figure 6.7, the identification using a MAC factor equal to 95% resulted in several non-structural modes (at 3P and 3P), two shifted modes (T-FA1 and a blade mode) and a stable tower mode T-FA2. Then, higher values ofMAC factor stabilized the tower mode T-FA1 and also leaded in the blade mode B3-F2. Unfortunately, the rest flapwise blade bending modes could not be isolated from the influence of the tower mode T-FA2.

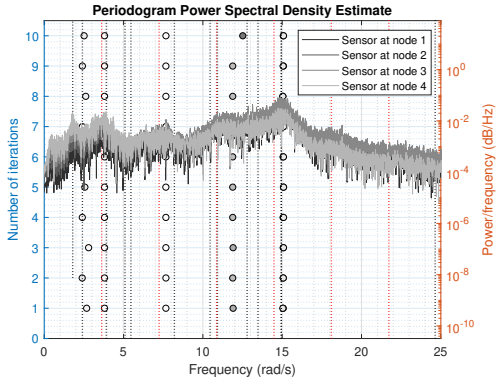

Figure 6.7: FDD - Stabilization diagram for FC3 and MAC = 95%

Mode	Exact (11.5rpm)		FDD (FC3)		
	ω_d (rad/s)	ζ (%)	ω_d (rad/s)	ζ (%)	MAC (%)
T-FA1	1.790	7.75	1.779	3.93	96
B3-F2	13.260	10.85	13.504	2.86	98.5
T-FA2	14.995	3.75	15.076	2.52	90

Table 6.5: FDD - Identified modal properties for FC3

Case FC4

In FC4 the wind speed is very high and the turbine operates inside the third region with constant rotational speed. The influence of the thrust force seems to be much larger than in the previous cases. This is deduced by looking in the stabilization diagram of Figure 6.8, where all the 6 selected peaks are gathered closed to nP regions. Still, the tower T-FA2 mode was stably identified, but the corresponding damping was relatively decreased compared to the exact values. A possible reason could be that the 12P coincides with the mode and could make the SDoF bell curve peakier. Additionally, the tower mode T-FA1 was identified by increasing the related MAC factor to 96%. Finally, all the blade modes around 9P are dominated by the harmonic.

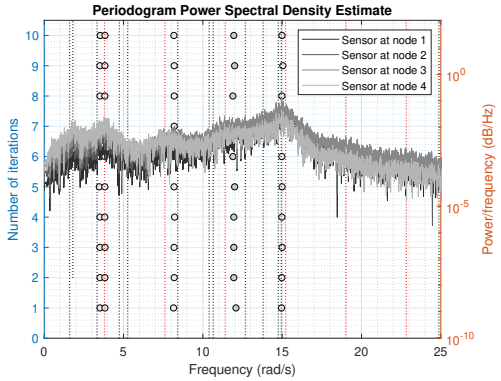

Figure 6.8: FDD - Stabilization diagram for FC4 and MAC = 95%

Mode	Exact (12.1rpm)		FDD (FC4)		
	ω_d (rad/s)	ζ (%)	ω_d (rad/s)	ζ (%)	MAC (%)
T-FA1	1.805	10.20	1.873	8.33	96
T-FA2	14.758	4.34	15.078	2.84	95

Table 6.6: FDD - Identified modal properties for FC4

Case FC5

FC5 is the last examined case of simulated data in FAST. In contrast to the previous identifications, here most of the modes were able to be identified in a stable way without changing the MAC factor. As it can be shown in Table 6.7, apart from the tower mode T-FA1, all the rest natural frequencies and the corresponding damping ratios are close to the exact values derived from FAST.

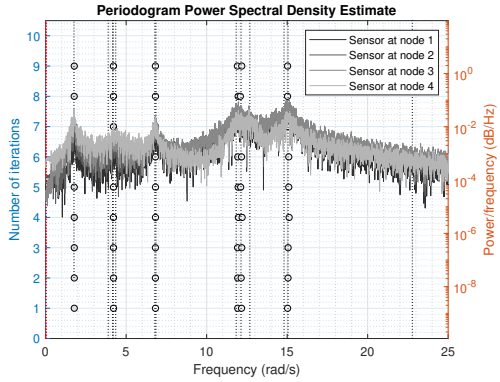

Figure 6.9: FDD - Stabilization diagram for FC5 and MAC = 95%

Mode	Exact (0rpm)		FDD (FC5)		
	ω_d (rad/s)	ζ (%)	ω_d (rad/s)	ζ (%)	MAC (%)
T-FA1	1.760	0.28	1.778	3.28	95
B2-F1	4.350	0.69	4.213	0.68	95
B2-E1	6.847	1.09	6.823	1.13	95
B2-F2	11.836	1.88	11.982	1.62	95
B1-F2	12.680	2.02	12.516	1.82	96
T-FA2	15.055	2.40	15.054	2.53	95

Table 6.7: FDD - Identified modal properties for FC5

6.3. CONCLUSIONS

In this chapter, FDD was applied in an iterative way on data derived from the examined simulated cases of the OWT in Matlab and FAST. Initially, the algorithm of FDD was applied on the ideal white noise input. The algorithm was able to derive good estimates of both the natural frequencies and the damping ratios. Additionally, the influence of an harmonic component close to a mode was examined, and it was concluded that the identification can become unstable for very closely spaced modes, or also shifted for an intermediate distance. Finally, an the same system was identified using simulated results considering environmental conditions. In that case, where the input spectra are a Kaimal and a JONSWAP spectrum for wind and wave, respectively, the first three modes were identified. Therefore, the influence of wave in the identification was rather minor.

As far as the identification of the operating OWT in FAST is concerned, FDD was able to derive the first tower bending mode by increasing the MAC factor. However, this option would also decrease the width of the SDoF bell curve and might affect the identification. Still, the derived damping values of mode T-FA1 are comparable with related identified values using ERA/NExT. Regarding the blade modes, FDD resulted in a very small number of stable blade modes. The main reason is that the influence of nP harmonics was dominant in a big part of the spectrum, and no clear peaks could be obtained. Moreover, most of the flapwise F2 bending modes were dominated by the presence of the second tower mode.

7

LEAST-SQUARES COMPLEX FREQUENCY-DOMAIN ESTIMATOR

The Least-Squares Complex Frequency-domain (LSCF) estimator is a curve-fitting technique that aims at identifying the modal properties of a system by fitting a rational fraction of two polynomials on each response auto/cross-Power Density Spectrum PSD. In this chapter, the theory behind LSCF will be presented and then the related algorithm will be applied on simulated data obtained from the OWT models in Matlab and FAST

7.1. THEORY BEHIND LSCF

The algorithm that will be presented in this chapter is the Least-Squares Complex Frequency-domain (LSCF) estimator, which is a simple and well-known frequency-domain estimator. This technique was introduced by P. Guillaume et al.[59] in 2001 and is more-or-less a curve fitting procedure that aims at obtaining the modal parameters of the system based only on the PSD of the output measurement data. As it will be shown later on, LSCF uses the discrete-time common-denominator model in order to extract the poles of the LTI system. Next, the natural frequencies and the damping ratios can be obtained from the real and the imaginary part of these poles.

It has to be mentioned that LSCF has been employed in many cases as the starting point of the Maximum Likelihood Estimation (MLE) method, which is an iterative frequency-domain estimator[60]. In that scheme, the main purpose of LSCF is to obtain initial values for MLE. The iterative nature of MLE is a way to deal with noise that is present in the measurement data, when the identification is done using output-only spectra.

However, several studies revealed that these initial values derived by LSCF already provided dynamic characteristics of high precision and minimal computational demand[61]. Therefore, one of the main advantages of this technique is that it is able to determine the modal properties with a low computational intensity, which allows to assess a large range of model orders efficiently. In that way, LSCF is able to obtain stabilization diagrams, even when applied to a large number of response data. Unfortunately, LSCF is referred not to be able to identify closely spaced modes. Instead, in such case LSCF leads into one single erroneous mode. Besides this disadvantage, in this chapter an attempt is made to apply LSCF on noisy output data.

Before explaining the algorithm behind this method, it is important to mention that in practice one may find the poly-reference version of LSCF method (pLSCF), which is also commercially known as PolyMAX method[12][61][13]. This technique is based on the so-called right matrix-fraction model instead of the common-denominator model and aims at dealing with the problem of closely spaced modes.

LSCF starts with the assumptions that the structure of interest can be approximated by an LTI system, and that the ambient excitation is supposed to be a broadband white noise stochastic process. Under these conditions, as explained in Section 6.1, Eq.7.1 is valid.

$$\mathbf{S}_{xx}(\omega) = \mathbf{H}(\omega)\,\mathbf{C}\mathbf{H}^{H}(\omega) \propto \mathbf{H}(\omega)\,\mathbf{H}^{H}(\omega) \tag{7.1}$$

where, $\mathbf{S}_{xx} \in \mathbb{C}^{mxm}$ is a matrix that contains auto/cross-PSD of the measured output responses, $\mathbf{H} \in \mathbb{C}^{mxr}$ is the FRF, $(\bullet)^{H}$ denotes the Hemitian (conjugate transpose) of a matrix and $\mathbf{C}$ is a constant matrix proportional to the identity matrix, representing the PSD of the broadband white noise stochastic system input. In this algorithm, the FRF will be expressed using a common-denominator model. In that case, each element of the

FRF matrix is represented by a rational fraction of two polynomials $a(\omega)$ and $b_{ij}(\omega)$. This formulation can be obtained by reformulating the definition of the FRF function. Eq.7.2 shows this definition together with the polynomial expression of the FRF.

$$\mathbf{H}(\omega) = \sum_{k=1}^{n} \frac{\mathbf{R}_k}{\omega - \lambda_k} + \frac{\bar{\mathbf{R}}_k}{\omega - \bar{\lambda}_k} = \frac{\begin{bmatrix} b_{11}(\omega) & \cdots & b_{1r}(\omega) \\ \vdots & \ddots & \vdots \\ b_{m1}(\omega) & \cdots & b_{mr}(\omega) \end{bmatrix}}{d(\omega)} = \frac{\mathbf{B}(\omega)}{d(\omega)} \tag{7.2}$$

According to that expression the poles of the FRF will also be the roots of the denominator polynomial $d(\omega)$. By substituting Eq.7.2 into Eq.7.1, it can be shown that the auto/cross-PSD matrix has similar modal decomposition as the FRF matrix (see Eq.6.7). Therefore, it is reasonable to expect that the roots of polynomial $d(\omega)$ will be the poles of the system.

$$\mathbf{S}_{xx}(\omega) = \frac{\begin{bmatrix} N_{11}(\omega) & \cdots & N_{1m}(\omega) \\ \vdots & \ddots & \vdots \\ N_{m1}(\omega) & \cdots & N_{mm}(\omega) \end{bmatrix}}{d(\omega)} = \frac{\mathbf{N}(\omega)}{d(\omega)} \tag{7.3}$$

Starting from this expression, LSCF estimator will determine these polynomials that will represent $\mathbf{S}_{xx}$ by fitting curves in a least squares sense. In the following part, the mathematical procedure that is followed in order to calculate these unknown polynomial functions will be described.

Determination of the unknown polynomial functions

The curve-fitting procedure will be applied on each separate element of $\mathbf{S}_{xx}$ matrix regardless of the way they are sorted[59][12][62]. The common-denominator mathematical model that will be used here is named as $S_k \in \mathbb{C}$ and models each element of matrix $\mathbf{S}_{xx}$, for $k = 1, \ldots, mm$. Therefore, each element k from the PSD matrix can be expressed based on Eq.7.4.

$$S_k(\omega) = \frac{N_k(\omega)}{d(\omega)} \tag{7.4}$$

where the numerator and the common-denominator polynomials will be expressed by following two relations.

$$\begin{aligned} N_k(\omega) &= \sum_{j=0}^{n} \Omega_j(\omega) B_{kj} \\ d(\omega) &= \sum_{j=0}^{n} \Omega_j(\omega) A_j \end{aligned} \tag{7.5}$$

In this equation, the first term $\Omega_j \in \mathbb{C}$ is the polynomial basis function and terms B_{kj} and $A_j \in \mathbb{R}$ are the unknown real parameters that need to be estimated. Also, $j = 0, \ldots, n$ are the exponents of the polynomial that will be used, starting from zero for the constant term of the polynomial and n is the order of the polynomial. It is assumed here that both the nominator and the denominator have the same order.

Since both the numerator and the denominator polynomials are expressed in the z-domain, selecting a discrete-time (or z-domain) polynomial basis function Ω_j will have several advantages over a continuous time model. More in detail, in discrete-time dynamic problems a common choice is to use the exponential expression of Eq.7.6. This expression will yield a better numerical conditioned estimation problem due to the fact that the exponential can be expressed by Sin and Cos functions, which at different frequencies are mathematically orthogonal.

$$\Omega_j(\omega) = e^{(-i\omega\Delta t)j} \tag{7.6}$$

where Δt is the sampling time. The main target of this curve-fitting procedure is to identify the unknown parameters A_j that correspond to all the exponents. The common denominator terms A_j and the nominator

terms for each component k of the PSD approximation $B_k j$ will be collected into a single unknown column vector $\boldsymbol{\theta}$.

$$\boldsymbol{\theta} = \begin{Bmatrix} \boldsymbol{\beta}_1 \\ \boldsymbol{\beta}_2 \\ \vdots \\ \boldsymbol{\beta}_{mm} \\ \boldsymbol{\alpha} \end{Bmatrix}, \ \boldsymbol{\beta}_k = \begin{Bmatrix} B_{k0} \\ B_{k1} \\ \vdots \\ B_{kn} \end{Bmatrix}, \ \boldsymbol{a} = \begin{Bmatrix} A_0 \\ A_1 \\ \vdots \\ A_n \end{Bmatrix} \tag{7.7}$$

where $\boldsymbol{\theta} \in \mathbb{R}^{(n+1)(mm+1)x1}$. Then, the identification problem is solved by minimizing the cost function for a discrete frequency vector ω_f $(f = 1,\ldots,N_f)$, which is shown in Eq.7.8.

$$l_{LS}(\boldsymbol{\theta}) = \sum_{k=1}^{mm} \sum_{f=1}^{N_f} \left|\varepsilon_k(\omega_f,\boldsymbol{\theta})\right|^2 \tag{7.8}$$

where the least squares (LS) equation error, $\varepsilon_k(\omega_f,\boldsymbol{\theta})$ is defined as described by Eq.7.9. This error can be interpreted as the difference between the PSD element k multiplied with the unknown modelled denominator, and the unknown modelled nominator of this PSD element k. In that sense, by minimizing this error, the measured and the modelled k^{th} element of the PSD will coincide.

$$\varepsilon_k(\omega_f,\boldsymbol{\theta}) = S_k(\omega_f)\, d(\omega_f,\boldsymbol{\theta}) - N_k(\omega_f,\boldsymbol{\theta}) \tag{7.9}$$

As referred in [59][12][62], due to the fact that this error equation is linear in the parameters and also because a common-denominator model is used, the error can be formulated in matrix notations as expressed by Eq.7.10.

$$\varepsilon_k(\omega_f,\boldsymbol{\theta}) = \begin{bmatrix} \mathbf{X}_k & \mathbf{Y}_k \end{bmatrix} \begin{bmatrix} \boldsymbol{\beta}_k \\ \boldsymbol{\alpha} \end{bmatrix} \tag{7.10}$$

Hence, the minimization of the error is equivalent to the expression of Eq.7.11.

$$\begin{Bmatrix} \varepsilon_1(\omega_f,\theta) \\ \varepsilon_2(\omega_f,\theta) \\ \vdots \\ \varepsilon_k(\omega_f,\theta) \end{Bmatrix} = \begin{bmatrix} \mathbf{X}_1 & 0 & \cdots & 0 & \mathbf{Y}_1 \\ 0 & \mathbf{X}_2 & & 0 & \mathbf{Y}_2 \\ \vdots & & \ddots & & \vdots \\ 0 & 0 & & \mathbf{X}_{mm} & \mathbf{Y}_{mm} \end{bmatrix} \begin{Bmatrix} \boldsymbol{\beta}_1 \\ \boldsymbol{\beta}_2 \\ \vdots \\ \boldsymbol{\beta}_{mm} \\ \boldsymbol{\alpha} \end{Bmatrix} = \boldsymbol{J\theta} \approx 0 \tag{7.11}$$

where, each block $\mathbf{X}_k$ and $\mathbf{Y}_k \in \mathbb{C}^{N_f x(n+1)}$ and $\mathbf{J} \in \mathbb{C}^{(mmN_f)x((mm+1)(n+1)}$ is the Jacobian matrix of this least-squares problem. These vectors $\mathbf{X}_k$ and $\mathbf{Y}_k$ can be calculated using the known PSD data S_k and also the polynomial basis function Ω_j as described in Eq.7.12.

$$\begin{aligned} \mathbf{X}_k &= \begin{bmatrix} \Omega_0(\omega_1) & \cdots & \Omega_n(\omega_1) \\ \vdots & & \vdots \\ \Omega_0\left(\omega_{N_f}\right) & \cdots & \Omega_n\left(\omega_{N_f}\right) \end{bmatrix} \\ \mathbf{Y}_k &= \begin{bmatrix} -\Omega_0(\omega_1)\, S_k(\omega_1) & \cdots & -\Omega_n(\omega_1)\, S_k(\omega_1) \\ \vdots & & \vdots \\ -\Omega_0\left(\omega_{N_f}\right) S_k\left(\omega_{N_f}\right) & \cdots & -\Omega_n\left(\omega_{N_f}\right) S_k\left(\omega_{N_f}\right) \end{bmatrix} \end{aligned} \tag{7.12}$$

By pre-multiplying Eq.7.11 with the Hermitian transpose of the Jacobean matrix, $\mathbf{J}^H$, the minimization of the equation error, $\boldsymbol{\varepsilon}(\omega_f,\boldsymbol{\theta})$ is equivalent to the expression of Eq.7.13. As described in [59], this step leads to a better conditioned problem and speeds up the method.

$$\boldsymbol{J^H J\theta} = \begin{bmatrix} \mathbf{R}_1 & 0 & \cdots & \bar{\mathbf{S}}_1 \\ 0 & \mathbf{R}_2 & & \bar{\mathbf{S}}_2 \\ \vdots & & \ddots & \vdots \\ \bar{\mathbf{S}}_1^H & \bar{\mathbf{S}}_2^H & \cdots & \sum_{k=1}^{mm} \mathbf{T}_k \end{bmatrix} \begin{Bmatrix} \boldsymbol{\beta}_1 \\ \boldsymbol{\beta}_2 \\ \vdots \\ \boldsymbol{\beta}_{mm} \\ \boldsymbol{\alpha} \end{Bmatrix} \approx 0 \tag{7.13}$$

with $\mathbf{R}_k = Re\left(\mathbf{X}_k^H \mathbf{X}_k\right)$, $\bar{\mathbf{S}}_k = Re\left(\mathbf{X}_k^H \mathbf{Y}_k\right)$ and $\mathbf{T}_k = Re\left(\mathbf{Y}_k^H \mathbf{Y}_k\right)$ real, square $(n+1)x(n+1)$ matrices. Solving Eq.7.13 for the unknown parameter vector results in the two expressions of Eq.7.14.

$$\begin{aligned} \boldsymbol{\beta}_k &= -\mathbf{R}_k^{-1} \bar{\mathbf{S}}_k \boldsymbol{\alpha} \\ \sum_{k=1}^{mm} \left(\mathbf{T}_k - \bar{\mathbf{S}}_k^H \mathbf{R}_k^{-1} \bar{\mathbf{S}}_k\right) \boldsymbol{\alpha} &= \mathbf{M}\boldsymbol{\alpha} \approx \mathbf{0} \end{aligned} \tag{7.14}$$

where, $\mathbf{M} \in \mathbb{R}^{(n+1)x(n+1)}$. In order to solve for $\boldsymbol{\alpha}$ and avoid the trivial solution $\boldsymbol{\alpha} = \mathbf{0}$, the last element of $\boldsymbol{\alpha}$, A_n is assumed to be constant and equal to 1. Using this constraint, the rest n elements of $\boldsymbol{\alpha}$ can be calculated in a least-squares sense.

$$\boldsymbol{\alpha}_{LS} = \left\{ \begin{array}{c} -\mathbf{M}(1:n, 1:n)^{-1} \mathbf{M}(1:n, 1+n) \\ 1 \end{array} \right\} \tag{7.15}$$

Apart from the solving Eq.7.15 using least squares, several other approaches are also available in literature[63] [64][65][66]. Solvers like Total Least Squares (TLS), Bootstrapped Total Least Squares (BTLS) and Weighted Generalized Total Least-Squares implementation (GTLS) are some of the most popular frequency domain estimators. In short, the procedure behind LSCF follows the steps below.

To conclude, this procedure resulted in the real unknown parameters of the k nominator polynomials and the common-denominator polynomial. Using these values, the PSD matrix can be modelled and based on the theoretical expression of Eq.4.1, the modal properties of the system can be obtained from the roots of the denominator.

Step - 1 PSD matrices

In the first step, the auto/cross-PSD matrix $\mathbf{S}_{xx} \in \mathbb{C}^{mxm}$ is determined from the discrete-time output response time-series using the Welch's averaged, modified periodogram method[67]. This method is one of the most widely used approaches in the calculation of PSD functions, and is an already incorporated Matlab function (*e.g.* `pwelch`).

In this approach, the time-series are divide into overlapping segments of a certain length using a given overlapping percentage $\in$(0%,100%). In the second step, a window is applied in time-domain at each sub-record, considering a Hamming window of length equal to the length of the segments. Other types of windows can also be used, but Hamming window combines both good resolution and small amplitude of side-lobes when inverted into frequency domain. Then Fast Fourier Transform (FFT) is used to convert the windowed sub-records into frequency domain. In the end the response spectra that correspond to the k^{th} sections from two different response data i and j, `i.e.` $X_{i,k}(\omega)$ and $X_{j,k}(\omega)$ will be used to obtain the PSDs as shown in Eq.7.16.

$$S_{x_i x_j}(\omega) = \frac{1}{n_f} \sum_{k=1}^{n} X_{i,k}(\omega)\, X_{j,k}^H(\omega) \tag{7.16}$$

where, n_f is the length of the time-series, and n is the number of sections. One may observe that PSDs obtained from Eq.7.16 provide an averaged estimate. In case of noisy time-series, this would lead into smoother spectra.

Step - 2 Determine polynomial basis function $\Omega_j(\omega)$

The next step is to determine the polynomial basis function $\Omega_j(\omega)$ that will be used. As mentioned before, for discrete-time dynamic problems the exponential expression of Eq.7.6 can be used. This function will be calculated for each exponent $j = 0, \ldots, n$, where n is the order of the polynomial of both the nominator and the denominator.

Step - 3 Determine matrices $\boldsymbol{X}_k$, $\boldsymbol{Y}_k$, $\boldsymbol{R}_k$, $\bar{\boldsymbol{S}}_k$ and $\boldsymbol{T}_k$

After the calculation of $\Omega_j(\omega)$, the vectors $\mathbf{X}_k$ and $\mathbf{Y}_k$ can be calculated as a function of the polynomial basis function and the PSD matrices (Eq.7.12). After the matrices $\mathbf{X}_k$ and $\mathbf{Y}_k$ are calculated, the reduced real matrices $\mathbf{R}_k = Re\left(\mathbf{X}_k^H \mathbf{X}_k\right)$, $\bar{\mathbf{S}}_k = Re\left(\mathbf{X}_k^H \mathbf{Y}_k\right)$ and $\mathbf{T}_k = Re\left(\mathbf{Y}_k^H \mathbf{Y}_k\right)$ are obtained.

Step - 4 Find the unknown parameters $\boldsymbol{\theta}$

In the last step, matrix $\mathbf{M}$ is calculated using the three aforementioned matrices (see Eq.7.14). Then, the least squares solution of the unknown common-denominator coefficients can be calculated from Eq.7.15.

Finally, unknown nominator polynomials can be obtained by calculating $\boldsymbol{\beta}_k$ as explained in Eq.7.14, where $\boldsymbol{\alpha} = \boldsymbol{\alpha}_{LS}$. These polynomials are the main output from this curve-fitting procedure. Finally, for visualization, these coefficient $\boldsymbol{\theta}$ can be used together with the polynomial basis function $\Omega_j(\omega)$ to derive the fitted curves as described by Eq.7.5.

Step - 5 Modal properties

Finally, the roots of the common-denominator are the poles λ_i of the system and may be used to calculate the natural frequencies and damping ratio of the system as explained in Eq.4.11 and Eq.4.12.

This whole procedure is very fast and can be applied in an iterative way for $n = 1, \ldots, n_{max}$. Therefore, by plotting the identified natural frequencies with respect to the order of the polynomial, a stabilization diagram is calculated to visualize the stable modes.

7.2. NUMERICAL RESULTS

The LSCF algorithm will be applied on the response data obtained from the numerical models introduced in Chapter 3. In the upcoming part, first, the modal properties of the OWT in Matlab will be derived for white noise input and then for ambient excitation. This is done in order to validate the algorithm and describe how LSCF will be applied. After this, the first mode of the system will be identified based on responses that correspond to white noise combined with harmonic input. In that way, the robustness against external harmonics will be checked. In the end, LSCF will be used to estimate the dynamic characteristics of the operating OWT in FAST. This is actually the greatest challenge, since both the white noise and the LTI assumptions are violated.

7.2.1. SIMULATED RESPONSES USING MATLAB MODEL

LSCF for white noise input

As described by the theory presented in Section 7.1, LSCF is a curve-fitting technique aims at identifying the poles of noisy auto/cross PSDs by fitting a common-denominator model. In order to deal with the noise, the Welch's method will be employed to smooth out the high frequent part of the noise that is present in the spectra. Once these fluctuations are removed, the main trend of the spectra will be highlighted. A Hamming window of length equal to 1/10 the length of the spectra with 50% overlapping will be used. Keep in mind that the time-series have been also corrupted using measurement noise with SNR equal to 50. Figure 7.1 shows the amplitudes of three elements from the smoothed matrix $\mathbf{S}_{xx} \in \mathbb{C}^{mxm}$. As it can be shown, the fitted curve for the highest order (50) is very close to the power spectra, but tries to fit and model also the noise that still remains in the spectra.

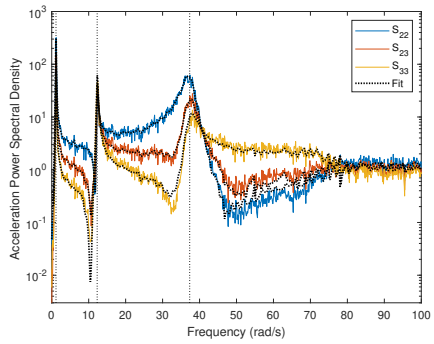

Figure 7.1: Original and fitted PSDs using LSCF

The poles of the fitted spectra will result in the modal properties of the system, and by iterating over the polynomial order, a stabilization diagram can be generated. One of the main problems that came out in the LSCF

algorithm is the large amount of non-structural modes in the stabilization diagrams. Given the low computational time of constructing one stabilization diagram using LSCF, the procedure that has been followed here, in order to remove as many as possible non-structural modes, suggests the construction of multiple diagrams. The resulting final diagram will include only the modes that are present in all the diagrams (stable modes). The modes that were kept in the final stabilization diagram are those that have a difference of natural frequency and damping ratio lower than 1rad/s and 2%, respectively. It was found out that applying LSCF on the full frequency band of the auto/cross PSD resulted in modes spread over the whole frequency range (200rad/s). In case where part of the PSDs at high frequencies is truncated, these non-structural modes that are related to the presence of noise shift. Therefore, by truncating different part from the high frequencies, the non-structural modes will be different, but the structural modes will remain the same. Figure 7.2 was generated after comparing the identified modes between two stabilization diagrams for a truncation at 100rad/s and 110rad/s. Then, the modes between the two spectra that have a difference of frequencies and damping ratio lower than 1rad/s and 2%, respectively are kept in the final stabilization diagram, while the rest are filtered out.

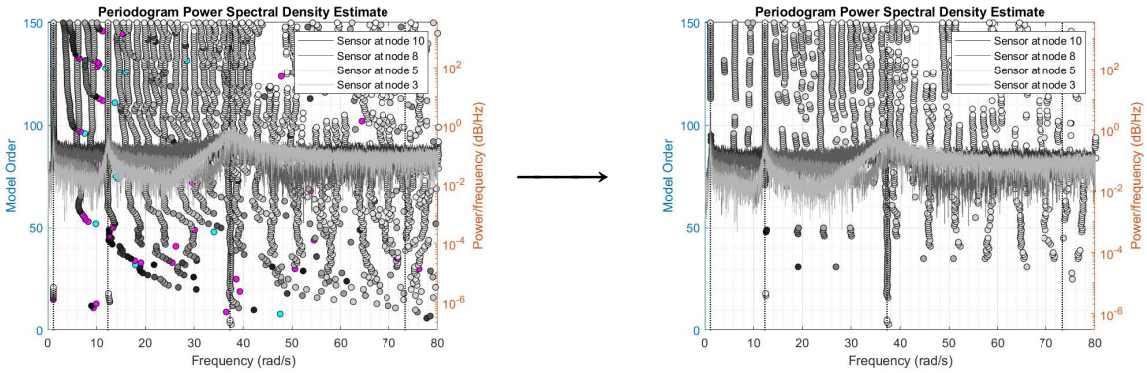

Figure 7.2: Stabilization diagram of initial identification (left) and merged modes from multiple identifications (right) – LSCF on white noise input

As it can be shown, this simple procedure resulted in a quite more clear stabilization diagram, but still too noisy with respect to the related diagrams of the aforementioned OMA algorithms. One may recognize the modes of the system by relating the identified modes with the peaks of the response PSDs. The main reason of these non-structural modes is that the curve for larger orders becomes less smooth and tries to model also the noisy parts of the PSDs. This cannot be avoided by more intense smoothing (smaller window length), since after a point, the smoothing procedure will affect the shape of the PSDs by moving and storing energy from a peak to neighbouring frequencies. This might lead in shifting and/or widening the peak.

Based on the stabilization diagram, the modes that corresponded to the peaks of the response PSDs can be shown in Table 7.1. The identified modes are very close to the exact values and verify the algorithm. Unfortunately, the first mode was identified when the order of the polynomial increased over 110. Still, this approach seems promising in the system identification thanks to the small deviations from the exact modal properties.

Mode	Exact		LSCF (white noise)	
	ω_d (rad/s)	ζ (%)	ω_d (rad/s)	ζ (%)
1	1.155	4.00	1.155	4.00
2	12.303	2.00	12.325	1.91
3	37.305	5.09	37.315	5.15

Table 7.1: Identified and exact modal properties - LSCF for white noise input

LSCF for white noise and harmonic input

In this paragraph the LSCF algorithm will be used on data, which has been generated with white noise input, together with harmonic components at frequencies close to the first natural frequency. The considered frequencies of the harmonic input loading are 1.31rad/s, 1.45rad/s and 1.76rad/s. Figure 7.3 shows the stabilization diagram for these three cases. As it can be shown, the harmonic influences the identification

results. The identified natural frequency shifts towards the frequency of the input load. Particularly, when the harmonic moves away from the natural frequency, this shift is larger until the influence of the harmonic is not significant. This has to do probably with the fact that the PSDs are smoothed, and this peak is not that sharp in the PSDs. However, this energy is still saved at the neighbouring frequencies, and leads to this shift of the identified modes. In case where the external harmonic component is far away from the natural frequency, it can be shown that the mode becomes stable after several iterations, which still correspond to order (~180) larger than the order (~110) for the case of pure white noise input.

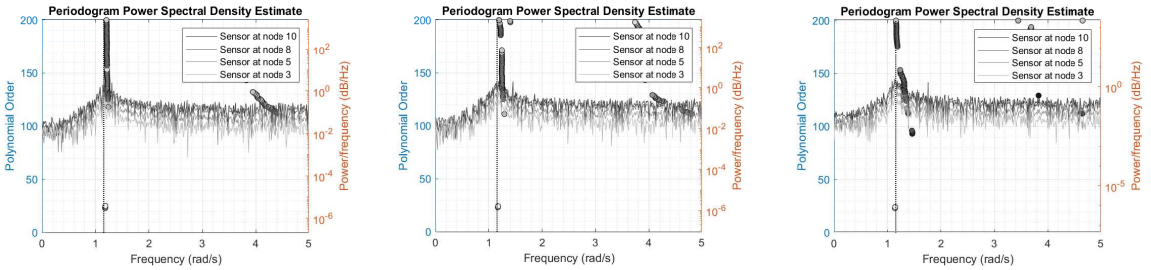

Figure 7.3: Stabilization diagram, zoomed at the fundamental natural frequency – LSCF for white noise and harmonic input

LSCF for wind, wave and current excitation

The case where the system is also loaded by wind, wave and current will be examined here. The algorithm of LSCF will be applied in the same way as in the case of white noise input. As it can be shown in Figure 7.4, the identification is not affected by the presence of wave loading. Actually, no mode was identified at frequencies lower than the first natural frequency of the system, where all wave energy lies.

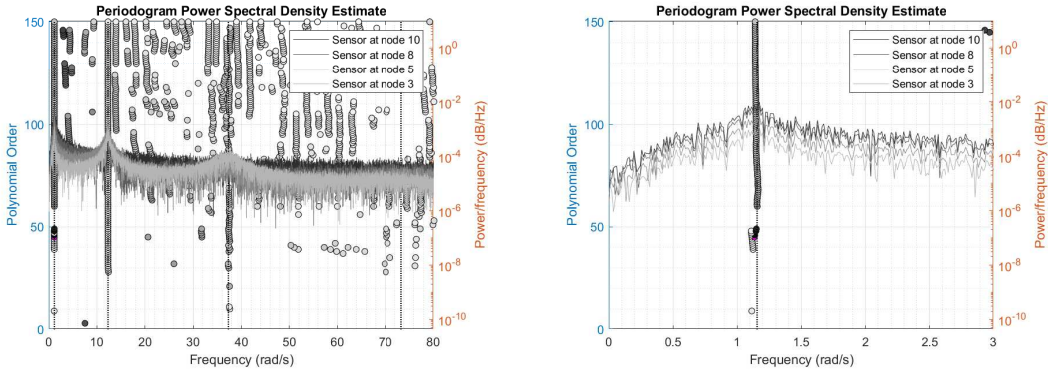

Figure 7.4: Stabilization diagram – LSCF for wind, wave and current input

The resulting modal properties can be shown in Table 7.2. The identification leads us to the conclusion that the external loading did not result in stable non-structural identified mode. It is unclear whether the first mode is influenced by the presence of the wave. The same observation as in all the previous algorithms hold also here, since the natural frequency of the first mode is shifted towards lower frequencies, and the modal damping ratio is overestimated.

Mode	**Exact**		**LSCF (env.cond.)**	
	ω_d (rad/s)	ζ (%)	ω_d (rad/s)	ζ (%)
1	1.155	4.00	1.140	6.07
2	12.303	2.00	12.312	2.37
3	37.305	5.09	37.517	5.70

Table 7.2: Identified and exact modal properties - LSCF for wind, wave and current excitation

7.2.2. SIMULATED RESPONSES USING MODEL IN FAST

In the previous section, the LSCF algorithm was applied on the OWT model in Matlab, loaded by white noise input. Due to the increased number of identified modes, differentiating between the structural and the non-structural modes is based on the engineers judgement. Here, this algorithm will be applied on the response PSD matrix from the accelerations obtained from the model in FAST.

More in detail, the time-series obtained from each of the loading cases of Section 2.2 are initially corrupted with measurement noise of SNR equal to 50. For all the simulated data from FAST, the whole modal content is present at frequencies lower than 25rad/s. However, the maximum frequency of the response PSDs is 200rad/s, which means that the PSDs are much wider than they need to be for the identification. Hence, this range above 25rad/s does not contain any modal information and could be truncated. The approach described in Section 7.2.1 will also be used here to derive quite clearer stabilization diagrams. In particular, the first identification will be applied on PSDs truncated at 30rad/s and the second at 40rad/s. The stable modes will be present at both these diagrams, while the part of the non-structural will be shifted. Then, by keeping only the modes that have a difference of natural frequencies lower than 1rad/s and a difference of damping ratio lower than 2%, a filtered stabilization diagram can be obtained.

Case FC1

LSCF was initially applied on the accelerations derived from FC1. The first observation is that the stabilization diagram is still very noisy. However, one may recognize an identified mode at first by the peaks in the response spectra and then by the identified modes at low polynomial orders, which stabilize for larger orders. All the identified stable modes were collected in Table 7.3. As it can be shown, both the two tower modes were identified. However, the related damping ratio was quite lower than the exact values. Additionally, LSCF resulted in six blade modes. When looking in the flapwise modes one may observe that the damping ratios are largely underestimated. One possible reason is that they are close to 3P and 6P. Therefore, the presence of the harmonic excitation will change the shape of the response spectra close to the blade mode and will make it peakier. Apart from that, the damping ratios of the rest edgewise modes were identified in a better accuracy.

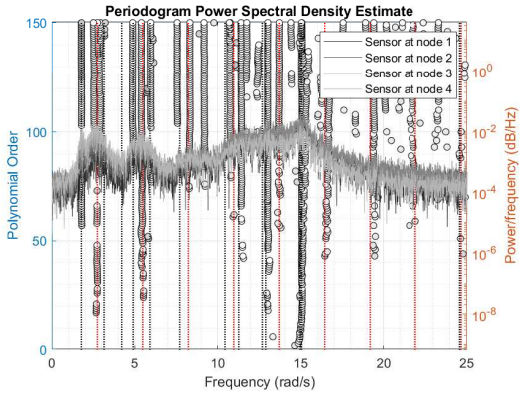

Figure 7.5: LSCF - Stabilization diagram for FC1

Mode	Exact (8.5rpm)		LSCF (FC1)	
	ω_d (rad/s)	ζ (%)	ω_d (rad/s)	ζ (%)
T-FA1	1.780	6.15	1.779	5.21
B3-F1	3.145	47.45	3.224	4.94
B2-F1	4.900	32.85	4.885	0.56
B3-E1	5.910	1.10	5.971	1.43
B2-E1	7.705	0.85	7.553	0.61
B2-F2	11.260	10.80	11.298	2.90
B3-F2	12.895	9.05	13.019	0.97
T-FA2	15.040	2.85	15.080	1.82

Table 7.3: LSCF - Identified modal properties for FC1

Case FC2

Figure 7.6 shows the results from the identification of FC2 examined case. The number of the non-structural modes is very high and can be attributed to minor peaks that the fitted curve makes at specific locations due to noise. Keep in mind that LSCF tries to find a curve that describes the noisy data as good as possible. Other techniques may fit smoother curves, without including noise when modelling (*e.g* MLE). Still, for the present case with the noisy stabilization diagrams, several modes have been stably identified. At first, both tower modes were identified with a corresponding good estimation of damping ratio. Additionally, three blade modes have been identified with poor damping precision.

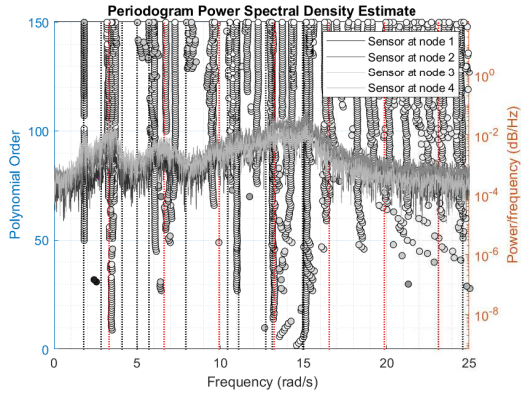

Figure 7.6: LSCF - Stabilization diagram for FC2

Mode	Exact (10.5rpm)		LSCF (FC2)	
	ω_d (rad/s)	ζ (%)	ω_d (rad/s)	ζ (%)
T-FA1	1.785	7.30	1.812	7.22
B3-E1	5.710	1.20	5.725	4.55
B2-F2	11.105	13.60	10.998	0.75
B3-F2	13.120	10.45	13.107	2.03
T-FA2	15.015	3.45	15.285	1.27

Table 7.4: LSCF - Identified modal properties for FC2

Case FC3

Applying LSCF on the responses of the third operating load case resulted in a decreased number of modes. Additionally, most of the modes are attracted by the presence of nP. The only blade mode that was identified was also close to a very noisy region, which increases the possibilities of obtaining erroneous damping.

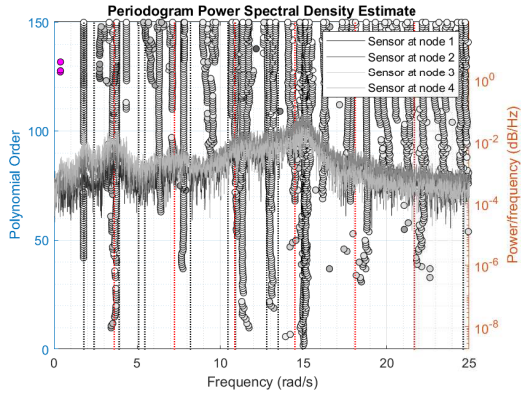

Figure 7.7: LSCF - Stabilization diagram for FC3

Mode	Exact (10.5rpm)		LSCF (FC3)	
	ω_d (rad/s)	ζ (%)	ω_d (rad/s)	ζ (%)
T-FA1	1.790	7.75	1.787	4.93
B1-F2	12.760	12.45	12.900	0.28
T-FA2	14.995	3.75	15.150	1.48

Table 7.5: LSCF - Identified modal properties for FC3

Case FC4

FC4 corresponds to very high wind speeds and strong harmonic excitation that dominate most of the response spectrum. This can be observed from Figure 7.8 and by the fact that most of the identified modes are gathered around the nP regions. As shown in Table 7.6, all the estimated damping ratios are underestimated both for the tower modes and the blade modes.

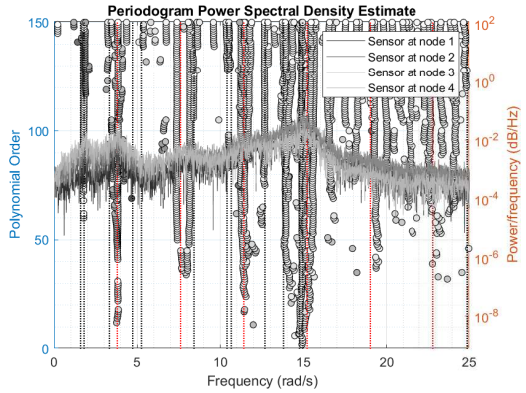

Figure 7.8: LSCF - Stabilization diagram for FC4

Mode	Exact (12.1rpm)		LSCF (FC4)	
	ω_d (rad/s)	ζ (%)	ω_d (rad/s)	ζ (%)
T-FA1	1.805	10.20	1.792	4.72
B2-E1	8.416	0.90	8.597	1.27
B1-F2	12.681	17.47	12.647	2.70
B3-F2	13.798	15.36	13.735	0.12
T-FA2	14.758	4.34	14.942	2.21

Table 7.6: LSCF - Identified modal properties for FC4

Case FC5

FC5 corresponds to parked turbine and no *n*P are present in the responses. This identification resulted in the highest number of modes, with also very good damping estimations except for the mode close to the first flapwise modes (Bx−F1), which was largely increased.

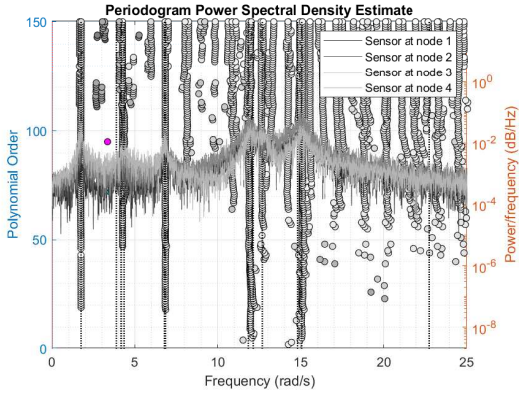

Figure 7.9: LSCF - Stabilization diagram for FC5

Mode	Exact (0rpm)		LSCF (FC5)	
	ω_d (rad/s)	ζ (%)	ω_d (rad/s)	ζ (%)
T-FA1	1.760	0.28	1.764	3.47
B1-F1	4.164	0.66	4.061	6.55
B3-F1	4.187	0.67		
B2-F1	4.350	0.69		
B2-E1	6.847	1.09	6.830	1.14
B2-F2	11.836	1.88	11.882	1.99
B3-F2	12.134	1.93	12.011	1.72
B1-F2	12.680	2.02	12.516	1.82
T-FA2	15.055	2.40	15.094	2.23

Table 7.7: LSCF - Identified modal properties for FC5

7.3. CONCLUSIONS

LSCF was applied for the identification of the two OWT models giving very dense stabilization diagrams, able to derive a large number of stable modes. In the application on the model in Matlab, it was figured out that in order to identify the first mode, a very large number of polynomial order was needed (>110). This happens due to the resolution of the spectrum. More in detail, when LSCF fits a curve on a relatively sharp peak with low resolution (*e.g.* first mode of model in Matlab), the fitted curve will initially (low orders) put a single peak that resembles a mode of almost zero damping (very rapid amplification at resonance). This is the reason why LSCF was applied at such high orders. It was found out that this technique is able to obtain an accurate estimation of the modal properties of the OWT system in Matlab. Briefly, LSCF was affected by the external harmonic component, especially when it was close to the natural frequency. The influence of the harmonic was mitigated by the smoothing procedure and no mode was identified at the frequencies of the harmonics.

In the second part of the numerical application, the data from FAST were used as inputs to the code. In all the cases the algorithm was able to identify both the tower modes. Additionally, the large values of damping ratio for the first fore-aft tower bending mode and the blades seem to be highly underestimated for most of the operating cases. In general the damping estimation was better for the edgewise modes which is limited at values lower than 10%. Finally, several identified modes were engaged to damping ratios much lower than 0.5%. For these cases damping may be affected by the aforementioned behaviour of the LSCF algorithm, where a peak is modelled by a very small number of spectral values.

8

TRANSMISSIBILITY-BASED OPERATIONAL MODAL ANALYSIS

Transmissibility-based Operational Modal Analysis (TOMA) introduced an innovative idea in OMA system identification. This technique aims at raising the influence of the type of the input in the identification of the modal parameters. In that way, non-structural modes related to the input spectrum are no more present in the identification. Still, several assumptions have been made. In this chapter the basic idea behind TOMA is initially presented and then the algorithm will be applied on simulated responses from the OWT models in Matlab and FAST

8.1. THEORY BEHIND TOMA

The idea of using a transmissibility function as a way to describe a relation between FRFs of a dynamic system has been investigated for decades in both numerical[68] and experimental[69] studies. Back in 1998, A. Ribeiro proposed a generalization of the concept of transmissibility matrix and introduced some important properties of it[70][71]. As stated in his works, both the FRFs and the transmissibility matrix are properties of the system. Despite this fact, it is important to keep in mind that the latter is also related to the location and the number of the applied external forces. Additionally, A. Ribeiro showed that the transmissibility matrix derived from a set of harmonic and a set of random excitation applied at the same locations, are identical to each other. In that way, he concluded that the transmissibility matrix is independent of the type of the applied forces. In short, as the FRF connects the input forces to the output responses, the transmissibility matrix relates the known /input responses to unknown/output responses.

This property has found many applications in the field of damage detection. However, the real breakthrough in applying transmissibilities in the field of OMA system identification came later in 2006, when Devriendt et al. proposed a scheme that included transmissibilities for the identification of modal parameters [72]. This was the first step towards the Transmissibility-based Operational Modal Analysis (TOMA)[73][29][30][74][75], which aims at identifying a system without making any assumption about the type of the input. In that way, this method reduces the danger of identifying non-structural modes, when the input includes significant harmonic components. Since then, Devriendt et al. did quiet extensive research on obtaining transmissibilities from outputs, which are totally independent of the input spectral content. In that sense, they focused on deriving transmissibilities of deterministic (non-stochastic) nature. This was essential in the identification of a system loaded by any type of external loads. Two other techniques that where proposed by Devriendt et al. are referred to as Poly-reference Transmissibility-based Operational Modal Analysis (pTOMA)[32][33][76] and Time Varying Transmissibility-based Operational Modal Analysis (Tv-TOMA)[34][35][77]. These two approaches aim at raising several shortcomings of TOMA, but also aim at automating the identification. More details will be explained while explaining TOMA.

At first, TOMA starts by obtaining the transmissibilities based on the response data $X(\omega)$. This implies the assumption that the structure of interest is an LTI system, as the expression $X(\omega) = H(\omega)F(\omega)$ will be employed. The first goal when applying TOMA is to obtain transmissibilities that are independent of the external loading spectra. The scalar transmissibility is calculated by taking the ratio of two response spectra i and j, as shown in Eq.8.1.

$$T_{ij}(\omega) = \frac{X_i(\omega)}{X_j(\omega)} = \frac{\sum_{k=1}^{r} H_{ik}(\omega) F_k(\omega)}{\sum_{k=1}^{r} H_{jk}(\omega) F_k(\omega)} \tag{8.1}$$

where, $X_i, X_j \in \mathbb{C}$ are two output response spectra, $F_k \in \mathbb{C}$ is the spectrum of external forces at DoF $k = 1, \ldots, r$ and $H_{ik}, H_{jk} \in \mathbb{C}$ are the related elements of the FRF that connects the input applied at the DoF k to a given response spectrum i, j.

As it can be deduced, in cases where the input consist of more than one uncorrelated forces, applied at different locations along the system, then the input spectrum is not simplified and, thus, scalar transmissibility is not deterministic anymore. Keep in mind that pTOMA has been developed to tackle that issue. This is done by using the multivariable transmissibility matrix instead of the scalar expression of Eq.8.1, and by also considering as many output reference spectra as the number of the uncorrelated external forces[33]. Coming back to TOMA, for the ideal cases where the external loading is consisted of a single input, or multiple fully correlated inputs, the scalar transmissibility will be deterministic. In other words, under these two conditions the spectrum of the eternal loading will be simplified. Hence, for a single input the transmissibility will be

$$T_{ij}(\omega) = \frac{X_i(\omega)}{X_j(\omega)} = \frac{H_{ik}(\omega) F_k(\omega)}{H_{jk}(\omega) F_k(\omega)} = \frac{H_{ik}(\omega)}{H_{jk}(\omega)} \tag{8.2}$$

and for multiple, fully correlated inputs $F_k(\omega) = f_k \mu(\omega)$

$$T_{ij}(\omega) = \frac{X_i(\omega)}{X_j(\omega)} = \frac{\sum_{k=1}^{r} H_{ik}(\omega) f_k \mu(\omega)}{\sum_{k=1}^{r} H_{jk}(\omega) f_k \mu(\omega)} = \frac{\sum_{k=1}^{r} H_{ik}(\omega) f_k}{\sum_{k=1}^{r} H_{jk}(\omega) f_k} \tag{8.3}$$

In practice, a purely deterministic nature of $T(\omega)$ hardly occurs due to noise and spectral leakage. Thus, transmissibilities will be calculated using H_1 estimator of Eq.8.4, as suggested by Leclere et. al[78]. In that way, the PSDs can be obtained by Welch's method and lead into smoother data.

$$H_1(\omega) = \frac{S_{ij}(\omega)}{S_{jj}(\omega)} \tag{8.4}$$

Due to the fact that the transmissibilities are ratios of FRF elements, by looking in the description of H (see Eq.6.6) one may realize that the poles of the FRF are wiped out. Therefore, the poles of T_{ij} for a single input (see Eq.8.2) are the zeros of H_{jk}, which leads to the conclusion that, when visualizing the transmissibility functions, the peaks of do not correspond at all to any resonance of the system. This for many years made the application of transmissibility measurements in system identification questionable.

However, one of the greatest properties of T_{ij} is that close to resonance it becomes constant and totally independent of the external loading (spectra $\mu_k(\omega)$, location k and magnitude f_k). This property applies regardless of whether the input spectrum has been simplified from T_{ij}, or not[73].

$$\lim_{\omega \to \omega_n} T_{ij}(\omega) = \frac{\varphi_{in}}{\varphi_{jn}} \tag{8.5}$$

Eq.8.5 shows that T_{ij} tends to a ratio between the elements φ_{in} and φ_{jn} of the mode shape φ_n of mode n. This property of the scalar transmissibility function triggered the development of TOMA. The fundamental idea is that by using two sets of response spectra, which correspond to different loading conditions, the transmissibilities of both the cases will have the same value close to the natural frequencies of the system. In other words, by considering two loading cases K and L, the following equation holds.

$$\lim_{\omega \to \omega_n} \Delta T_{ij}^{K-L}(\omega) = \lim_{\omega \to \omega_n} T_{ij}^{K}(\omega) - \lim_{\omega \to \omega_n} T_{ij}^{L}(\omega) = \frac{\varphi_{in}}{\varphi_{jn}} - \frac{\varphi_{in}}{\varphi_{jn}} = 0 \tag{8.6}$$

This means that the function $\Delta T_{ij}^{K-L} \in \mathbb{C}$ becomes zero at the natural frequencies of the system and non-zero at the rest frequency range. Then, by definition, the zeros of ΔT_{ij}^{K-L} will be the poles of $\Delta^{-1} T_{ij}^{KL} = 1/\Delta T_{ij}^{K-L}$ and for this specific problem will include the poles of the system. In that way, the identification is possible once the poles of the so-called base function $\Delta^{-1} T_{ij}^{KL}$ are calculated. By considering all the outputs and a reference response spectra j, the following $\Delta^{-1} T^{KL}$ matrix can be formed.

$$\boldsymbol{\Delta}^{-1}\mathbf{T}^{KL} = \begin{bmatrix} \Delta^{-1} T_{1j}^{KL} \\ \vdots \\ \Delta^{-1} T_{(m-1)j}^{KL} \end{bmatrix} \tag{8.7}$$

This matrix $\mathbf{\Delta}^{-1}\mathbf{T}^{KL} \in \mathbb{C}^{(m-1)x1}$ is structured by arraying all the combinations of outputs without considering the case where $i = j$.

In Chapter 7, LSCF was introduced as a technique able to derive mathematical models which will represent the elements of the output auto/cross PSD matrix. As described in that chapter, each element of this matrix can be modelled as a rational fraction of two polynomials. In addition, all the elements of the PSD matrix will have the same polynomial expression.

This curve-fitting technique will also be used here in order to derive an expression of the denominator of $\mathbf{\Delta}^{-1}\mathbf{T}^{KL}$, the roots of which coincide with the poles of the FRF. The main advantage here is that $\mathbf{\Delta}^{-1}\mathbf{T}^{KL}$ is deterministic and independent of the input spectra. Eq.8.8 shows how matrix $\mathbf{\Delta}^{-1}\mathbf{T}^{KL}$ is represented using the common-denominator description with nominator polynomial N. The reason why this curve-fitting technique is used is to obtain an expression of the polynomial $d(\omega)$.

$$\mathbf{\Delta}^{-1}\mathbf{T}^{KL}(\omega) = \frac{\begin{bmatrix} N_{1j}(\omega) \\ \vdots \\ N_{(m-1)j}(\omega) \end{bmatrix}}{d(\omega)} = \frac{\mathbf{N}(\omega)}{d(\omega)} \tag{8.8}$$

In practice, any frequency-domain estimator can lend itself for the determination of the common-denominator model of Eq.8.8.

Once the roots of the denominator d are calculated, then natural frequencies and the related damping ratio of each mode can be obtained. This identification can be executed in an iterative way for increasing polynomial order in order to generate a stabilization diagram.

In this stabilization diagram one may notice that apart from the resonance frequencies, there are more non-structural modes. These are mathematical modes and can be attributed to the fact that the transmissibilities may cross each-other at frequencies between two natural frequencies. In other words, the poles of the FRF are a subset of the total number of the roots of the common-denominator d. This fact is a minor problem, as one may differentiate between structural modes and mathematical modes by looking into the PSDs of the response. Several approaches have been proposed to remove these mathematical modes by using responses of a third set of loading[32][73]. The idea is that these non-structural modes correspond to a given combination of two loading sets. Hence, a different set of loading will reveal the structural modes. However, using three sets of different loading conditions is not so practical, as the loading in most cases does not change significantly.

Finally, a good estimate of the mode shape can be determined directly from the transmissibilities by taking the frequency line of each natural frequency as described by the limit of Eq.8.5. The whole mode shape can be calculated by using all the $m-1$ transmissibilities. The last m^{th} location can be set to 1. Scaling the mode shape is a decision of the user. A more extensive study about determining the mode shape using TOMA can be found in[74].

8.2. NUMERICAL RESULTS

The approach of TOMA described before will be used in the present section to identify the modal properties of a system loaded by non-white noise input processes. The main shortcoming of this technique is that two sets of responses, which correspond to different loading conditions, need to be used instead of one. This is easier when testing experimentally a system, but in real OWT structures the loading is more-or-less applied at the rotor. In Section 8.2.1 the algorithm will be used on responses derived from the OWT model in Matlab and then in Section 8.2.2, it will be applied on responses derived from the model in FAST.

8.2.1. SIMULATED RESPONSES USING MATLAB MODEL

TOMA for white noise and harmonic input

All the four methods described in the past chapters were based upon the white noise input assumption. In this case two different sets of input will be considered, with non-white noise spectra. In the first simulation, the system is loaded by a concentrated load applied at 53.8m hight with amplified spectral energy between 45rad/s and 55rad/s. The second simulation is similar to the first, but the loaded node is located at 86.08m, while the amplified region extends between 25rad/s and 35rad/s. Figure 8.1 shows the location of the loads together with the related responses.

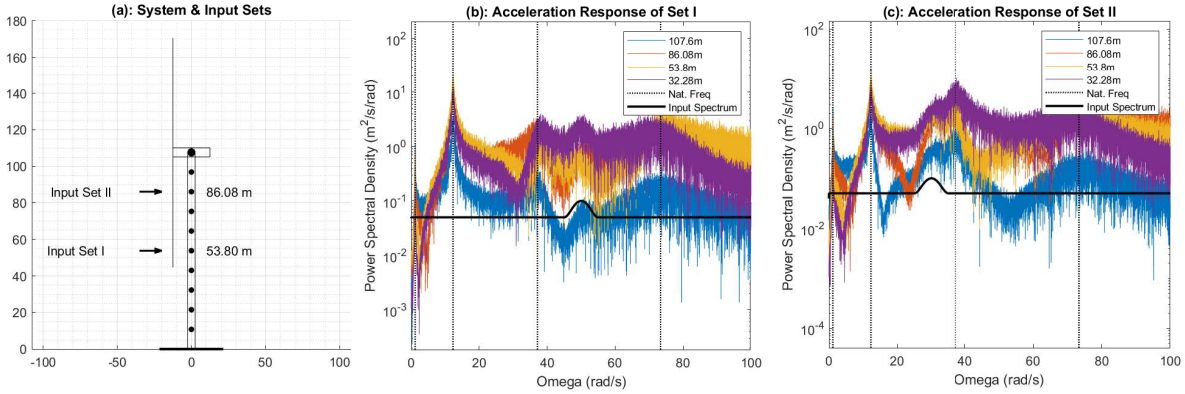

Figure 8.1: Additional simulated cases for the demonstration of TOMA on the OWT model in Matlab

The identification procedure using TOMA is based on the transmissibilities and not directly on the data. Therefore, using these two sets of data, the transmissibilities and the base function ΔT_{ij}^{K-L} can be calculated. In practice, H_1 estimator is used for the calculation of T_{ij}^{K} instead of Eq.8.1. This will deal with the presence of noise and spectral leakage, so that the transmissibilities have a deterministic nature. For the calculation of T_{ij}^{K}, the response signal at sensor of Node 8 (86.08m) is used as a reference signal j. As it can be shown, the transmissibilities for different sets of inputs cross each other at resonance. Apart from that case, several crossings can be also observed between natural frequencies.

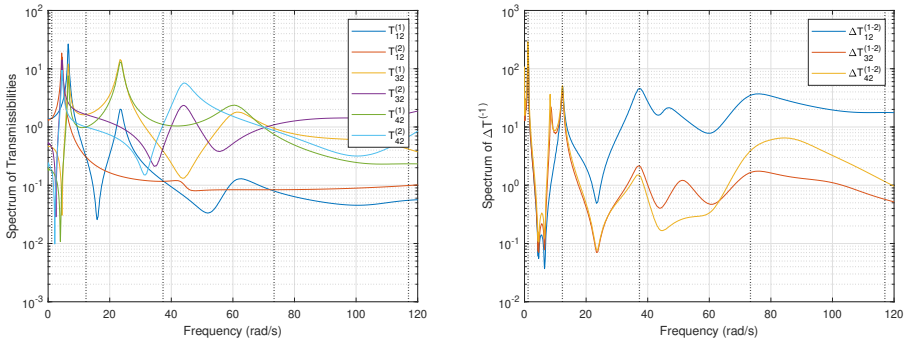

(a) Transmissibility functions T_{ij}^{K}

(b) Base functions ΔT_{ij}^{K-L}

Figure 8.3 shows the stabilization diagram of the identification using LSCF estimator on ΔT_{ij}^{K-L} base functions. As it can be shown, four modes where identified. Moreover, due to the additional crossings of the transmissibilities between the natural frequencies, several non-structural modes have been also identified. These modes can be neglected by looking at the response spectra.

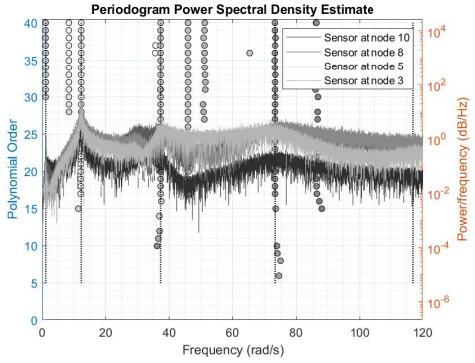

Figure 8.3: Stabilization diagram – TOMA for random, non-white noise excitations

Mode	Exact		TOMA	
	ω_d (rad/s)	ζ (%)	ω_d (rad/s)	ζ (%)
1	1.155	4.00	1.159	3.27
2	12.303	2.00	12.304	2.00
3	37.305	5.09	37.305	5.09
4	73.332	9.83	73.296	9.98

Table 8.1: Identified and exact modal properties - TOMA for OWT in Matlab

One may observe that no mode has been identified between the range of 25rad/s and 35rad/s. The two modes identified at frequencies 45.9rad/s and 51.14rad/s are not due to the input, but due to the additional crossings of the transmissibilities. In case where the location of the load changes (excite different node), these non-structural modes will shift. On the other hand, in case where both the nodes were loaded by the same input, (*e.g.* amplified between 25 and 35rad/s), then the identification would be absolutely the same.

8.2.2. SIMULATED RESPONSES USING MODEL IN FAST

In this Section, TOMA will be used to obtain the modal properties of the OWT model in FAST. The simulated cases that are presented in Table 2.2 correspond to different operating conditions and, thus, TOMA will be performed on different couples of these cases. At first, the time-series corrupted by adding measurement noise of SNR equal to 50. Then, LSCF is applied on the base function $\Delta^{-1}T_{ij}^{KL}$, instead of the PSDs and the procedure is as described in Section 7.2.

Case FC1–FC4

Using TOMA algorithm for the case of an operating OWT is itself a great challenge, since it is almost impossible to obtain in practice responses that correspond to such different inputs as explained in the previous section. More in detail, the system is mainly loaded at the top of the tower and not in between. Therefore, the location of the tower does not change almost at all. Figure 8.4 shows an example of the transmissibilities using load set FC1(1) and FC4(2).

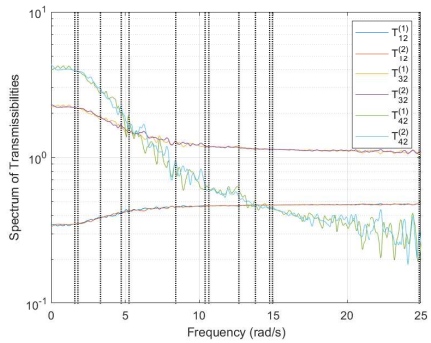

Figure 8.4: Transmissibilities from FC1 and FC4

It is clear that the transmissibilities almost match to each other. Therefore, the identification is not possible using these loading sets. Instead, an alternative option is to use the parked loading case of FC5 as one base set. Then the second set will be one of the four operational cases. However, this algorithm leads into one single identification of the modal properties, and as discussed in Section 3.3.1, the OWT itself will probably have different properties under different operational and parked conditions, leading to errors in the identification.

Case FC1–FC5

The transmissibilities of FC1 and FC5 were different to each other, probably due to the fact that the OWT in case where it is parked is also highly loaded due to the drag forces applied along the tower. Therefore, these two cases correspond to spatially different loading conditions, and applying TOMA was possible.

In the first couple of loading sets FC1 and FC5, three modes have been identified as shown in Table 8.2. As it can be shown, the identification needed lower polynomial order thanks to the deterministic nature of the transmissibilities. Additionally, another observation is that no structural mode was identified between the two tower modes apart from a mode close to B2–F2. TOMA will identify a mode only in case where the ratios of the modal shapes between the locations of the sensors are the same in both the loading sets (see Eq.8.5). However, due to the high difference between the modal properties of the OWT examined in operating and parked conditions, most of the blade modes were not identified. Therefore, in this application the presence of most of the blade modes together with the external loading were removed.

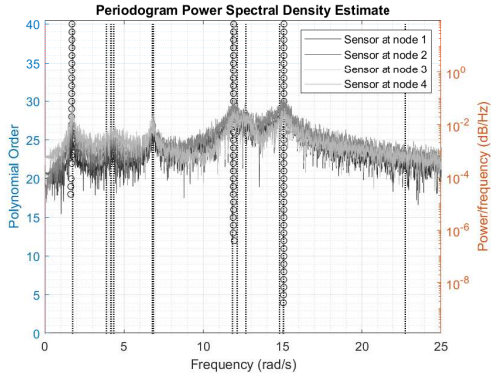

Figure 8.5: TOMA - Stabilization diagram for FC1-FC5

Mode	Exact (8.5rpm)/ Exact (0rpm)		TOMA (FC1-FC5)	
	ω_d (rad/s)	ζ (%)	ω_d (rad/s)	ζ (%)
T-FA1	1.780/ 1.760	6.15/ 0.28	1.735	3.82
B2-F2	11.260/ 11.836	10.80/ 1.88	11.854	3.03
T-FA2	15.040/ 15.055	2.85/ 2.40	15.089	1.01

Table 8.2: TOMA - Identified modal properties for FC1 & FC5

Case FC2–FC5

As already described before, the modes of the blades are largely affected by the fact that the properties of the system change under different loading conditions. Table 8.3 shows that a mode was identified between the two tower modes. This mode was attributed to the blade mode B2–F2, but for this specific couple of measurement sets, it is unclear whether this mode can be related to the blade mode. Still, it is close to the blade mode of FC5, but it deviates slightly from the blade mode of FC2.

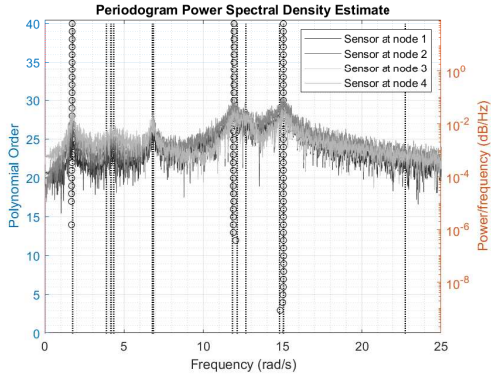

Figure 8.6: TOMA - Stabilization diagram for FC2-FC5

Mode	Exact (10.5rpm)/ Exact (0rpm)		TOMA (FC2-FC5)	
	ω_d (rad/s)	ζ (%)	ω_d (rad/s)	ζ (%)
T-FA1	1.785/ 1.760	7.30/ 0.28	1.754	2.85
B2-F2	11.105/ 11.836	13.60/ 1.88	11.936	3.71
T-FA2	15.015/ 15.055	3.45/ 2.40	15.038	1.52

Table 8.3: TOMA - Identified modal properties for FC2 & FC5

Case FC3–FC5

When FC3 is used together with FC5 in TOMA, the identified modes do not change much. However, the blade mode B2–F2 seems to start deviate more and more from the exact values from FC3. Keep in mind that the tower damping is also not close to the exact values from FAST. The damping ratio of T–FA1 seems to be in between the damping obtained from FAST via linearization, while in T–FA2 it is lower than both the analytically determined damping ratios.

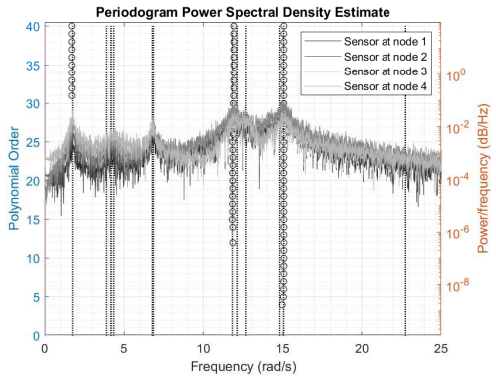

Figure 8.7: TOMA - Stabilization diagram for FC3-FC5

Mode	Exact (11.5rpm)/ Exact (0rpm)		TOMA (FC3-FC5)	
	ω_d (rad/s)	ζ (%)	ω_d (rad/s)	ζ (%)
T-FA1	1.790/ 1.760	7.75/ 0.28	1.705	3.32
B2-F2	11.030/ 11.836	14.70/ 1.88	11.950	2.97
T-FA2	14.995/ 15.055	3.75/ 2.40	15.069	1.43

Table 8.4: TOMA - Identified modal properties for FC3 & FC5

Case FC4–FC5

The last examined sets of measurement data correspond to the parked FC5 and the operating FC4 loading cases. As it can be shown, the identified natural frequency of the blade mode B2–F2 has almost 10% difference with the related exact values of FC4. Hence, this mode might also be a so-called mathematical mode due to additional crossings of the transmissibility functions.

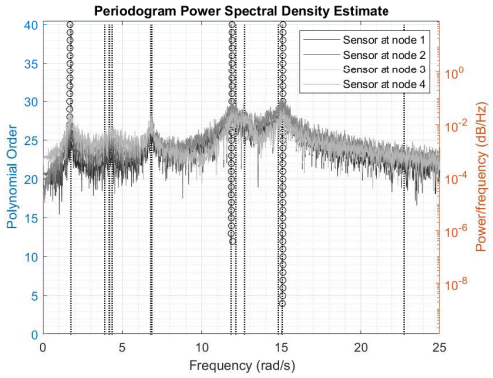

Figure 8.8: TOMA - Stabilization diagram for FC4-FC5

Mode	Exact (12.1rpm) / Exact (0rpm)		TOMA (FC4-FC5)	
	ω_d (rad/s)	ζ (%)	ω_d (rad/s)	ζ (%)
T-FA1	1.805/ 1.760	10.20/ 0.28	1.738	3.39
B2-F2	10.652/ 11.836	22.01/ 1.88	11.961	2.64
T-FA2	14.758/ 15.055	4.34/ 2.40	15.115	1.16

Table 8.5: TOMA - Identified modal properties for FC4 & FC5

8.3. CONCLUSIONS

TOMA was initially applied on the OWT model in Matlab using two newly simulated sets of responses. Each set corresponds to non-white noise concentrated forces at two different nodes. The identification using TOMA resulted in four identified modes, while many of the previously mentioned algorithms were able to identify up to three. This could be due to the fact that the loading is located at nodes closer to the middle of the tower, which leads in higher excitation of the fourth mode.

In the application of the algorithm on FAST, it can be concluded that TOMA resulted in similar modal properties in all the four couples of loading cases. This is reasonable, since all the operating load cases FC1, FC2, FC3 and FC4 have almost the same location of input. In other words, they consider more-or-less that the tower is loaded on top, which results in a later stage in similar transmissibility functions. Therefore, in case where only operating conditions were available, and the spatial distribution of the applied forces is not much different between the two sets of data, TOMA would be very sensitive and probably lead to serious troubles in obtaining the modes of the tower.

Another conclusion is that the identification was not affected by the nP loading of the first loading set FC1, FC2, FC3 and FC4. In parallel, the presence of almost all the blade modes has also been removed. Thanks to that, the transmissibility functions had an almost deterministic nature and, thus, compared to LSCF, TOMA was able to lead into very stable modes already at very lower polynomial orders.

On the contrary to the removal of the blade modes, a mode that could resemble blade mode B2–F2 of FC5 was stably identified in all the cases that were examined. Also, TOMA method was able to identify the modal properties of the tower. However, keep in mind that the identified parameters (*e.g.* damping ratio) are values in between the modal properties of the two examined sets of responses. Finally, by looking in the identification using the set FC4 & FC5, it seems that mode B2–F2 deviates from the related exact value of FC4, which leaves open the possibility of having an non-structural mode that accidentally coincides the blade mode of FC5. This might be attributed to the additional crossings of the transmissibility functions between two modes.

9

SENSORS AND MONITORING FOR OPTIMAL SYSTEM IDENTIFICATION

An offshore wind turbine includes most of the times a specific number of sensors that aims at deriving time-series of several outputs. In the present chapter, at first the number of the sensors will be investigated using the fourth operational case FC4 of the OWT model in FAST. The target is to check whether the results from an OMA algorithm improve by increasing, or worsen by decreasing the number of sensors. In addition, the option of including accelerations data at the tip of a blade will be discussed. The second topic that will be briefly investigated is the case were different types of measurement are confused in the same OMA technique. For the present study, ERA has been selected to be used, thanks to its better and clearer understanding.

9.1. NUMBER AND LOCATION OF SENSORS

Number of sensors along the tower

Given that the data used in the algorithm are selected by the user, it is possible to add and include in the OMA method more sensors placed along the tower. FAST v7.02 gives the possibility of using up to nine accelerometers. These sensors have been placed per 10.325m along the full length of the tower. Then, eight different configurations will be considered when applying ERA/NExT, as displayed in Figure 9.1. At first, all the nine sensors will be used. Then the bottom two will be removed. In each of the last three configurations, one sensor will be removed, until only one sensor is left at the top of the tower. It needs to be mentioned that the fifth configuration includes the same sensors as in FC4.

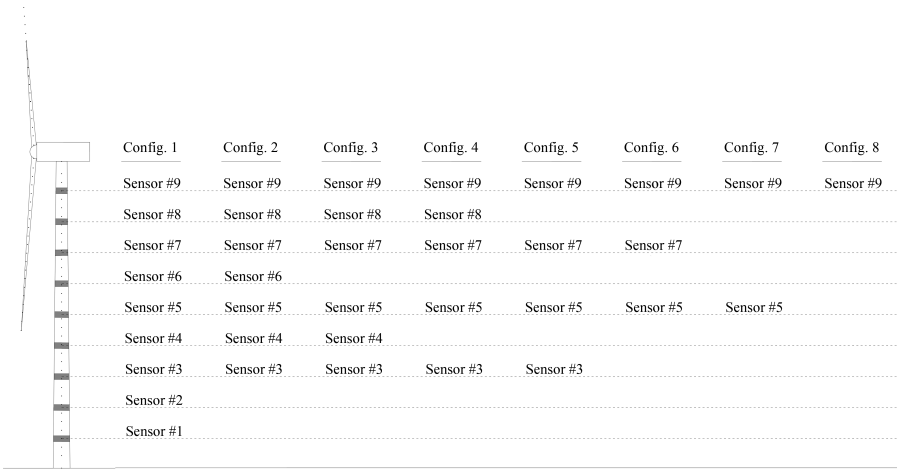

Figure 9.1: Configurations of accelerometers along the tower of OWT model in FAST

For the purpose of this study, ERA/NExT was applied on the data, without considering measurement noise, so that any randomness is removed. Also, the results correspond to system order equal to 80. At first, by looking into Table 9.1 one may notice that the differences between configuration 1 and 2 are minor. Therefore, it was found out that the sensors located at the bottom did not affect the identification. Then, by removing sensors from higher locations, the identified modal properties were slightly affected. The largest difference was observed when Sensor #6 was removed. Still, the differences in the last three configurations are relatively small, and there is no clear tendency towards higher accuracy of the identification. However, when only two sensors are left, as in the last two configurations, one may observe that all the natural frequencies and the related damping ratios have been affected.

Natural Frequencies (rad/s)										
Mode	**Exact**		**Conf. 1**	**Conf. 2**	**Conf. 3**	**Conf. 4**	**Conf. 5**	**Conf. 6**	**Conf. 7**	**Conf. 8**
T-FA1	1.805		1.857	1.856	1.839	1.839	1.842	1.843	1.859	1.863
B2-E1	8.416		8.132	8.132	8.128	8.127	8.125	8.122	8.131	-
B3-F2	13.798		13.703	13.694	13.562	13.589	13.608	13.627	13.894	13.165
T-FA2	14.758		15.122	15.119	15.026	15.040	15.062	15.062	15.134	15.232
Damping Ratio (%)										
Mode	**Exact**		**Conf. 1**	**Conf. 2**	**Conf. 3**	**Conf. 4**	**Conf. 5**	**Conf. 6**	**Conf. 7**	**Conf. 8**
T-FA1	10.20		11.34	11.31	10.90	11.11	11.22	11.39	11.65	10.31
B2-E1	0.90		0.93	0.94	1.05	1.06	1.07	1.09	1.13	-
B3-F2	15.36		5.19	5.20	5.04	4.91	5.00	4.86	4.51	6.99
T-FA2	4.34		1.93	1.97	2.32	2.29	2.26	2.21	1.06	1.74

Table 9.1: Identified and exact modal properties - ERA for FC4 and multiple sensor configurations

The initial target was to obtain more modes by increasing the number of sensors, but as it can be concluded, four accelerometers (or even three) were enough to monitor the tower and capture four modes with an accuracy close to more "dense" setups. In general, the main idea when locating a sensor is highly connected to observability. More in details, when a sensor is located at a node of a sensor, it is impossible to be able measure this mode. In other words, it is preferred to place a sensor at the antinodes of the mode shape, and not at the nodes. This is actually the main reason why removing Sensor #1 and #2 did not affect the identification. Both these sensors are located close to the support, which is a node for all the tower modes. It needs to be mentioned that using more sensors would also lead in more detailed identified mode shapes.

Monitoring blades

In this paragraph, another setup will be discussed. In the benchmark study that was presented in the previous chapters, the measurement data were obtained only from several locations along the tower. This, in combination to the fact that the algorithms were not able to capture the large values of damping related to aerodynamics, could make the option of adding accelerometers on one or more blades very attractive. Therefore, the 5^{th} configuration of sensors shown in Figure 9.1 (FC4) will be examined in case where one blade is also monitored. The additional time-series derived from FAST correspond to the absolute accelerations of the blade tip. Only one blade was included in the monitored parts of the OWT, since the behaviour of the rest two blades was almost the same.

As it can be shown in Figure 9.2, the blade tip (Sensor #10) has much larger accelerations than the sensors along the tower. That is reasonable, since that element is much more flexible than the tower, and also connected to the top of the tower. In addition, one may observe that the blade is excited at nP, where $n = 1, 2, \ldots$, etc. Due to that fact, the presence of the harmonics is more intense at lower frequencies and affect the first tower mode. Apart from that, one can figure out that the modal content of the blade accelerations is not consistent to the modal content of the accelerations along the tower and, therefore, no structural mode was able to be identified.

The difference of the modal content of the blade tip and the tower needs to be investigated further. It is expected that the modal content of the acceleration at the top of the tower should also be present at the acceleration of the blade, since these two elements are connected to each other. However, this is not the case. In order to see the deviation of the spectral content along a tower, Figure 9.4 can be used to display the acceleration spectra at three locations along the blade. The first is at the middle of the blade and the other two close to the root and at the tip. One may observe that indeed the acceleration close to the root has peaks at the modes of the tower and also at several blade modes. However, the tip acceleration is dominated by nP

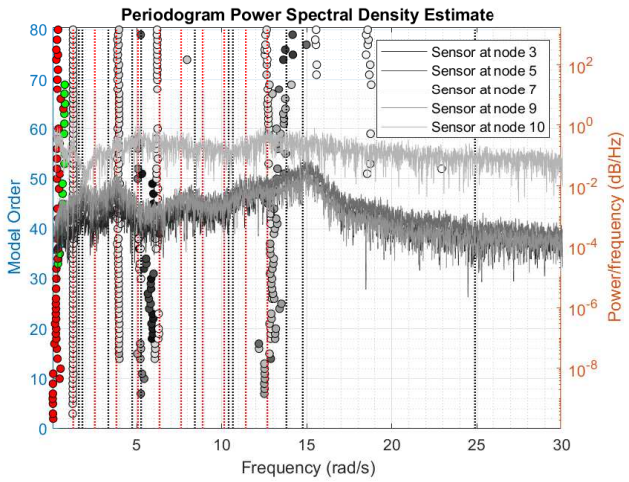

Figure 9.2: Stabilization diagram of sensor configuration #5, considering an accelerometer at blade tip

($n = 1, 2, \ldots$, etc), and at higher frequencies it shows two peaks that are broader than closer to the root. These figures include also the tower (thick solid lines) and blade modes (dashed,dotted and dash-dot lines) and the nP frequencies (red solid lines).

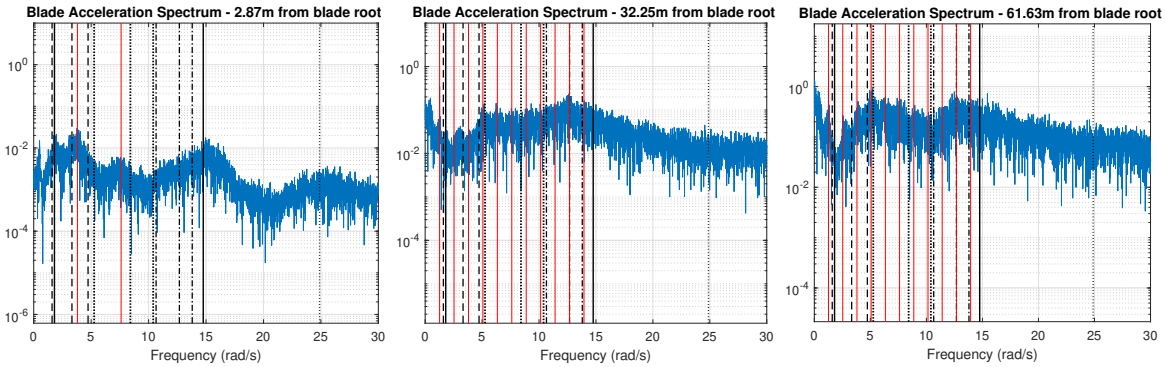

Figure 9.3: Acceleration spectra along the blade

Despite the fact that in the present study the confusion of blade and tower responses was not able to obtain any tower or blade mode, monitoring also all the blades could potentially improve the results of the identification procedure and provide with valuable information. Hence, it is important to investigate several options of sensor positioning in order to improve the identification. Keep in mind that the tower modes are coupled to collective and asymmetric blade modes that are probably not the same to the modes of a single blade. In parallel, the blades are connected to the tower, which means that the absolute acceleration of the whole blade would probably be coupled to the tower top acceleration. Looking more into the responses of a singe blade and combining it with the responses of the tower would probably help in applying OMA techniques on data from different elements of the structure.

9.2. TYPE OF SENSORS

An OWT includes most of the times several types of sensors at multiple locations. Accelerometers, inclinometers and strain sensors are some possible options of gauges that can be used to monitor main parts of wind turbines (*e.g.* tower, blades, etc). The algorithms that were used in this thesis were applied explicitly on acceleration data. However, most of the algorithms do not specify the type of the measurements. In this section, different types of sensors placed along the tower will be used to combined acceleration and strain time-series in the same identification. The OWT model in Matlab that was described in Section 3.2 is able to simulate strain, displacement, velocity and acceleration responses along the tower of the structure. Unfortunately,

this option is not possible for the model in FAST, since version v7.02 generates only accelerations.

The three different setups will be used. The first one includes explicitly strain sensors, the second only accelerometers and the last one a combination of strain and acceleration gauges. The plan is to apply ERA on the two sets of data that correspond to the same type of gauges and then see the influence in case where two types are combined.

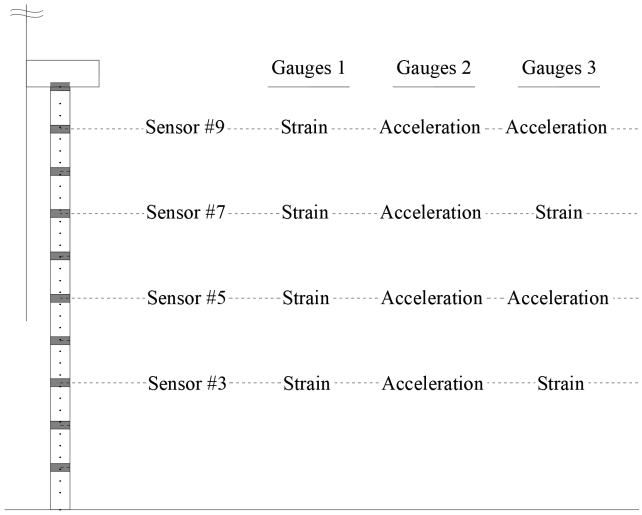

Figure 9.4: Configurations and types of gauges along the tower of OWT model in Matlab

One may notice that when using only strains ERA was able to obtain less modes, and particularly it derived modes with lower natural frequencies. This is possibly related to the fact that the accelerations in frequency domain are a function of the displacement spectra multiplied by ω^2, while the strains in terms of harmonic content are more or less related to the displacements. In that way, in a strain response spectrum higher frequencies are related to smaller values with respect to an acceleration response spectrum. The combination of both strains and accelerations leaded into slightly better results for the first mode compared to the case where only accelerations were used. In addition the case of Gauges 3 was able to obtain the third mode. The performance of ERA was in general quite better when using only accelerations. However, it seems that adding strains did not make the identification worse.

Mode	**Exact**		**Gauges 1**		**Gauges 2**		**Gauges 3**	
	ω_d (rad/s)	ζ (%)	ω_d (rad/s)	ζ (%)	ω_d (rad/s)	ζ (%)	ω_d (rad/s)	ζ (%)
1	1.155	4.00	1.155	3.23	1.149	3.17	1.151	3.69
2	12.303	2.00	12.321	1.72	12.307	1.98	12.316	1.75
3	37.305	5.09	-	-	37.296	4.76	36.931	4.05

Table 9.2: Identified and exact modal properties - ERA for OWT model in Matlab, white noise loading and different types sensor

It was found out that ERA leaded into reasonable results even when both strains and accelerations where considered. This could be due to the fact that ERA relates the output measurements to the state-space via matrix **C** (see Eq.4.1). Therefore, one may expect that the system matrix **A** is independent of the inputs signals. The same concept also holds for SSI. Finally, FDD and LSCF based the identification on the expression of PSDs. Regardless of the type of the signal used (strains, velocities or accelerations), these functions will still have the same poles. The reason is that in frequency domain, they are connected by multiplying or dividing with ω (or ω^2).

Different units between different signals probably would lead in using time-series with magnitudes orders larger or smaller to each other. For this particular example, strains were 100 times smaller than the accelerations. Scaling the response signals did not lead into any big difference. Since accelerations showed better behaviour in the identification, it would be interesting to look for approaches to obtain acceleration time-series from strain time-series. One approach was proposed by Chan-gi Pak[79] in order to obtain acceleration and velocity responses from measured strains.

The option of using alternative system identification approaches, where also input time-series are available is really promising and attractive. The scope of this thesis is limited to OMA algorithms that consider an unknown and unmeasurable input. However, in ideal conditions, where more parameters could be monitored, it would be very interesting to collect also time-series of input-related parameters.

10

CONCLUSIONS AND RECOMMENDATIONS

*The scope of this thesis presented in the introduction highlighted two main objectives. The first stated that it is important to assess and eliminate the impact of limitations related to loading on the identification and according to the second, the applicability of OMA system identification techniques on measurements of different operational conditions need to be investigated. These would answer the questions of whether existing OMA system identification algorithms are able to be adapted and used on operating OWTs. In parallel, it was suggested to examine several ways to optimize the identification procedure by directly interfering in the code (*e.g. *filtering stabilization diagrams, etc.) or by investigating different sensor locations and also confusing different types of sensors*

10.1. CONCLUSIONS

Robustness against non white noise excitation

Initially, once the algorithm behind each OMA method was developed, the OWT model in Matlab was used for validation. In that way, the strategy behind each algorithm was presented, and the behaviour of each algorithm in the identification of this simple LTI model was explained. The robustness against closely spaced harmonics was also investigated for each algorithms, apart from TOMA. It was found out that the algorithms that were affected the most are SSI-b and SSI-Ov. On the other hand, TOMA was able to identify the modal properties even for loading that includes coloured noise, without leading into fake modes at these frequencies.

Suggested optimizations for the identification procedure

While presenting the algorithms, several techniques were described to derive clear stabilization diagrams. In SSI, it was found out that the non-structural modes were highly affected by the randomness of the measurement noise that was added on the data. Therefore, these modes can be removed by running the identification twice and comparing the identified modes between the two diagrams.

Also, in FDD, a pseudo-stabilization diagram was used, which could reveal the unstable modes. In case where a selected peak was corrupted by neighbouring harmonics, then the length of the free decay that was used for the identification affected the identified modes. Each iteration corresponds to a different manually selected range of the free decay.

Finally, in LSCF and TOMA, the modelled curves could be fitted over a smaller frequency range, particularly when the sampling frequency is larger than the region where the modal content is concentrated. Then by truncating different parts of the PSD, a big part of the spurious non-structural modes will shift. This can be used to remove several unstable modes that are not related to modes.

Conclusions of the Benchmark study

Based on the results of the algorithms that were examined in the benchmark study, a summary of their performance against the assessment criteria is presented in Table 10.1.

Technique	Number of modes	Stability of modes	Deviation from exact values
ERA	++++	+++	+++
SSI	++	++++	++++
FDD	++	++	+++
LSCF	++++	+++	+++
TOMA	++	++++	+

Table 10.1: Performance of OMA techniques per assessment criteria

At first, regarding the application of ERA/NExT on data from FAST, this technique resulted in a large number of identified modes with respect to the other algorithms. However, by looking into the stabilization diagrams that corresponded to an operating turbine, the blade modes were quite unstable. Additionally, when ERA/NExT was applied on data from a parked turbine, it resulted explicitly in stable modes. Therefore, the unstable blade modes of the rest cases can be directly linked to the rotation of the rotor. This observation has two possible explanations, since the modes could be either affected by the harmonic excitation or by the fact that they change with the time-varying rotational speed.

Regarding SSI, it was found out that this algorithm obtained more stable modes, but was able to identify less modes than ERA/NExT. A possible reason could be the fact that the projection matrix $\mathbf{O}_i$ is derived from a multiplication of Hankel matrices that include shifted data. This results in some kind of covariance matrix, which has removed the influence of the stochastic white noise input. A similar idea was presented in Section 4.2, when the theory behind NExT was explained. However, the difference is that in ERA/NExT, only the first part of the correlation function is considered for the identification (almost 5%), while in SSI the whole time-series will be used. Therefore, several transient parts related to the input, or/and the time-invariant behaviour of the system might result in a less impulse-like signal and affect the identification of stable modes. This could be the reason why SSI was largely affected by the violation of the OMA assumptions. Finally, all the SSI algorithms run twice for each identification, to filter out the unstable modes. In that step, the first fore-aft tower bending mode was also removed due to unstable damping.

FDD was able to derive both the tower bending modes, even though the first tower bending mode was affected by the presence of 3P. Regarding the blade modes, FDD resulted in a very small number of stable blade modes. The main reason is that the influence of nP harmonics was dominant between the tower modes, and no clear peaks could be obtained. Moreover, most of the 2$^{\text{nd}}$ flapwise bending modes were dominated by the presence of the second tower mode.

Apart from ERA/NExT, LSCF was also able to lead into dense stabilization diagrams. In all the examined cases the algorithm identified both the tower modes and a big number of blade modes. In general, LSCF resulted also in a big number of non-structural modes, and this would probably lead into problems when selecting the structural modes. In some cases, the identified damping was found to be extremely low (<1%). This can be explained by the low frequency resolution together with the presence of noise. In other words, this happens because LSCF fits initially a single peak at a mode and this corresponds to almost zero damping. In such a case, a larger order could be used to obtain a modal damping, but it would probably be very sensitive.

Finally, TOMA was able to identify both the tower modes. In parallel, it also resulted into a third mode that could resemble blade mode B2-F2 of FC5 for all the cases that were examined. However, in TOMA the identified parameters (*e.g.* damping ratio) are values in between the modal properties of the two examined sets of responses. It needs to be mentioned that by looking in the identification using the set FC4 & FC5, it seems that mode B2-F2 deviates from the related exact value of FC4, which leaves open the possibility of having an non-structural mode that accidentally coincides the blade mode of FC5. Compared to LSCF, the almost deterministic nature of TOMA leaded in very stable modes already at much lower polynomial orders.

Conclusions on identified damping ratio of flapwise blade bending modes

The main attention was attracted by the inability of the algorithm to capture the extremely high ($\gg$10%) damping ratios of the flapwise blade bending modes. In general the damping estimation was better for the edgewise modes which is limited at values lower than 10%. Apart from TOMA, which resulted mainly in tower modes, the flapwise blade modes identified by the rest algorithms showed in several cases increased damping ratios, larger than the edgewise modes. However, as mentioned before, large damping ratios were underestimated. One possible reason is the fact that in many cases the flapwise modes were close to nP excitation. In

parallel, such large damping ratios would have in time-domain very short free decay responses, and in frequency domain very a broad and short peak response spectrum. In that way, the neighbouring nP excitation could confuse the algorithms and underestimate the actual damping ratios.

The influence of the loading for different operational cases

Compared to parked conditions, it is clear that the identified modal parameters that correspond to operating conditions are much more unstable and difficult to obtain. At first, **ERA/NExT**, SSI, FDD and LSCF identified most of the nP components of the wind loading. As the wind speed increases, SSI was more-and-more affected by the external loading. The same happened to ERA/NExT and LSCF. The main reason is that the influence of the nP becomes more severe in two ways. At first the excitation is amplified, but also by increasing the rotational speeds, the range over which the excitation is dominant becomes broader. In that way, in FC4, the second tower mode and the 9P loading were almost coincident, while in FC1 the second tower mode was between 12P and 15P that were attenuated.

Another conclusion is that by using TOMA, the identification of the tower modes was not affected by the nP loading of the first loading set FC1,FC2,FC3 or FC4. In parallel, the presence of almost all the blade modes has also been removed.

Regarding the wave loading, both the models showed a very stiff behaviour with respect to wave loading. The algorithms were applied on the mode in Matlab under wind, wave and current excitation, but they did not show to be significantly influenced.

The influence of violating the LTI assumption

The violation of the LTI assumption in the model in FAST has a direct influence in the performance of TOMA, where two sets of data that correspond to different conditions need to be used. More in detail, the modal properties of an OWT are highly affected by the loading conditions and therefore, TOMA results in modal properties that are between the modal properties of the two examined sets.

Additionally, as mentioned before, the violation of the LTI assumption would affect the stationarity of the response time-series and could be a reason of obtaining unstable blade modes using ERA/NExT and a small number of blade modes using SSI. Additionally, regarding the frequency-domain techniques, inverting a signal from time-domain into frequency-domain will lead in a loss of the time resolution. Then, this wild affect the shape of spectral peaks and therefore affect damping estimation.

Sensors: Types and Locations

Regarding the number of the accelerometers that were located along the tower, it was found out that by applying ERA/NExT on more than 4 sensors in operational case FC4, the results of the identification did not improve much. Four accelerometers (or even three) were enough to monitor the tower and capture four modes with an accuracy close to more "dense" setups. In order a mode to be observable, the sensor should be away from the nodes of the mode, and the best locations would be close to the antinodes.

Another setup considered also the case where one blade was monitored. It was found out that the tip acceleration is dominated by nP ($n = 1, 2, \ldots$, etc), and the modal content of the blade tip accelerations is not consistent to the modal content of the accelerations along the tower. Due to that fact, no structural mode was able to be identified.

Finally, when both strains and acceleration data were confused in the same identification, the algorithm was able to obtain the modal properties of the examined system using ERA/NExT. However, the identification based explicitly on strain data resulted in less modes than using accelerations. The reason could be that in frequency-domain, accelerations are connected to displacements by multiplying ω^2, while strains are related to the spatial derivative of the displacement. Therefore, using accelerations is more efficient in identifying modes at higher frequencies.

10.2. RECOMMENDATIONS

Guidelines: OMA algorithms that deal with harmonic input

Several approaches can be found in literature that aim at eliminating the influence of the harmonic components in the modal parameter extraction process. P. Mohanty and D.J. Rixen, modified several classic modal

identification methods, in order to obtain the actual structural modes even in cases where harmonics components are close to the natural frequencies of the system[20][21][22][23]. In addition, classical SSI algorithm has also been [24]. However, the present study showed that the harmonic excitation introduced by rotational sampling are not single harmonic components with frequencies nP. Instead rotational sampling will lead into a wider range of amplified excitation around nP frequencies. Therefore, these modified algorithms will not be able to deal with the violation of the white noise input assumption.

Future work: Promising OMA techniques for dealing with non-white noise of operating OWTs

Based on the gained experience, it is clear that all the algorithms have pros and cons. But the most promising approach in removing the influence of the external loading would be transmissibility based techniques. Several existing approaches have been investigated by different researchers, which do not use different sets of loadings in the identification procedure. In that way, the identified modes will correspond to the modal properties of the system, while operating. PSDT and Tv-TOMA are two of such techniques. PSDT has been developed in a different way and leads into non deterministic transmissiblities. Therefore, it wound be suggested to investigate such algorithm, together with a stochastic frequency domain estimator (*e.g.* BTLS or MLE) for the case of operating OWT.

Future work: Loading conditions of data sets in TOMA

In this study, TOMA was performed on two sets of data that corresponded to loading conditions that are essentially different. In particular, one set was referring to operating and one to parked turbine. Investigating data sets that correspond to different couples of loading conditions could make transmissibility-based algorithms perform better and would contribute significantly in determining the modal properties of an operating OWT (*e.g.* wind-wave misalignment, wind misalignment, etc.).

Future work: Wave loading

Wave loading does violate the white noise excitation assumption, but in the models that were used for the present study the influence of wave loading was not significant and did not affect the identification of the OWT system in Matlab. However, the presence of wave loading is significant and due to the fact that it is close to the first tower mode, investigating further their effect on the OMA algorithms would be of great importance.

Future work: Additional sensors on blades

Despite the fact that in the present study the confusion of blade and tower responses directly in ERA/NExT algorithm was not able to obtain any tower or blade mode, monitoring also all the blades could potentially improve the results of the identification procedure and provide with valuable information. Hence, it is important to investigate several options of sensor positioning on the blades in order to improve the identification.

It needs to be mentioned that the tower modes are coupled to collective and asymmetric blade modes that are probably not the same to the modes of a single blade. In parallel, the blades are connected to the tower, which means that the absolute acceleration of the whole blade would probably be coupled to the acceleration at the top of the tower. Looking more into the modal content of a singe blade responses and combining it with the modal content of the tower responses would probably help in applying OMA techniques on data from different elements of the structure.

Future work: Converting output time-series into accelerations

Since accelerations showed better behaviour in the identification, it would be interesting to look for approaches to obtain acceleration time-series from strain time-series. One approach was proposed by Chan-gi Pak[79] in order to obtain acceleration and velocity responses from measured strains.

Future work: System identification considering both input and output time-series

The system identification algorithms that consider both output and input data are sometimes referred in literature as deterministic system identification. The option of using such approaches, where also input time-series are available is really promising and attractive. The scope of this thesis is limited to OMA algorithms that consider an unknown and unmeasurable input. However, in ideal conditions, where more parameters could be monitored, it would be very interesting to collect also time-series of input-related parameters (*e.g.* wind speed, forcing at the RNA base, etc.).

BIBLIOGRAPHY

[1] IRENA(2018), *Offshore innovation widens renewable energy options: Opportunities, challenges and the vital role of international co-operation to spur the global energy transformation, (Brief to G7 policy makers),* in *International Renewable Energy Agency, Abu Dhabi* (2018).

[2] J.-N. Juang and R. S. Pappa, *An eigensystem realization algorithm for modal parameter identification and model reduction,* Journal of guidance, control, and dynamics **8**, 620 (1985).

[3] J.-N. Juang, *Applied system identification* (Prentice Hall, 1994).

[4] I. IBRAHIM and E. Mikulcik, *Shock and Vibration Bulletin 43, 21-37,* A time domain vibration test technique **4** (1973).

[5] D. L. Brown, R. J. Allemang, R. Zimmerman, and M. Mergeay, *Parameter estimation techniques for modal analysis,* SAE transactions , 828 (1979).

[6] G. James, T. G. Carne, J. P. Lauffer, *et al.*, *The natural excitation technique (NExT) for modal parameter extraction from operating structures,* Modal Analysis-the International Journal of Analytical and Experimental Modal Analysis **10**, 260 (1995).

[7] G. James, T. Carne, and P. Veers, *Damping measurements using operational data,* Journal of solar energy engineering **118**, 190 (1996).

[8] P. Van Overschee and B. De Moor, *Subspace identification for linear systems: theory-implementations-applications,* (1996).

[9] P. Van Overschee and B. De Moor, *Subspace algorithms for the stochastic identification problem,* Automatica **29**, 649 (1993).

[10] R. Brincker, L. Zhang, and P. Andersen, *Modal identification of output-only systems using frequency domain decomposition,* Smart materials and structures **10**, 441 (2001).

[11] P. Guillaume, P. Verboven, and S. Vanlanduit, *Frequency-domain maximum likelihood identification of modal parameters with confidence intervals,* in *Proceedings of the international seminar on modal analysis*, Vol. 1 (Katholieke Universiteit Leuven, 1998) pp. 359–366.

[12] P. Guillaume, P. Verboven, S. Vanlanduit, H. Van Der Auweraer, and B. Peeters, *A poly-reference implementation of the least-squares complex frequency-domain estimator,* in *Proceedings of IMAC*, Vol. 21 (A Conference & Exposition on Structural Dynamics, Society for Experimental . . . , 2003) pp. 183–192.

[13] B. Peeters, H. Van der Auweraer, *et al.*, *PolyMAX: a revolution in operational modal analysis,* in *1st International Operational Modal Analysis Conference, Copenhagen, Denmark, Apr* (2005) pp. 26–27.

[14] A. Jhinaoui, L. Mevel, J. Morlier, and W. Zhou, *Generalized subspace identification for rotating systems: application to a wind turbine,* in *Leuven Conference on Noise and Vibration Engineering* (2012).

[15] M. S. Allen, S. Chauhan, and M. H. Hansen, *Advanced operational modal analysis methods for linear time periodic system identification,* in *Civil Engineering Topics, Volume 4* (Springer, 2011) pp. 31–44.

[16] E. N. Chatzi and A. W. Smyth, *Nonlinear system identification: Particle-based methods,* Encyclopedia of Earthquake Engineering , 1 (2014).

[17] F. Naets, J. Croes, and W. Desmet, *An online coupled state/input/parameter estimation approach for structural dynamics,* Computer Methods in Applied Mechanics and Engineering **283**, 1167 (2015).

[18] D. Amsallem and C. Farhat, *An online method for interpolating linear parametric reduced-order models,* SIAM Journal on Scientific Computing **33**, 2169 (2011).

[19] P. E. Wellstead, *Non-parametric methods of system identification,* Automatica **17**, 55 (1981).

[20] P. Mohanty and D. J. Rixen, *Operational modal analysis in the presence of harmonic excitation,* Journal of sound and vibration **270**, 93 (2004).

[21] P. Mohanty and D. J. Rixen, *Modified ERA method for operational modal analysis in the presence of harmonic excitations,* Mechanical Systems and Signal Processing **20**, 114 (2006).

[22] P. Mohanty and D. Rixen, *A modified (ibrahim) time domain algorithm for operational modal analysis including harmonic excitation,* Journal of Sound and Vibration **275**, 375 (2004).

[23] P. Mohanty and D. J. Rixen, *Modified SSTD method to account for harmonic excitations during operational modal analysis,* Mechanism and Machine theory **39**, 1247 (2004).

[24] K. Dai, Y. Wang, Y. Huang, W. Zhu, and Y. Xu, *Development of a modified stochastic subspace identification method for rapid structural assessment of in-service utility-scale wind turbine towers,* Wind Energy **20**, 1687 (2017).

[25] N.-J. Jacobsen, *Separating structural modes and harmonic components in operational modal analysis,* in *Proceedings IMAC XXIV Conference* (2006).

[26] N.-J. Jacobsen, P. Andersen, and R. Brincker, *Using enhanced frequency domain decomposition as a robust technique to harmonic excitation in operational modal analysis,* in *Proceedings of ISMA2006: international conference on noise & vibration engineering* (Belgium Leuven, 2006) pp. 18–20.

[27] N.-J. Jacobsen, P. Andersen, and R. Brincker, *Eliminating the influence of harmonic components in operational modal analysis,* in *Proceedings of The 25th International Modal Analysis Conference (IMAC), Orlando, Florida* (2007).

[28] P. Guillaume, C. Devriendt, and G. De Sitter, *Identification of modal parameters from transmissibility measurements,* in *Proceedings of the 1st international operational modal analysis conference, Copenhagen* (2005) pp. 26–27.

[29] C. Devriendt and P. Guillaume, *The use of transmissibility measurements in output-only modal analysis,* Mechanical Systems and Signal Processing **21**, 2689 (2007).

[30] C. Devriendt, G. De Sitter, S. Vanlanduit, and P. Guillaume, *Operational modal analysis in the presence of harmonic excitations by the use of transmissibility measurements,* Mechanical systems and signal processing **23**, 621 (2009).

[31] C. Devriendt, W. Weijtjens, G. De Sitter, and P. Guillaume, *Combining multiple single-reference transmissibility functions in a unique matrix formulation for operational modal analysis,* Mechanical Systems and Signal Processing **40**, 278 (2013).

[32] C. Devriendt, G. De Sitter, and P. Guillaume, *An operational modal analysis approach based on parametrically identified multivariable transmissibilities,* Mechanical Systems and Signal Processing **24**, 1250 (2010).

[33] W. Weijtjens, G. De Sitter, C. Devriendt, and P. Guillaume, *Operational modal parameter estimation of MIMO systems using transmissibility functions,* Automatica **50**, 559 (2014).

[34] W. Weijtjens, J. Lataire, C. Devriendt, and P. Guillaume, *Dealing with periodical loads and harmonics in operational modal analysis using time-varying transmissibility functions,* Mechanical Systems and Signal Processing **49**, 154 (2014).

[35] W. Weijtjens, J. Lataire, C. Devriendt, and P. Guillaume, *Transmissibility based OMA for time-varying loading conditions,* (2014).

[36] W.-J. Yan and W.-X. Ren, *Operational modal parameter identification from power spectrum density transmissibility,* Computer-Aided Civil and Infrastructure Engineering **27**, 202 (2012).

[37] W.-J. Yan and W.-X. Ren, *An Enhanced Power Spectral Density Transmissibility (EPSDT) approach for operational modal analysis: theoretical and experimental investigation,* Engineering Structures **102**, 108 (2015).

[38] M. H. Hansen, *Aeroelastic instability problems for wind turbines,* Wind Energy: An International Journal for Progress and Applications in Wind Power Conversion Technology **10**, 551 (2007).

[39] M. Arshad and B. C. O'Kelly, *Offshore wind-turbine structures: a review,* Proceedings of the Institution of Civil Engineers-Energy **166**, 139 (2013).

[40] A. Group *et al., Technical application papers No. 13 wind power plants*, Tech. Rep. (Bergamo, Italy, 2011).

[41] F. Petrini, H. Li, and F. Bontempi, *Basis of design and numerical modeling of offshore wind turbines,* Structural engineering & mechanics **36**, 599 (2010).

[42] T. Burton, N. Jenkins, D. Sharpe, and E. Bossanyi, *Wind energy handbook* (John Wiley & Sons, 2011).

[43] E. Kulunk, *Aerodynamics of wind turbines,* in *Fundamental and Advanced Topics in Wind Power* (InTech, 2011).

[44] K. Hasselmann, T. Barnett, E. Bouws, H. Carlson, D. Cartwright, K. Enke, J. Ewing, H. Gienapp, D. Hasselmann, P. Kruseman, *et al., Measurements of wind-wave growth and swell decay during the Joint North Sea Wave Project (JONSWAP),* Ergänzungsheft 8-12 (1973).

[45] W. J. Pierson Jr and L. Moskowitz, *A proposed spectral form for fully developed wind seas based on the similarity theory of SA Kitaigorodskii,* Journal of geophysical research **69**, 5181 (1964).

[46] J. Jonkman, S. Butterfield, W. Musial, and G. Scott, *Definition of a 5-MW reference wind turbine for offshore system development,* National Renewable Energy Laboratory, Golden, CO, Technical Report No. NREL/TP-500-38060 (2009).

[47] J. M. Jonkman and M. Buhl Jr, *FAST user's guide, national renewable energy laboratory,* No. NREL/EL-500-38230, Golden, CO (2005).

[48] J.-N. Juang and R. S. Pappa, *Effects of noise on modal parameters identified by the eigensystem realization algorithm,* Journal of Guidance, Control, and Dynamics **9**, 294 (1986).

[49] W. Yang, H. Li, S.-L. J. Hu, and Y. Teng, *Stochastic modal identification in the presence of harmonic excitations,* .

[50] G. Zhang, B. Tang, and G. Tang, *An improved stochastic subspace identification for operational modal analysis,* Measurement **45**, 1246 (2012).

[51] M. W. Häckell and R. Rolfes, *Monitoring a 5-MW offshore wind energy converter — Condition parameters and triangulation based extraction of modal parameters,* Mechanical Systems and Signal Processing **40**, 322 (2013).

[52] R. Brincker and P. Andersen, *Understanding stochastic subspace identification,* Proceedings of the 24th IMAC, St. Louis **126** (2006).

[53] W. Favoreel, B. De Moor, and P. Van Overschee, *Subspace state space system identification for industrial processes,* Journal of process control **10**, 149 (2000).

[54] X. Dong, J. Lian, M. Yang, and H. Wang, *Operational modal identification of offshore wind turbine structure based on modified stochastic subspace identification method considering harmonic interference,* Journal of Renewable and Sustainable Energy **6**, 033128 (2014).

[55] R. Brincker, L. Zhang, and P. Andersen, *Modal identification from ambient responses using frequency domain decomposition,* in *Proc. Proc. of the 18*'International Modal Analysis Conference (IMAC), San Antonio, Texas* (2000).

[56] R. Brincker, C. Ventura, and P. Andersen, *Damping estimation by frequency domain decomposition,* in *19th International Modal Analysis Conference* (2001) pp. 698–703.

[57] P. Andersen, R. Brincker, M. Goursat, and L. Mevel, *Automated modal parameter estimation for operational modal analysis of large systems,* in *Proceedings of the 2nd international operational modal analysis conference*, Vol. 1 (2007) pp. 299–308.

[58] A. Hasan, M. Danial, Z. Ahmad, M. Salman Leong, and L. Hee, *Enhanced frequency domain decomposition algorithm: a review of a recent development for unbiased damping ratio estimates,* Journal of Vibroengineering **20**, 1919 (2018).

[59] H. Van Der Auweraer, P. Guillaume, P. Verboven, and S. Vanlanduit, *Application of a fast-stabilizing frequency domain parameter estimation method,* Journal of dynamic systems, measurement, and control **123**, 651 (2001).

[60] M. El-Kafafy, P. Guillaume, B. Peeters, F. Marra, and G. Coppotelli, *Advanced frequency-domain modal analysis for dealing with measurement noise and parameter uncertainty,* in *Topics in Modal Analysis I, Volume 5* (Springer, 2012) pp. 179–199.

[61] B. Peeters, H. Van der Auweraer, P. Guillaume, and J. Leuridan, *The PolyMAX frequency-domain method: a new standard for modal parameter estimation?* Shock and Vibration **11**, 395 (2004).

[62] B. Cauberghe, P. Guillaume, P. Verboven, E. Parloo, and S. Vanlanduit, *The secret behind clear stabilization diagrams: the influence of the parameter constraint on the stability of the poles,* in *Proceedings of the 10th SEM international congress & exposition on experimental and applied mechanics* (2004) pp. 7–10.

[63] R. Pintelon, P. Guillaume, Y. Rolain, J. Schoukens, and H. Van Hamme, *Parametric identification of transfer functions in the frequency domain-a survey,* IEEE transactions on automatic control **39**, 2245 (1994).

[64] R. Pintelon, P. Guillaume, G. Vandersteen, and Y. Rolain, *Analyses, development, and applications of TLS algorithms in frequency domain system identification,* SIAM journal on matrix analysis and applications **19**, 983 (1998).

[65] G. Vandersteen, K. Barbé, R. Pintelon, and J. Schoukens, *Bootstrapped total least squares estimator using (circular) overlap for errors-in-variables identification,* IFAC Proceedings Volumes **42**, 1568 (2009).

[66] R. Pintelon and J. Schoukens, *System identification: a frequency domain approach* (John Wiley & Sons, 2012).

[67] P. Welch, *The use of fast fourier transform for the estimation of power spectra: a method based on time averaging over short, modified periodograms,* IEEE Transactions on audio and electroacoustics **15**, 70 (1967).

[68] W. Liu and D. Ewins, *Transmissibility properties of MDoF systems,* in *Proceedings-Spie The International Society For Optical Engineering*, Vol. 2 (SPIE INTERNATIONAL SOCIETY FOR OPTICAL, 1998) pp. 847–854.

[69] P. S. Varoto and K. G. McConnell, *Single point vs. multi point acceleration transmissibility concepts in vibration testing,* in *Society for Experimental Mechanics, Inc, 16 th International Modal Analysis Conference.*, Vol. 1 (1998) pp. 83–90.

[70] A. Ribeiro, J. Silva, and N. Maia, *On the generalisation of the transmissibility concept,* Mechanical Systems and Signal Processing **14**, 29 (2000).

[71] N. M. Maia, J. M. Silva, and A. M. Ribeiro, *The transmissibility concept in multi-degree-of-freedom systems,* Mechanical Systems and Signal Processing **15**, 129 (2001).

[72] M. Fontul, A. Ribeiro, J. Silva, and N. Maia, *Transmissibility matrix in harmonic and random processes,* Shock and Vibration **11**, 563 (2004).

[73] C. Devriendt and P. Guillaume, *Identification of modal parameters from transmissibility measurements,* Journal of Sound and Vibration **314**, 343 (2008).

[74] C. Devriendt, G. Steenackers, G. De Sitter, and P. Guillaume, *From operating deflection shapes towards mode shapes using transmissibility measurements,* Mechanical Systems and Signal Processing **24**, 665 (2010).

[75] G. De Sitter, C. Devriendt, and P. Guillaume, *Transmissibility-based operational modal analysis: Enhanced stabilisation diagrams,* Shock and Vibration **19**, 1085 (2012).

[76] W. Weijtjens, G. de Sitter, C. Devriendt, and P. Guillaume, *Operational modal analysis based on multivariable transmissibility functions: Revisited,* in *Topics in Dynamics of Civil Structures, Volume 4* (Springer, 2013) pp. 317–326.

[77] W. Weijtjens, G. De Sitter, C. Devriendt, and P. Guillaume, *Automated transmissibility based operational modal analysis for continuous monitoring in the presence of harmonics,* in *Proceedings of the 9th International Conference on Structural Dynamics (EURODYN), Porto, Portugal* (2014) pp. 2231–2238.

[78] Q. Leclere, N. Roozen, and C. Sandier, *On the use of the Hs estimator for the experimental assessment of transmissibility matrices,* Mechanical Systems and Signal Processing **43**, 237 (2014).

[79] C.-g. Pak and R. A. Truax, *Acceleration and velocity sensing from measured strain,* in *AIAA Infotech@ Aerospace* (2016) p. 1229.